

---


Electronic Theses and Dissertations, 2004-2019

---

2005

## Transmission Electron Microscopy Studies In Shape Memory Alloys

Madhavi Tiyyagura  
*University of Central Florida*

 Part of the [Materials Science and Engineering Commons](#)  
Find similar works at: <https://stars.library.ucf.edu/etd>  
University of Central Florida Libraries <http://library.ucf.edu>

This Masters Thesis (Open Access) is brought to you for free and open access by STARS. It has been accepted for inclusion in Electronic Theses and Dissertations, 2004-2019 by an authorized administrator of STARS. For more information, please contact [STARS@ucf.edu](mailto:STARS@ucf.edu).

---

### STARS Citation

Tiyyagura, Madhavi, "Transmission Electron Microscopy Studies In Shape Memory Alloys" (2005).  
*Electronic Theses and Dissertations, 2004-2019*. 406.  
<https://stars.library.ucf.edu/etd/406>

TRANSMISSION ELECTRON MICROSCOPY STUDIES IN SHAPE MEMORY ALLOYS

by

MADHAVI TIYYAGURA

B.Tech. Metallurgy, Regional Engineering College, Warangal, 2000

A thesis submitted in partial fulfillment of the requirements  
for the degree of Master of Science  
in the Department of Mechanical, Materials and Aerospace Engineering  
in the College of Engineering and Computer Science  
at the University of Central Florida  
Orlando, Florida

Spring Term  
2005

© 2005 Madhavi Tiyyagura

## ABSTRACT

In NiTi, a reversible thermoelastic martensitic transformation can be induced by temperature or stress between a cubic (B2) austenite phase and a monoclinic (B19') martensite phase. Ni-rich compositions of the binary alloy have cubic structure at room temperature (requiring stress or cooling to transform to the monoclinic phase), while Ti-rich binary compositions are monoclinic at room temperature (requiring heating to transform to the cubic phase). The stress-induced transformation results in the superelastic effect, while the thermally induced transformation is associated with strain recovery that results in the shape memory effect. Ternary elemental additions such as Fe can additionally introduce an intermediate rhombohedral (R) phase between the cubic and monoclinic phase transformation.

This work was initiated with the broad objective of connecting the macroscopic behavior in shape memory alloys with microstructural observations from transmission electron microscopy (TEM). Specifically, the goals were to examine (i) the effect of mechanical cycling and plastic deformation in superelastic NiTi; (ii) the effect of thermal cycling during loading in shape memory NiTi; (iii) the distribution of twins in martensitic NiTi-TiC composites; and (iv) the R-phase in NiTiFe.

Both in-situ and ex-situ lift out focused ion beam (FIB) and electropolishing techniques were employed to prepare samples of the shape memory alloy for TEM characterization. The Ni rich NiTi samples were fully austenitic in the undeformed state. The introduction of plastic deformation (8% and 14% in the samples investigated) resulted in the stabilization of martensite in the unloaded state. An interlaying morphology of the austenite and martensite was observed as the martensite needles tend to orient themselves in preferred orientations. The aforementioned

observations were more noticeable in mechanically cycled samples. The observed dislocations in mechanically cycled samples appear to be shielded from the external applied stress via mismatch accommodation since they are not associated with unrecoverable strain after a load-unload cycle. On application of stress, the austenite transforms to martensite and is expected to accommodate the stress and strain mismatch through preferential transformation, variant selection, reorientation and coalescence. The stabilized martensite (i.e., martensite that exists in the unloaded state) is expected to accommodate the mismatch through variant reorientation and coalescence. On thermally cycling a martensitic NiTi sample under load through the phase transformation, significant variant coalescence, variant reorientation and preferred variant selection was observed. This was attributed to the internal stresses generated as a result of the thermal cycling. A martensitic NiTi-TiC composite was also characterized and the interface between the matrix and the inclusion was free of twins while significant twins were observed at a distance away from the matrix-inclusion interface. Incorporating a cold stage, diffraction patterns from NiTiFe samples were obtained at temperatures as low as -160 °C.

Overall, this work provided insight into deformation phenomena in shape memory materials that have implications for engineering applications (e.g., cyclic performance of actuators, engineering life of superelastic components, stiffer shape memory composites and low-hysteresis R-phase based actuators). This work was supported in part by an NSF CAREER award (DMR 0239512).



## ACKNOWLEDGMENTS

I take this opportunity to thank Dr. Raj Vaidyanathan, my advisor, for his help, advice and guidance on this research and with the thesis. His belief in the ideas leading to this study and in me is what is in this thesis. I thank my co-advisor Dr. Helge Heinrich for helping me learn the principles of TEM and FIB, his help and friendly attitude will always be remembered and be appreciated. I am happy to acknowledge Dr. Linan An for being my thesis committee member. His ever smiling face will be remembered.

I want to acknowledge the Advanced Materials Processing and Analysis Center's, (AMPAC), Materials Characterization Facility, (MCF) at UCF, which gave me the opportunity to learn different material characterization techniques. I feel it is a treasure, which is just waiting for every student to explore. MCF engineer's assistance specially Mr. Zia Rahman's help at the TEM and FIB is appreciated. I express my gratitude to all the administrative personal at AMPAC, Waheeda Illasarie, Kari Stiles, Karen Glidewell and Cindy Harle, their assistance to the students in AMPAC from the time they are admitted until they graduate and even after, that are truly appreciated. Special thanks to Waheeda, who asks everyone with a smiling face if she could help fix their problem at MCF.

I also want to thank Dr. Stephen Schwarz for his help in teaching the *in-situ* FIB technique. Among the students I'd like to mention especially Andrew Warren, Sankar Laxman, Romyana Petrova, Bo Yao and Jing Liu , who were all helpful in sharing their knowledge about the instruments and also helped me with different things at MCF. I am very thankful to my colleagues in my group, especially Vinu Krishnan for patiently going through my thesis and for all the help and support during my stay here. I thank all my friends and well wishers here.

Biggest thanks goes to my family members especially my mother for being the only person in this world who is so unique to me, my brother for being my best critique and friend with my thesis work, my sister for being so understanding and my doggy for his never changing attitude for no matter what comes. I thank god for all the love and support they had given me till now and for what they would give for the rest of my life.



## TABLE OF CONTENTS

LIST OF FIGURES .....	xi
LIST OF TABLES .....	xiv
LIST OF ACRONYMS/ABBREVIATIONS .....	xv
CHAPTER ONE: INTRODUCTION.....	1
1.1 Motivation.....	1
1.2 Introduction to Shape Memory Alloys .....	1
1.2.1 Shape Memory Effect .....	2
1.2.2 Pseudoelasticity, Superelasticity and Rubber-like behavior .....	5
1.3 Applications .....	6
1.4 Introduction to Transmission Electron Microscopy .....	9
1.4.1 History of TEM.....	10
1.4.2 Parts of an Electron Microscope .....	11
1.4.3 Techniques in TEM.....	16
1.4.3.1 Conventional Imaging (Bright Field and Dark Field TEM) .....	17
1.4.3.2 Electron Diffraction (SAD).....	18
1.4.3.3 Phase-Contrast Imaging (High Resolution TEM, HRTEM).....	19
1.4.3.4 Energy-Dispersive X-ray Spectroscopy (EDS).....	19
1.4.3.5 Electron Energy-Loss Spectroscopy (EELS).....	20
1.5 Introduction to the Focused Ion Beam Microscope (FIB).....	20
1.5.1 FIB Technique .....	21

1.6 Organization.....	22
CHAPTER TWO: LITERATURE REVIEW.....	23
2.1 Cycling of NiTi alloys .....	23
2.1.1 Influence of Precipitates and Texture on Cycling.....	26
2.1.2 TEM Study on Cycling of NiTi alloys.....	27
2.2 Introduction to NiTi Composites .....	29
2.2.1 Mechanical Behavior of NiTi-TiC composites.....	30
2.3 R-Phase Transformations.....	33
2.3.1 TEM studies in the R-Phase.....	35
CHAPTER THREE: SAMPLES AND SAMPLE PREPARATION .....	37
3.1 Sample A.....	37
3.2 Sample B.....	38
3.3 Sample C.....	38
3.4 Sample D.....	39
3.5 Sample E.....	39
3.6 Sample F .....	40
3.7 Sample G.....	40
3.8 Focused Ion Beam (FIB) Technique.....	41
3.8.1 <i>Ex situ</i> Lift Out Technique.....	41
3.8.2 <i>In situ</i> Lift Out Technique.....	43
3.9 Electropolishing .....	47
3.10 Mechanical Polishing using a Tripod .....	48
CHAPTER FOUR: EFFECT OF PLASTIC DEFORMATION AND CYCLING .....	49

4.1 Undeformed Austenitic NiTi .....	49
4.1.1 Results.....	49
4.1.2 Discussion .....	53
4.2 Deformed Austenitic NiTi .....	54
4.2.1 Results.....	54
4.2.2 Discussion .....	65
4.3 Martensitic NiTi.....	68
4.3.1 Results.....	68
4.3.2 Discussion .....	72
CHAPTER FIVE: NiTi-TiC .....	75
5.1 Results.....	75
5.2 Discussion.....	79
5.2.1 Eshelby Equivalent Inclusion Method .....	79
5.2.2 Determination of Internal Mismatch Stresses.....	80
5.2.3 Comparison with Spherical Indenter .....	86
CHAPTER SIX: R-Phase in NiTiFe.....	89
6.1 Results.....	89
6.2 Discussion.....	93
CHAPTER SEVEN: CONCLUSIONS AND FUTURE WORK.....	94
APPENDIX: LATTICE PARAMETERS .....	97
LIST OF REFERENCES.....	102

## LIST OF FIGURES

Figure 1: Transformation temperatures during the shape memory effect.....	3
Figure 2: Principle of the shape memory effect.....	4
Figure 3: Principle of pseudoelasticity .....	5
Figure 4: Parts of a typical TEM.....	11
Figure 5: Double tilt sample holder .....	14
Figure 6: (a) The bright field imaging technique and (b) the dark field imaging technique .....	17
Figure 7: Position of the lenses for the SAD technique.....	18
Figure 8: Focused ion beam microscope .....	20
Figure 9: Stress strain curves of NiTi SMA under monotonic tension and compression.....	25
Figure 10: The <i>ex situ</i> technique of FIB used for TEM sample preparation .....	43
Figure 11: The FIB <i>in situ</i> technique used for TEM sample preparation .....	47
Figure 12: (a-f) TEM images of NiTi_A_CD.....	51
Figure 13: (a) TEM image of NiTi_A_CD and the corresponding SADP is shown in (b) .....	51
Figure 14: (a) TEM image of NiTi_A_HIP (prepared using FIB) and the corresponding SADP is shown in (b) .....	52
Figure 15: TEM image of NiTi_A_HIP (electropolished sample) and the corresponding SADP is shown in (b) .....	52
Figure 16: SADP of NiTi_A_HIP (electropolished sample).....	53
Figure 17: (a) TEM image of NiTi_A_8% and the corresponding SADP is shown in (b).....	56
Figure 18: (a) TEM image of NiTi_A_8% and the corresponding SADP is shown in (b).....	56

Figure 19: (a) HRTEM image of the lattice in NiTi_A_8% (b) Fourier filtered HRTEM image of NiTi_A_8%. (c) Reduced fourier filter image of 19(a) showing the reflections.....	57
Figure 20: TEM image of NiTi_A_8%.....	58
Figure 21: (a) TEM image of NiTi_A_8% and the corresponding SADP is shown in (b).....	58
Figure 22: TEM image of NiTi_A_8%.....	59
Figure 23: (a) HRTEM image of NiTi_A_8% (b) Fourier filtered HRTEM image of NiTi_A_8% .....	61
Figure 24: Profile around the dislocation lines shown in Figure 24; (a) is the top profile while (b) is the bottom profile of the lattice of NiTi_A_8%.....	62
Figure 25: TEM images of NiTi_A_14%.....	63
Figure 26: (a) TEM image of NiTi_A_14% and the corresponding SADP is shown in (b).....	64
Figure 27: (a) TEM image of NiTi_A_14% and the corresponding SADP is shown in (b).....	64
Figure 28: Stress-strain response of the undeformed (NiTi_A_CD), 8% plastically strained and 8% plastically strained and 15 times cycled (NiTi_A_8%) samples.....	65
Figure 29: TEM images of NiTi_M_0.....	69
Figure 30: SADP corresponding to Figure 30(a).....	70
Figure 31: TEM images of NiTi_M_1214.....	71
Figure 32: SADP corresponding to Figure 31(a) and Figure 31(b).....	72
Figure 33: Schematic illustration of the shape memory effect in a single crystal.....	73
Figure 34: TEM images of NiTi_10TiC_M.....	78
Figure 35: Diagram showing the maximum stress under the indenter.....	87
Figure 36: The contact radius of the TiC particle for the spherical indenter analogy.....	88

Figure 37: SADP of NiTiFe at (a) room temperature, (b) -20°C, (c) -60°C and (d) -160°C for the [111] beam direction.....	90
Figure 38: SADP of NiTiFe at (a) room temperature, (b) -20°C, (c) -60°C and (d) -160°C for the [110] beam direction.....	91
Figure 39: SADP of NiTiFe at (a) room temperature, (b) -20°C, (c) -60°C and (d) -160°C for the [100]-beam direction.....	92

## LIST OF TABLES

Table 1: Twinning modes observed in NiTi B19' martensite.....	24
Table 2 : Properties of reflections in “kinematic diffraction” patterns of the austenite .....	98
Table 3: Properties of reflections in “kinematic diffraction” patterns of the martensite .....	99

## LIST OF ACRONYMS/ABBREVIATIONS

$A_f$	Austenite finish temperature
$A_p$	Austenite peak temperature
$A_s$	Austenite start temperature
$M_f$	Martensite finish temperature
$M_p$	Martensite peak temperature
$M_s$	Martensite start temperature
R-phase	Rhombohedral phase
$R_f$	R-phase finish temperature
$R_p$	R-phase peak temperature
$R_s$	R-phase start temperature
SMA	Shape Memory Alloy
SME	Shape Memory Effect
TEM	Transmission Electron Microscopy
MT	Martensitic Transformation
S-S	Stress-Strain
FIB	Focused Ion Beam
TWSME	Two Way Shape Memory Effect
FFT	Fast Fourier Transform
SADP	Selected Area Diffraction Pattern



BF	Bright Field
DF	Dark Field
HRTEM	High-Resolution Transmission Electron Microscopy

# **CHAPTER ONE: INTRODUCTION**

## **1.1 Motivation**

The work aims to use transmission electron microscopy (TEM) for the study of selected phenomena in shape memory alloys. One of the objectives is to correlate the macroscopic behavior and properties of NiTi alloys with microstructural features observed by TEM. Specifically, the effect of mechanical cycling and cold work on superelasticity, and the effect of thermal cycling on the shape memory effect will be assessed. Furthermore, the distribution of twins in martensitic NiTi-TiC composites will be examined. Another aspect of this investigation will be the R-phase transformation in NiTiFe shape memory alloys. Overall, the goal is to provide insight into deformation phenomena in these materials that have implications for engineering applications (e.g., cyclic performance of actuators, engineering life of superelastic components and low-hysteresis R-phase based actuators).

## **1.2 Introduction to Shape Memory Alloys**

Shape memory alloys have the interesting ability to “remember” their original size and shape, at a characteristic transformation temperature. Shape memory alloys are fascinating materials characterized by the shape memory effect and superelasticity, which ordinary metals and alloys do not possess. The shape memory effect was first observed in samples of gold-cadmium in 1932 and 1951, and in brass (copper-zinc) in 1938. However, it was in 1962 that William J. Buehler and co-workers at the Naval Ordnance Laboratory (NOL) discovered that

NiTi showed the shape memory effect [Srinivasan & McFarland 2001]. They found that an alloy consisting of equal quantities of nickel and titanium atoms exhibited the transformation that leads to the shape memory effect. Buehler named it NiTiNOL to include the acronym of the name of his laboratory.

Both the shape memory effect and superelasticity are closely related to the martensitic transformation. The martensitic transformation is a diffusionless phase transformation in solids, in which the atoms move cooperatively, and often by a shear-like mechanism. Usually in NiTi, the parent phase (high temperature phase) is cubic, and the martensite (low temperature phase) is monoclinic. Many variants of martensite can be formed from the parent phase. In NiTi, there are 24 different ways of producing martensite from austenite as a result of the symmetric CsCl structure having 6 equivalent phase diagonal planes (6  $\{110\}$  planes, which become basal planes for the martensite). Each of these planes can shift in one of two directions and can distort shear in one of two directions,  $6 \times 2 \times 2 = 24$  [Funakubo 1987].

### **1.2.1 Shape Memory Effect**

The shape memory effect (SME) is the ability of an alloy to remember its pre-deformation shape when it is heated from some relatively low temperature. All the accumulated strain is recovered during this phase transformation, and the recovery can take place against large forces [Funakubo 1987, Uchino 1998, Vaidyanathan 2002]. The shape memory effect is a phenomenon in which a material or specimen recovers its previous shape when heated above a certain

temperature. The specimen can be easily deformed below  $A_s$  (austenite start temperature) in the martensite phase (Figure 1). When it is heated, the martensite to austenite transformation begins at  $A_s$  (austenitic start temperature) and finishes at  $A_f$  (austenitic finish temperature), where it is completely transformed to austenite. Upon cooling, the reverse transformation back to martensite takes place at  $M_s$  (martensitic start temperature) and at  $M_f$  (martensitic finish temperature), all the austenite is completely transformed back to martensite [Buehler 1967]. The principle of SME is shown in Figure 2.

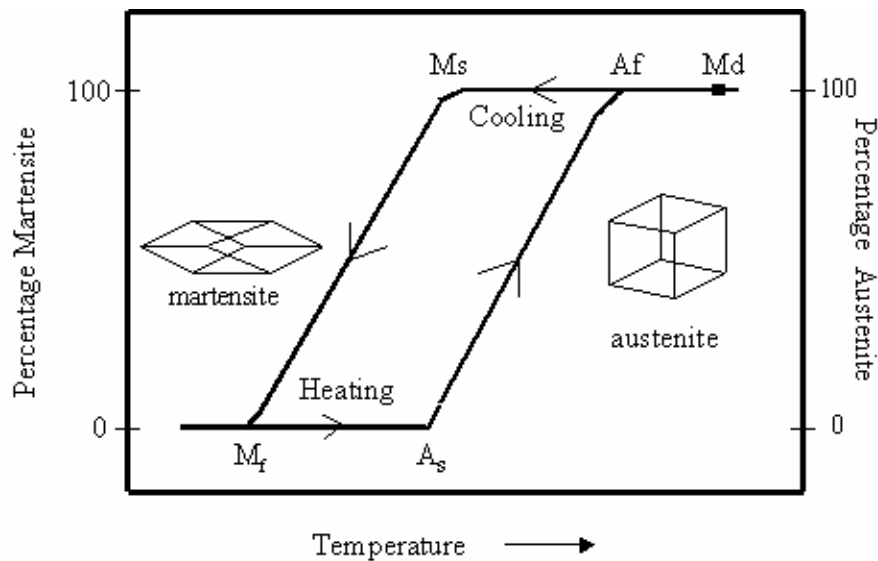


Figure 1: Transformation temperatures during the shape memory effect

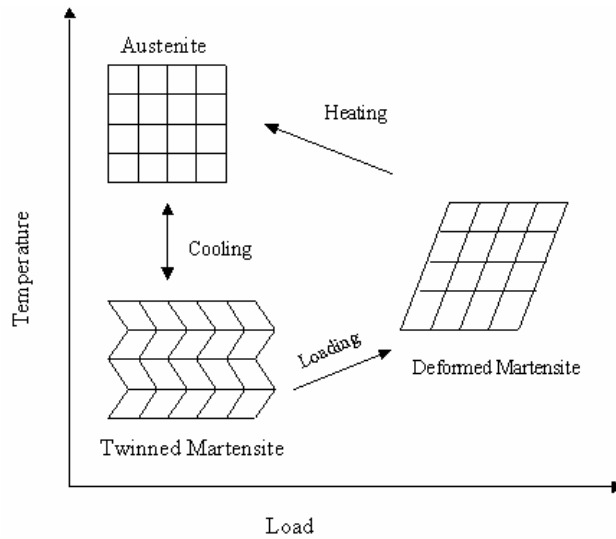


Figure 2: Principle of the shape memory effect

The shape memory effect can be of two types, namely, the one-way shape memory effect or the two-way shape memory effect. If the alloy remembers only its high-temperature shape, it is called the one-way shape memory effect. If in addition to the high-temperature shape the alloy remembers its low-temperature shape (deformed shape), it is called the two-way shape memory effect. The two way shape memory effect is achieved by “biasing” or “training” the shape memory alloy, wherein it is cycled several times between its high-temperature and low-temperature phases.

One of the reasons for it to remember its shape is that upon heavy deformation, dislocations are introduced so as to stabilize the configuration of the martensite phase. These dislocations exist even in the parent phase after the reverse transformation upon heating and the stress field around them induces particular habit plane variants upon cooling [Otsuka & Wayman 1998].

### 1.2.2 Pseudoelasticity, Superelasticity and Rubber-like behavior

When elastic deformation recovers just by unloading at a constant temperature (i.e., the stress-strain curve is characterized by a closed loop) it is called pseudoelasticity. It is a generic term, which encompasses both superelastic and rubber-like behavior. When a closed loop originates from a stress-induced transformation upon loading and the reverse transformation upon unloading, it is called superelasticity. If it occurs by the reversible movement of twin boundaries in the martensite state, it is called rubber-like behavior.

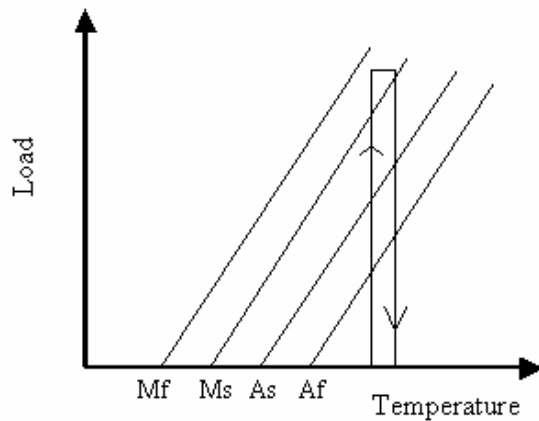


Figure 3: Principle of pseudoelasticity

Pseudoelasticity occurs in shape memory alloys when the alloy is completely composed of austenite (temperature greater than  $A_f$  and below  $M_d$ , the martensite desist temperature). Unlike the shape memory effect, pseudoelasticity occurs without a change in temperature. The load on the shape memory alloy is increased until the austenite is transformed to martensite simply due to the loading. The loading is absorbed by the martensite, but as soon as the loading is decreased,

the martensite begins to transform back to austenite since the temperature of the specimen is still above  $A_f$  and the specimen springs back to its original shape. This effect is outlined in Figure 3.

### **1.3 Applications**

Shape memory alloys have unique properties, which lend themselves to a variety of applications. CuZnAl and NiTi are the two alloys that are mostly used for practical SMA applications. NiTi is used in applications where operations are repeated many times such as electric switches and actuators and in applications that require high reliability.

#### **Pipe Couplings**

The one-way shape memory phenomenon is being made use of in developing pipe couplings. A ternary NiTiFe alloy is used, since any binary alloy with low  $M_s$  is essentially Ni-rich and unstable as stress relief heat treatments after machining can cause the  $M_s$  to shift. Fe is used to substitute Ni to depress  $M_s$ . This results in materials with relatively wide ranges of melting temperatures and processing windows [Funakubo 1987]. The couplings are established at room temperature and are in the austenite phase. Their inner diameter is slightly smaller than the outer diameter of the pipe. These couplings are expanded after putting them in liquid nitrogen when the austenite phase changes to the martensite phase. After putting the coupling in place to join the pipe, the coupling is heated to room temperature and an excellent joint is formed between the pipe and the coupling. These couplings are used in the plumbing of atomic

submarines and warships as well as maintenance and repair of pipes (with diameters as large as 150 mm) laid on the ocean floor to transport oil inland from oil fields.

### **Fasteners and Connectors**

Fasteners and connectors are used in place of rivets and bolts when the far side of the fastened objects cannot be accessed, like in mid-air structures. Here, the original fastener is in the austenite state. It is dipped in liquid nitrogen to straighten. It is then inserted into the hole and actuates as it gets back to room temperature and is installed tightly. Connectors in electrical appliances also follow the same principle.

### **Actuators**

Shape memory actuators sense a change in temperature and under go a phase change at a particular temperature to deliver a corrective force and displacement [Otsuka & Wayman 1998]. Thermal actuators are used to protect filters, which are used for water filtration as they can get damaged if they are exposed to hot water. When hot water flows, the SMA spring is heated, overcoming the bias spring force and closing the valve for filter protection.

The cooling system in diesel engines employs an electrically driven fan, which is turned off and on as required to maintain a specified system temperature. Thermally operated electrical switches must operate reliably while subjected to strong vibrations. The bimetal-operated switches used for this application suffer from chatter due to their low contact force and short stroke. These conditions have been completely corrected by the use of high contact force SMA switches.



## **Damping**

Shape memory alloys have good damping capacity both in the austenite state because of stress induced martensite transformation, and in the martensite state because of stress-induced martensite variant reorientation. Recently, attempts were being made to explore the feasibility of these materials for seismic protection [Liu *et al.* 1999].

## **Medical applications**

When SMAs are applied in the medical field, they must be capable of fulfilling requirements relating not only to mechanical reliability but also to chemical reliability (in-vivo degradation, decomposition, dissolution, corrosion, etc.) and biological reliability (biocompatibility, toxicity, carcinogenicity, antithrombogenicity, antigenicity, etc.) [Funakubo 1987]. Since biochemical stability is an important factor when SMAs are applied in medical fields, all applications are currently limited to NiTi.

SMAs are used in orthodontic treatments for malocclusions, impact canines and other problems where the superelastic characteristics of NiTi are exploited. NiTi is used for artificial joints for femoral heads and sockets. The SMAs are used as blood clot filters that when inserted into the body, open up at body temperature to arrest clots. They are used for bendable surgical tools and in implants such as stents, joints, clamps etc. Furthermore, they are used as eyeglass frames that recover their original shape when accidentally bent out of shape.

## **1.4 Introduction to Transmission Electron Microscopy**

The transmission electron microscope has become the premier tool for microstructural characterization of materials that use a beam of highly energetic electrons to examine objects on a very fine scale [Fultz & Howe 2001]. This examination can yield the following information:

- i) Topography: The surface features of the specimen, its texture; where there is relation between these features and material properties (hardness, reflectivity, etc.)
- ii) Morphology: The shape and size of the particles and grains; direct relation between the structure and material properties (ductility, strength, reactivity, etc.)
- iii) Composition: The elements and compounds that the specimen is composed of and relative amounts of them; direct relation to materials properties (melting point, reactivity, hardness, etc.)
- iv) Crystallographic information: The atomic arrangement in the specimen; which again relates to the material properties (conductivity, electrical properties, strength, etc.)

### 1.4.1 History of TEM

The resolution of light microscopes is limited by the physics of light to 0.2 micrometers. In the early 1930s, this theoretical limit had been reached and there was a scientific desire to study fine details of the interior structures of organic cells (nucleus, mitochondria, etc.). This required a resolution better than that of a light microscope. The transmission electron microscope was the first type of electron microscope to be developed. It is similar to the light transmission microscope except that a focused beam of electrons is used instead of light to "see through" the specimen.

Ernst Ruska's first scientific work (1928-1929) was concerned with the mathematical and experimental proof of Busch's theory on the effect of a magnetic field of a coil of wire through which an electric current is passed and which is then used as an electron lens. During the course of this work, he recognized that the focal length of the electrons could be shortened by use of an iron cap. From this discovery the polschuh lens was developed, a lens that has been used since then in all magnetic high-resolution electron microscopes. Further work, conducted together with Max Knoll, led to the first construction of an electron microscope in 1931 in Germany.

## 1.4.2 Parts of an Electron Microscope

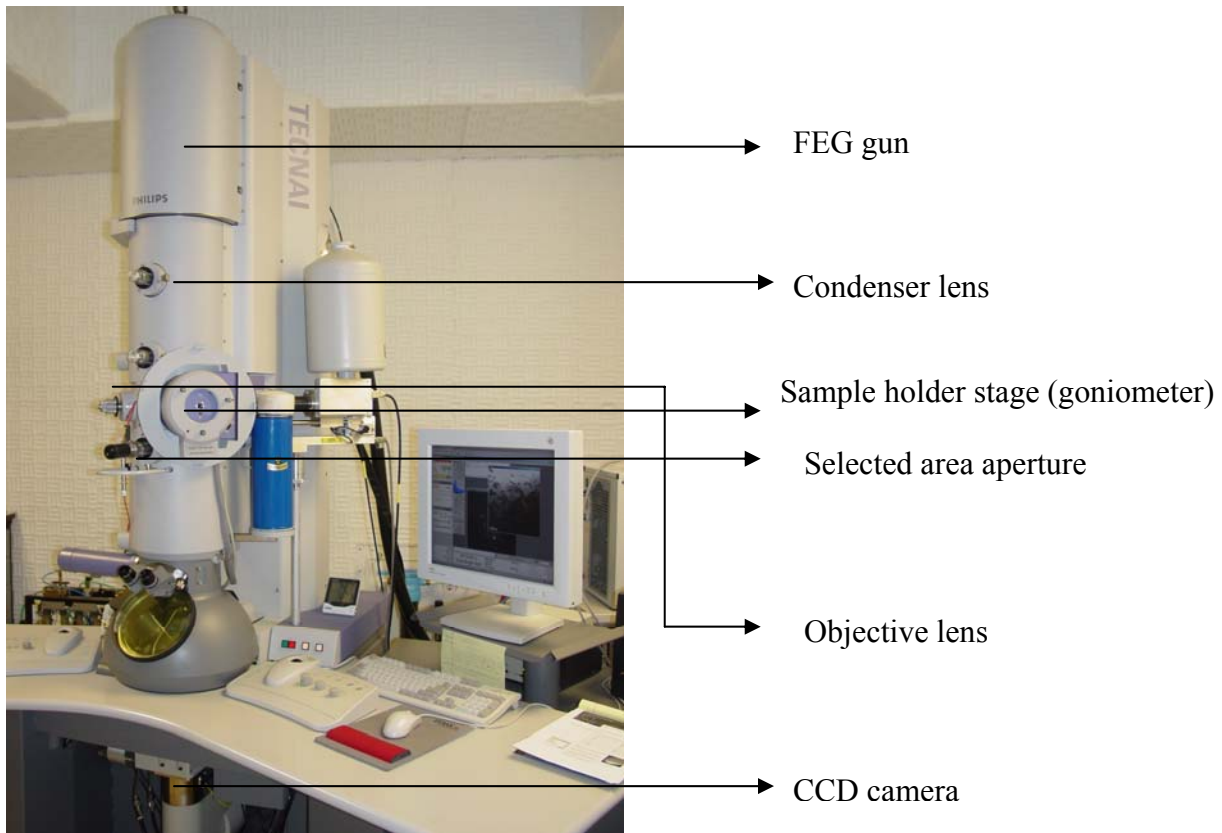


Figure 4: Parts of a typical TEM

**FEG (Field Emission Gun):** The FEG gun has a very fine tungsten tip with a tip radius lower than 100 nm. A first anode is positively charged by several kV with respect to the tip. This is called the “extraction voltage” since it generates the intense electric field-extracting electrons by enabling them to tunnel out of the tip. Increasing the extraction voltage when you first switch on has to be done slowly, so the mechanical shock doesn’t fracture the tip. This is the only practical step you have to carry out to run an FEG, and it can easily be computer-controlled. (i) Anode 1 provides the extraction voltage to pull electrons out of the tip. (ii) Anode 2 accelerates the

electrons to 100 kV or more. The electrons are accelerated through the applied potential by the second anode. The combined fields of the anodes and the Wehnelt cylinder between the anodes act like a more refined electrostatic lens to produce a crossover. This lens controls the effective source size and position, but it isn't very flexible. FEGs can be, depending on the type, operated at 300 K to 1700 K. By the use of apertures and lens systems, these electrons are "channeled" so that they can be utilized in illuminating the specimen.

**Condenser Lens:** The function of the condenser lens is to focus the electron beam emerging from the gun onto the specimen to permit optimal illuminating conditions for visualizing and recording the image. This depends upon the condenser's focal length (i.e., the distance from the center of the lens or lens aperture to the point of convergence of the rays at cross-over, for a source at infinity). The condenser lens of the electron microscope is a relatively weak lens having a focal length of the order of a few centimeters that can be adjusted over a considerable range. The position of the condenser lens is outlined in Figure 4. The condenser aperture of the condenser diaphragm is in the front-focal plane conjugate to the diffraction plane of the specimen.

**Objective Aperture:** The objective lens forms the initial enlarged image of the illuminated portion of the specimen in a plane that is suitable for further enlargement by the projector lens. The objective magnetic lens is the most critical component of the microscope. In the construction of the microscope one must consider the following criteria:

- i) To obtain a high magnification at the given image distance, which is fixed by the length of the column connecting the objective lens with the projector lens, the

specimen must be situated close to the focal plane of the objective. This is made possible by constructing a symmetrical lens so that the specimen can be positioned in the center of it. In most cases, the initial magnification provided by the objective lens is in the range of 100X.

- ii) The focal length should be as short as practical (1-5 mm) to ensure that the chromatic and spherical aberration is minimal.
- iii) A minimum clearance must be provided for inserting the specimen and position a physical aperture close to the objective lens.
- iv) Provisions must usually be made for inserting electrical or magnetic deflection and stigmatism devices in, or close to the objective for correcting minute asymmetries in the lens field.

An objective aperture is used in the back focal plane (it is also called the diffraction plane as a diffraction pattern is formed there) to select one or more Bragg reflections and to form magnified images of the sample only with contributions from Bragg reflections within this aperture.

### Sample Holder (Goniometer):



Figure 5: Double tilt sample holder

A double tilt sample holder is shown in Figure 5. A goniometer can tilt the specimen with high precision in any desired direction to  $\pm 40^\circ$ . Crystalline samples have to be tilted in the goniometer for:

- i) observation of lattice fringes and crystal structures
- ii) observation of diffraction contrast of lattice defects with distinct Bragg reflections or known orientations

- iii) determination of the Burgers vector of lattice defects
- iv) determination of crystal orientation by electron diffraction

**Selected Area Diffraction:** The diffraction pattern is always present in the column, and one needs to set the lenses properly to project the diffraction pattern onto the screen. Electrons that are diffracted by the crystalline planes of the sample satisfying the Bragg condition, as well as undiffracted (transmitted) electrons, are brought into focus by the objective lens in the plane of the objective aperture (known as the back focal plane). The diffraction pattern in the back focal plane arises because of the image formation on the image plane. In order to project the diffraction pattern on the TEM screen, the intermediate lens is focused on the back focal plane.

**CCD (Charged Couple Device) Camera:** For digital image processing and for the electron microscope alignment, it is of interest to record two-dimensional arrays of pixels directly, avoiding the dark-room work required for photographic emulsions or the read-out for imaging plates. For the camera system a fluorescent material like ZnS is used on a viewing screen. For using a CCD camera in a TEM, light has to be generated by a scintillator material like Ce-doped yttrium-aluminum garnet (YAG). The photons are transferred by a fiber optics system on the pixels of the CCD array. A CCD imaging system used here consists of an array of  $1024^2$  silicon based photodiodes (pixels), each  $24 \times 24 \mu\text{m}^2$ .



### **1.4.3 Techniques in TEM**

Electron microscopes use a focused beam of electrons instead of light (light microscopes) to "image" the specimen and gain information as to its structure and composition. Electrons are generated by a process known as thermionic or by field emission. They are then accelerated by an electric field and focused by electrical and magnetic fields on to the sample.

A crystalline material interacts with the electron beam mostly by diffraction rather than absorption. If the planes of atoms in a crystal are aligned at certain angles to the electron beam, the beam is transmitted; while at other angles, the beam is diffracted, sending electrons in another direction. In the TEM, the specimen holder allows the user to tilt the specimen to certain angles in order to establish the desired diffraction conditions; while an aperture placed below the specimen allows the user to select electrons diffracted in a particular direction. The resulting image shows diffraction contrast, which highlights faults in the crystal structure clearly. Faults in crystals affect both the mechanical and electronic properties of materials, so understanding how they behave gives powerful insight. Some modes a TEM can be operated in are discussed below.

### 1.4.3.1 Conventional Imaging (Bright Field and Dark Field TEM)

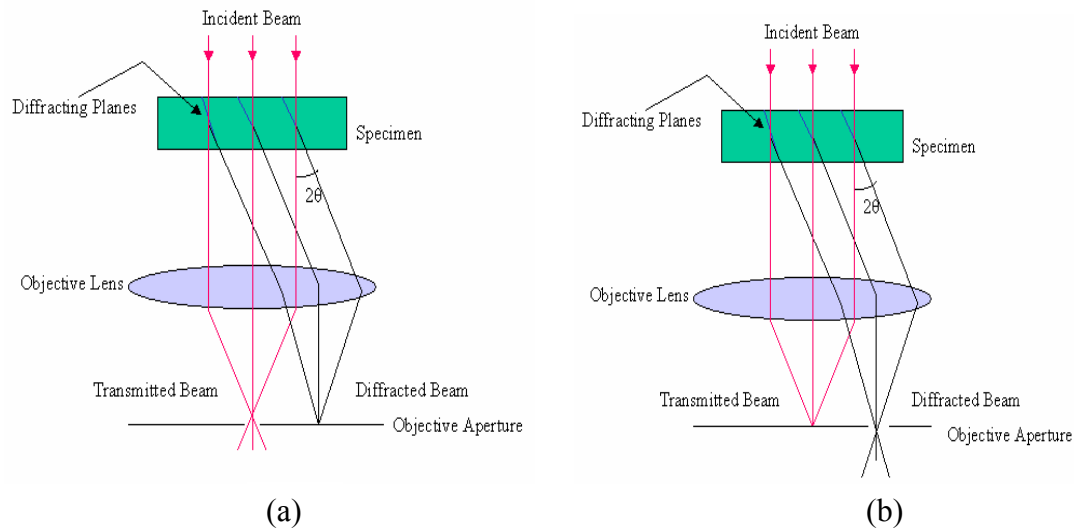


Figure 6: (a) The bright field imaging technique and (b) the dark field imaging technique

When the aperture is positioned to pass only transmitted (undiffracted) electrons, a bright-field (BF) image is formed, when the aperture is positioned to pass only some diffracted electrons, a dark-field (DF) image is formed [Fultz & Howe 2001]. In conventional studies of crystalline materials, most of the features of the image form from “diffraction contrast”. Diffraction contrast is the variation of the intensity of electron diffraction across the specimen, useful in making images of defects such as dislocations, interfaces and second phase particles. Diffraction contrast is observed by introducing an objective aperture in the beam. If the objective aperture is removed then the diffracted intensity recombines with the transmitted intensity at the viewing screen. This recombination suppresses the observed diffraction contrast. Regions that are diffracting through the objective aperture appear bright in DF, dark in BF. Regions that are not diffracting are dark in DF, bright in BF. The beam orientations in both BF and DF modes are shown in Figure 6.

### 1.4.3.2 Electron Diffraction (SAD)

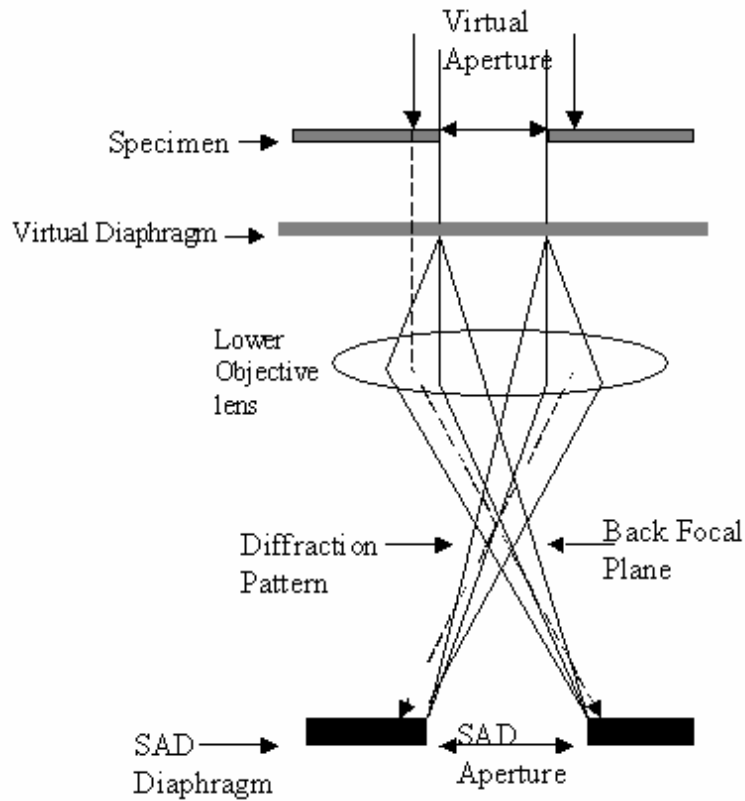


Figure 7: Position of the lenses for the SAD technique

For taking an SAD pattern the intermediate lens is focused on the back focal plane of the objective lens. Here, the objective aperture is removed and the intermediate aperture passes only electrons from a selected region of the sample as shown in Figure 7.

#### **1.4.3.3 Phase-Contrast Imaging (High Resolution TEM, HRTEM)**

An atomic resolution image is formed by the "phase contrast" technique, which exploits the differences in phase among the various electron beams scattered by the sample. A large objective lens aperture (or no aperture) allows the transmitted beam and at least four diffracted beams to form an image where the phase contrast is partially transformed to an amplitude contrast by defocusing. High-resolution images are most useful for identifying individual defects in crystals, and for studying atomic arrangements at interfaces. It is capable of determining the arrangement of atoms at solid-solid interfaces such as grain boundaries and inter-phase boundaries.

#### **1.4.3.4 Energy-Dispersive X-ray Spectroscopy (EDS)**

Highly energetic electrons that impact the sample yield a variety of by-products, one being X-rays. Some X-rays have element characteristic energies/wavelengths and can be detected using a solid-state energy dispersive spectrometer (EDS) detector [Fultz & Howe 2001]. An X-ray spectrum is acquired from small regions of the specimen illuminated with a focused electron beam. Characteristic X-rays from each element are used to determine the concentration of different elements in the specimen.

### **1.4.3.5 Electron Energy-Loss Spectroscopy (EELS)**

The electrons impinging on the sample can lose energy by a variety of mechanisms. These losses can reveal the composition of the sample in TEM. Plasmon losses are a frequent cause of energy loss. Plasmons are collective excitations of the electron gas in the material and are typically several eV in magnitude. Phonon losses can also occur, which are much smaller. Therefore the energy spread of the monoenergetic beam must be particularly small to detect such losses. Phonons are quantized sound waves within the solid. In TEM, the losses predominantly occur in the bulk of the sample, as the beam travels through the thin specimen to the EELS detector on the other side.

### **1.5 Introduction to the Focused Ion Beam Microscope (FIB)**



Figure 8: Focused ion beam microscope

The working principle of a FIB is much like the SEM (Scanning Electron Microscope). The FIB is shown in Figure 8. The only difference being FIB uses a focused beam of gallium ions while SEM uses a beam of electrons. The FIB has a Liquid Metal Ion Source (LMIS) and a reservoir of gallium that is in contact with a sharp tungsten needle [Giannuzzi & Stevie 1999]. The Ga wets the needle and flows to the W tip. A high extraction field ( $> 10^8$  V/cm) is used to pull the liquid Ga into a sharp cone whose radius is 5-10 nm. Ions are emitted because of field ionization and post ionization and are accelerated down the FIB column.

The two advantages of using Ga are:

- i) Ga has a low melting point and hence is liquid at room temperature
- ii) Ga ions can be focused to a very fine probe size ( $<10$  nm in diameter) [Giannuzzi & Stevie 1999]

By controlling the strength of the electrostatic lenses and by adjusting the aperture sizes, the probe current density can be altered from tens of pA to several nA, corresponding to a beam diameter of 5 nm to 0.5  $\mu\text{m}$ .

### **1.5.1 FIB Technique**

In this technique, a bulk sample is inserted directly into the FIB chamber and a specimen is prepared from the sample surface. A protective Pt layer is deposited and trenches are milled on either side of the deposited Pt layer. The sputtering mechanism may also implant some Ga ions in the sample. Following this, the specimen is thinned down to the extent that it is electron beam

transparent. It is lifted out with the help of a needle that utilizes electrostatic force. The final sample is placed on a carbon film grid for TEM studies.

## **1.6 Organization**

The work in this thesis is organized as follows. Chapter 2 presents a literature review. Chapter 3 discusses the samples used and sample preparation techniques. Chapter 4 discusses the influence of cycling and plastic deformation in NiTi. It presents discussion on both, superelastic and shapememory NiTi. Chapter 5 presents results and discussion on NiTi-TiC composites. Chapter 6 discusses the R-Phase in NiTi, including results and discussion. Finally, Chapter 7 presents the conclusions.

## CHAPTER TWO: LITERATURE REVIEW

### 2.1 Cycling of NiTi alloys

It is known that NiTi SMAs undergo a thermoelastic martensitic transformation from cubic B2, the austenite, to monoclinic B19', the martensite, upon cooling. The martensite plates are self-accommodated forming a triangular morphology. The internal defects of the B19' martensite reported so far are  $\langle 011 \rangle$  type II,  $\{11-1\}$  type I,  $\{111\}$  type I, (011) type I, (100) compound and (001) compound twins [Xie *et al.* 1998]. The details are listed in Table 1. Following the formal crystallographic theory of twinning the nomenclature that we follow for twinning is

$K_1$  is the twinning plane, or the first undistorted plane

$K_2$  is the second undistorted plane

$\eta_1$  is the shear direction

$\eta_2$  is the direction defined by the intersection of the plane of shear with  $K_2$

i) A twin is of the first kind when  $K_1$  is a rational plane and  $\eta_2$  a rational direction.

ii) A twin is of the second kind when  $K_2$  is a rational plane and  $\eta_1$  a rational direction.

iii) A compound twin is formed when all four elements  $K_1$ ,  $K_2$ ,  $\eta_1$  and  $\eta_2$  are rational.



Table 1: Twinning modes observed in NiTi B19' martensite

Twinning Mode	$K_1$	$\eta_1$	$K_2$	$\eta_2$	Twinning shear strain	Theoretical solution	Twinning mechanism
{11-1} type I	(11-1)	[0.5404 0.45957 1]	(0.24695 0.5061 1)	[-2-21]	0.3096	Yes	Lattice invariant shear. Variant accommodation or deformation twinning
{111} type I	(111)	[-1.5117 0.5117 1]	(-0.66875 0.3375 1)	[211]	0.1422	No	Reported in martensite after tension. Not observed in undeformed martensite
(011) type I	(011)	[1.5727 1 -1]	(0.7205 1 -1)	[011]	0.2804	Yes	Lattice invariant shear
<011> type II	(0.7205 1 -1)	[011]	(011)	[1.5727 1 1]	0.2804	Yes	Lattice invariant shear
(100) compound	(100)	[001]	(001)	[100]	0.2385	No	Deformation or variant accommodation twinning
(001) compound	(001)	[100]	(100)	[001]			

Under monotonic tension, within the stress plateau of the stress-strain curve, the deformation of martensite in NiTi SMAs may occur by

- i) Stress-induced growth of the most favorably oriented martensite variants
- ii) Stress-induced reorientation of martensite
- iii) Stress-induced twin boundary migration within a martensite variant

Under tension, a stress plateau occurs at about 1% strain extending to about 6% strain. While under compression, the specimen quickly strain hardens and no stress-plateau is observed.

It indicates that the martensite reorientation process takes place easily under tension than under compression [Xie *et al.* 1998]. This phenomenon is seen in the stress-strain curve in Figure 9.

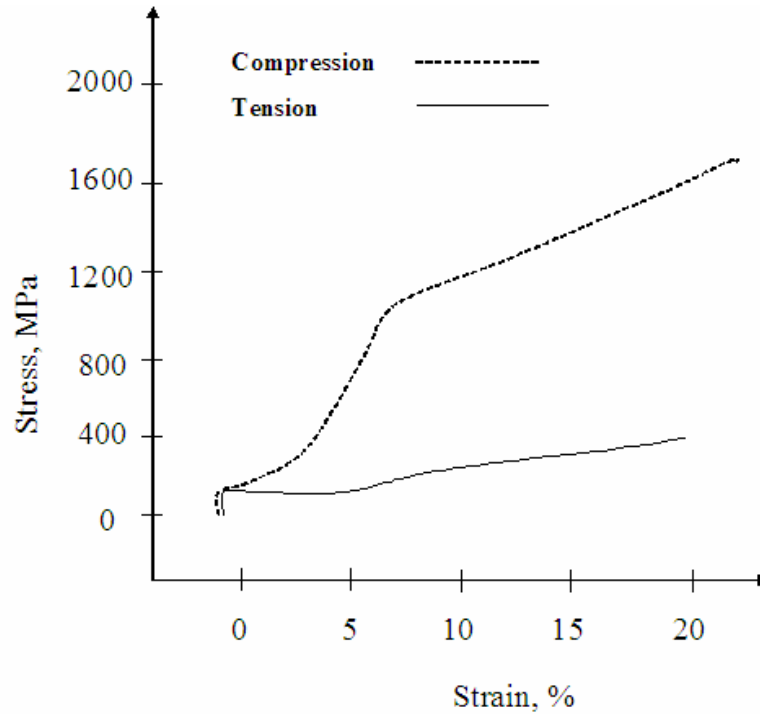


Figure 9: Stress strain curves of NiTi SMA under monotonic tension and compression

Work on cyclic deformation and fatigue of polycrystalline NiTi shape memory alloys where both low-cycle and high-cycle fatigue was studied shows that in the low-cycle regime the transformation stress-strain response evolves as a function of the first 15-20 applied loading cycles. This work postulated that the evolution of the stress-strain response in NiTi could be attributed to dislocation activity. Years later, it was postulated that the cyclic response of NiTi depends on heat treatment, material composition and testing temperature. From extensive studies of the cyclic pseudoelastic response of NiTi it was concluded that degradation of the pseudoelastic effect occurs as a result of mechanisms operating during the stress-induced transformation rather than during elastic loading. Dislocation activity was not explicitly observed

by electron microscopy, but rather inferred from experimental results and optical microscopy [Xie *et al.* 1998].

### **2.1.1 Influence of Precipitates and Texture on Cycling**

Ti<sub>3</sub>Ni<sub>4</sub> precipitates in NiTi alloys give superior fatigue resistance. Some mechanical cycling experiments revealed that compressive cyclic degradation resistance is strongly dependent on crystallographic orientation. Under compression, orientations approaching the [100] pole of the stereographic triangle possess the highest fatigue resistance. Orientations approaching the [111] pole of the stereographic triangle demonstrate the lowest fatigue resistance. Orientations near the [110] pole possess intermediate resistance to cyclic degradation [Gall & Maier 2002].

It was found that aging generally produces coherent 10 nm Ti<sub>3</sub>Ni<sub>4</sub> precipitates, which improves the fatigue resistance of NiTi compared to other heat treatments (solutionized or overaged) for nearly all orientations. Heat treatments and the subsequent Ti<sub>3</sub>Ni<sub>4</sub> precipitate size affect the cyclic degradation resistance of NiTi. NiTi with 10 nm Ti<sub>3</sub>Ni<sub>4</sub> precipitates consistently showed stabilized martensite due to mechanical cycling, and an absence of dislocation activity. The stabilized or ‘pinned’ martensite existed in the samples even though it was heated to 75°C above A<sub>f</sub> after pseudoelastic cycling. Incoherent Ti<sub>3</sub>Ni<sub>4</sub> precipitates (500 nm) consistently show significant dislocation activity due to mechanical cycling in addition to stabilized martensite colonies [Gall & Maier 2002].

Though small precipitate sizes prevent dislocation motion, martensite interfaces can still be pinned by the small precipitates and cause permanent strain accumulation. Materials with large

precipitate sizes do not exhibit permanent pinning of the martensite as a dominant mode, but rather plastic flow is more dominating. Owing to these competing microstructural mechanisms, a heat treatment [Miyazaki & Otsuka 1986] is not always the most effective means to improve the cyclic degradation resistance of NiTi.

### 2.1.2 TEM Study on Cycling of NiTi alloys

TEM studies carried out on undeformed and deformed samples consisting of B19' martensite at room temperature showed that the martensite reorientation process takes place more easily under tension than under compression [Xie *et al.* 1998]. Martensite plates in the deformed samples are smaller than compared to those in the undeformed samples. The microstructural details in both cyclically deformed and undeformed materials are discussed in the following. Three types of martensite twins, i.e., {011} type II, {11-1} type I and {001} compound twins, were found in the undeformed samples. Among them, the {011} type II twinning is the most frequently observed one. From TEM studies it was noted that the {011} type II twin bands were undeformed and the junction plane was generally straight with a comparatively small strain contrast area. The martensite variants were self-accommodated with each other. In each martensite variant, parallel plates extend through the whole martensite plates with a rather straight junction plane. Compared to (011) type II and (11-1) type I twin platelets observed, the (001) twin platelets are much narrower [Xie *et al.* 1998].

In deformed samples the martensite variants are still self-accommodating and (11-1) type I twinning is more frequently observed. In addition, (011) type II, (111) type I and (001)

compound twins are also present, and various types of lattice defects developed as a result of mechanical cycling. The junction plane between the variants was close to (001). A high density of dislocations appears inside the twin plates and in the junction plane area. In addition to the dislocations, shear bands along the (110) plane were also seen in the twins. Dislocation arrays along the (11-1) plane were found inside the twin bands and a high density of dislocations were formed along the (11-1) and (110) planes. Shear bands along the (110) plane appeared regularly in the twin bands [Xie *et al.* 1998].

TEM observations suggest that the most favorably oriented twinning system under a tension-compression cyclic load would be the (11-1) type I twinning. This is because the value of twinning shear strain for the (11-1) type I twin, is 0.3096, is the largest one for all the twinning systems observed so far in B19' martensite. (111) type I twinning can be found only in materials under tension [Xie *et al.* 1998], which has been seen by X-ray diffraction analysis. It has not been observed in TEM because (111) type I twins do not have solutions in phenomenological crystallographic theory [Xie *et al.* 1998]. The twin band thickness in the deformed martensite is seen to be higher than in undeformed martensite indicating that in addition to stress-induced re-orientation of martensite plates, stress-induced twin boundary migration also occurs under tension-compression cycling. Dislocations annihilate on twin boundaries and cluster in junction plane areas. New lattice defects can explain the martensite cyclic strain hardening process during tension-compression cycling [Xie *et al.* 1998].

## **2.2 Introduction to NiTi Composites**

Extensive knowledge exists concerning the deformation of metal matrix composite systems with stiff ceramic reinforcing phases (such as Al-SiC) where the matrix deforms by slip after initial elastic deformation. However, little is known about composites with matrices exhibiting alternative deformation mechanisms (e.g., twinning or stress induced transformations). The thermoelastic phase transformation and/or twinning deformation in NiTi can be expected to be affected by the presence of stiff ceramic particles which not only produce residual internal stresses (due to thermal mismatch) but also add to externally applied stresses. Consequently, the mechanical deformation behavior of such composites is both of theoretical interest (to better understand such deformation mechanisms) and practical interest (as superelastic composites) [Vaidyanathan *et al.* 1999a].

Dunand and co-workers [1996] have systematically characterized such NiTi-based shape-memory composites (a martensitic NiTi matrix reinforced with TiC). Mechanical strain in martensitic NiTi can be separated in three components: (i) strain by twinning which is recoverable; (ii) plastic strain by slip, which is unrecoverable; and (iii) residual elastic strains, which do not on average contribute to the total macroscopic prestrain, but may be recovered by relaxation during phase transformation. These three types of strains affect the kinetics and thermodynamics of the transformation as follows: (i) twinning reduces the number of martensitic variants, thus facilitating their subsequent transformation to austenite, and may also induce residual elastic stresses, due to residual mismatch strains between twinned variants; (ii) dislocations introduced by slip both stabilize the deformed martensite and induce the two way shape memory effect (TWSME) by their elastic stress field; and (iii) elastic stresses stabilize the

martensite, as described by the Clausius-Clapeyron equation, and can also induce the TWSME [Dunand *et al.* 1996].

Relaxation of the elastic and plastic mismatches between two phases (or between composite and matrix) may occur by twinning or slip of the matrix. The thermal transformation of mismatch twins formed during mechanical deformation to accommodate the elastic particles is similar to thermal transformation of twins responsible for the overall shape change of the specimen when twinning accommodates the mismatch. Then, the overall shape memory recovery of the composite is going to differ from the unreinforced matrix. In the second case, where matrix slip relaxes the mismatch with the reinforcement, dislocations are expected to stabilize the deformed martensite and enhance the TWSME. Further if relaxation by slip or twinning is incomplete after deformation, the resulting residual elastic stresses are also expected to affect the macroscopic recovery behavior by stabilizing the martensite and by inducing the TWSME.

### **2.2.1 Mechanical Behavior of NiTi-TiC composites**

Dunand *et al.* [1996] have systematically studied NiTi-based shape-memory composites where a martensitic NiTi matrix deforms by twinning in the presence of TiC particles. The first studies on the mechanical behavior of NiTi-based composites where an austenitic matrix deforms by forming stress-induced martensite in the presence of a reinforcing ceramic phase was carried out by Vaidyanathan *et al.* [1999b] by neutron diffraction of mechanically-loaded NiTi samples. They investigated the evolution of martensite fractions and discrete phase strains in superelastic NiTi and NiTi-TiC composites under compression loading. No reaction was observed by

microscopy and microprobe analyses between the NiTi matrix and the TiC particles, which were almost perfectly stoichiometric with a composition of  $49.8 \pm 0.1$  at.% C (as determined by combustion analysis with infrared detection). Because of the inert nature of TiC the matrix chemical composition was assumed to be constant and the mechanical behavior observed was not attributed to chemical effects [Vaidyanathan *et al.* 1999b].

The difference in macroscopic stress-strain curves observed for different volume fraction additions of TiC particles has been attributed to the differences in volume fractions of stress-induced martensite formed during loading due to the presence of the reinforcing particles. The volume fraction of martensite formed at any given applied stress decreases with increasing TiC content. The modulus of the austenite phase measured by the Rietveld method was expected to change at higher load levels due to: (i) load transfer to the stress-induced martensite which exhibits different elastic constants; (ii) transformation mismatch stresses between the two phases; and (iii) the evolving texture in the austenite [Vaidyanathan *et al.* 1999a].

For low loads, on NiTi–20TiC little martensite is formed, so the composite deforms mostly elastically. On the other hand, NiTi–10TiC showed significant amounts of stress-induced martensite at high applied stresses which could lead to additional mismatch with the TiC particles and thus deviation from the elastic response, as observed in plastically deforming aluminum composites. The lack of such plastic load-transfer suggests that the austenite/martensite matrix effectively accommodates the mismatch arising due to the large transformation strains in superelastic deformation. This may be attributed to the self-accommodating nature of the transformation, wherein certain variants can preferentially form to minimize the mismatch between matrix and reinforcement, as observed in shape-memory NiTi–TiC composites deforming by martensite twinning [Vaidyanathan *et al.* 1999b].



The studies by Fukami-Ushiro *et al.* [1996] at room temperature, show that the martensitic matrix deforms plastically by slip and/or twinning. At elevated temperature, plastic deformation of the austenitic matrix takes place by slip and/or formation of stress-induced martensite. The effect of TiC particles on the stress-strain curves of the composites depended upon which of these deformation mechanisms is dominant. First, in the low-strain elastic region, the mismatch between the stiff, elastic particles and the elastic-plastic matrix is relaxed in the composites: (i) by twinning of the martensitic matrix, resulting in a macroscopic twinning yield stress and apparent elastic modulus lower than those predicted by the Eshelby elastic load-transfer theory; and (ii) by dislocation slip of the austenitic matrix, thus increasing the transformation yield stress, as compared to a simple load-transfer prediction, because the austenite phase is stabilized by dislocations. Second, in the moderate-strain plastic region where nonslip deformation mechanisms are dominant, mismatch dislocations stabilize the matrix for all samples, thus (i) reducing the extent of twinning in the martensitic samples or (ii) reducing the formation of stress-induced martensite in the austenitic samples. This leads to a strengthening of the composites, similar to the strain-hardening effect observed in metal matrix composites deforming solely by slip. Third, in the high-strain region controlled by dislocation slip, weakening of the NiTi composites results, because the matrix contains (i) untwinned martensite or (ii) retained austenite, which exhibits a lower slip yield stress than twinned or stress-induced martensite, respectively [Fukami-Ushiro *et al.* 1996].

### **2.3 R-Phase Transformations**

The transformation sequence of certain NiTi alloys is as follows: B2 parent phase → incommensurate (IC) → commensurate (R-phase) → B19' martensite. The R-phase transformation with a tiny temperature hysteresis as small as 1 K and superior thermal cycling characteristics in NiTi alloys have attracted considerable attention, since it is useful in cryogenic applications. The associated shape-memory effect and superelasticity are useful for actuator applications. The R-phase transformation was first found by Dautovich and Purdy (1965) and then characterized by Sandrock and Hehemann (1971), from the sharp increase in resistivity and the appearance of superlattice reflections at  $1/3 \ 1/3 \ 0$  and equivalent positions in electron diffraction patterns. The structure of the R-phase has been a controversy for a long time. The crystal structure was established recently with powder X-ray diffraction. According to them the trigonal structure of the R phase is produced as a result of the association of three  $[110] [1-10]$ -type transverse displacement waves in the cubic parent phase [Murakami & Shindo 2001]. X-ray studies show that the incommensurability is neither regular nor periodic and it depends on the Brillouin zone [Stroz 2003].

NiTi SMAs can exhibit the R-phase at room temperature under the following conditions:

- i) Introduction of rearranged dislocations which are produced by thermal cycling or cold working and then annealing at low temperatures,
- ii) Introduction of precipitates by heat treatment at temperatures between 300°C and 500°C for Ni-rich alloys,

iii) Addition of certain third elements like Fe, Al, etc., that reduce the martensitic transformation temperatures [Wu *et al.* 2000].

Recently, a rapid solidification method was reported to induce the B2→R transformation in NiTi alloys. This was attributed to an introduction of crystallographic defects such as dislocations by rapid solidification [Nam *et al.* 2002]. All these factors are effective in revealing the R-phase transition because they depress the  $M_s$  point lower than the  $T_R$  (critical temperature) [Miyazaki & Otsuka 1986].

Some of the phenomena associated with the formation of the R-phase are extra diffraction spots at 1/3 positions of the B2 reciprocal lattice, an increase in electrical resistance prior to the martensite transformation, and a splitting in the {011} and {211} B2 reflections [Miyazaki & Otsuka 1986].

The R-phase transformation is a martensitic transformation of the first order [Otsuka & Wayman 1998], as a prominent change in crystal structure takes place below a definite transformation temperature  $R_s$ . However, it has been pointed out that some structural modulation occurs even above  $R_s$ , as detected by abnormal phonon softening and the presence of incommensurate diffuse scattering. Peak positions of diffuse scattering close to superlattice reflections below  $R_s$  have been believed to be closely related to the formation of the R-phase. It

is claimed that specific defects such as dislocations and precipitates could be favorable nucleation sites for the R-phase [Murakami & Shindo 2001].

Recent studies revealed that the R-phase transformation can occur in two stages. Kim *et al.* [2004] reported this behavior for a nickel-rich alloy subjected to low temperature ageing. The authors explained the two stages of the R-phase transformation as caused by a non-homogeneous distribution of nickel in the matrix following the heat treatment. They also show the influence of internal stress fields on the time evolution of the two stages of the R-phase transformation components. The R-phase transformation is caused by a non-homogeneous distribution of dislocations in a near-equiatomic NiTi alloy [Chrobak & Stroz 2005]. The two main factors influencing the multi-stage transformation behavior are inhomogeneities in chemical composition and internal stresses. Depending on the mutual interaction of these two, the course of the transformation can be different [Chrobak & Stroz 2005]. A new explanation is proposed based on *in situ* TEM observation that the second DSC peak in the cooling direction may include two transformations: R-phase to B19' in the grain boundary regions with precipitates, and B2 directly to B19' in the precipitate-free grain interiors. The R-phase nucleates at  $Ti_{11}Ni_{14}$  precipitates because they have the same rhombohedral structure with  $a=0.738$  nm and  $c=0.532$  nm for the R-phase and  $a=1.124$  nm and  $c=0.5077$  nm for  $Ti_{11}Ni_{14}$ . The compatible crystal structure and close lattice parameters makes the formation of R-phase at the boundary of  $Ti_{11}Ni_{14}$  easier than the formation of the monoclinic martensite phase [Tan & Crone 2004].

### **2.3.1 TEM studies in the R-Phase**

TEM studies of the R-phase conducted by Stroz [2003] lead to the following conclusions. The TEM images of the sample at room temperature do not reveal the presence of the R-phase; the only visible details are some tweed like structures and a number of dislocations. The corresponding diffraction patterns show only spots of the matrix in the [111] orientation. However, if this pattern is acquired and the background is subtracted, it reveals very weak superlattice reflections situated at  $1/3$  of 110 spots. It was proposed that electrical resistance starts to rise at the temperature when the incommensurate phase is formed in the sample. Recent studies by Cai *et al.* [1999] believe that the electrical resistance starts to increase with the start of the commensurate phase. Electron diffraction patterns from the regions and FFT (Fast Fourier Transform) images show that the positions of the superlattice reflections deviate from the exact  $1/3$  position of  $\langle 110 \rangle$  spots. At room temperature, up to 308 K the specimen is mostly in an incommensurate state. So, it is believed that the observed high-resolution micrographs image a modulated phase rather than the R-phase. This is confirmed by diffraction patterns that show the positions of the extra spots being shifted from the exact positions of the R-phase [Stroz 2003]. The incommensurate state exists in a wide temperature range above the  $R_s$  temperature. As the intensities of the extra spots are not very strong, the observed modulations are also weak [Cai *et al.* 1999].

Observations of the  $1/2\langle 110 \rangle$  reflections have been reported infrequently in the past. Tamiya *et al.* concluded that this is due to the thin foil effect as  $1/2\langle 110 \rangle$  reflections are not visible on the X-ray patterns. A plate like morphology was formed in the whole specimen volume at much lower temperatures, than the R-phase transition. This proves that an additional transformation takes place prior to the martensite formation [Stroz 2003].

## **CHAPTER THREE: SAMPLES AND SAMPLE PREPARATION**

The samples used for these studies are NiTi shape memory alloys that have different processing histories. The TEM specimens must be very thin and able to withstand the high vacuum present inside the instrument. In general, these materials are naturally resistant to vacuum, but they must be prepared as a thin foil, or etched so that some portion of the specimen is thin enough for the electron beam to penetrate.

### **3.1 Sample A**

These samples are a NiTi alloy with 51 at.% Ni and were produced from commercially available NiTi bars, which were supplied by Special Metal Corporation, New Hartford, NY. These bars were cold drawn from cast ingots that were produced via vacuum induction melting followed by vacuum arc remelting. The bars were subsequently used to fabricate cylindrical compression NiTi specimens. These specimens (10 mm in diameter and 24 mm in length) were fabricated by electro discharge machining, solutionized at 1000°C for 1 hour in argon and quenched in an oil bath at room temperature. Following this, annealing was done at 400°C in air for 1hr followed by quenching in ice water. From the starting composition, this material is expected to be austenite at room temperature. It is hereafter designated NiTi\_A\_CD to represent that it is austenitic (A) and cold drawn (CD).

### **3.2 Sample B**

These samples were obtained from pre-alloyed NiTi powders (99.9% pure, 49.4 at.% Ni, size between 44 and 177 $\mu$ m, from Special Metals Corp., NY) blended with Ni powders (99.9% pure particles, size between 44 and 177 $\mu$ m, from Special Metals Corp., NY). The powders were then packed in a cylindrical low carbon steel container (thickness 0.318 cm, internal diameter 2.5 cm, length 12 cm, lined with a boron nitride coated nickel foil to prevent carbon contamination) and were subjected to Hot Isostatic Pressing (HIP) at 1065°C and 100 MPa for 3 h. The NiTi billet had a nominal composition of 51.0 at.% Ni.

The billets were electro-discharge-machined into cylindrical specimens 10 mm in diameter and 24 mm in length. These specimens were solutionized at 1000°C for 1 h and oil-quenched to room temperature in titanium-gettered flowing argon, annealed at 400°C for 1 h in air and quenched in ice-water [Vaidyanathan *et al.* 2001]. From the starting composition this material is expected to be austenitic at room temperature. It is hereafter designated NiTi\_A\_HIP to represent that it is austenitic (A) and subjected to hot isostatic pressing (HIP).

### **3.3 Sample C**

These samples were processed in the same way as the alloy mentioned in Section 3.1 above. In addition the alloy was strained 8% plastically and 15 load-unload cycles were applied to a stress of 1500 MPa. From the starting composition, this material is expected to be austenitic at

room temperature prior to deformation. It is hereafter designated NiTi\_A\_8% to represent that it is austenitic (A) and has 8% plastic strain (8%).

### **3.4 Sample D**

The samples were processed in the same way as the alloy mentioned in Section 3.1 described above. After the processing, 14% plastic strain was applied to the specimen. From the starting composition this material is expected to be austenitic at room temperature prior to deformation. It is hereafter designated NiTi\_A\_14% to represent that it is austenitic (A) and has 14% plastic strain (14%).

### **3.5 Sample E**

These samples are a NiTi alloy with 50.31at.% Ni and comprised of commercially available wires of diameter 0.03” from NDC Corporation, Fremont, CA. The wires were heat treated at 550°C for 15 minutes and water quenched for shape setting in spring form. From the starting composition, this material is expected to be martensitic at room temperature. Three sets of samples were prepared for analysis:

- i) The shape set wire. It is designated as NiTi\_M\_0 to represent that it is in the martensitic state at room temperature and there was no cycling on this sample.
- ii) 1214 cycles applied on the wire by putting a weight of 100 grams and heating/cooling through the martensitic transformation. It is designated as NiTi\_M\_1214 to represent that



it is in the martensitic state at room temperature and there were 1214 cycles applied on this sample.

The DSC (differential scanning calorimetry) conducted on NiTi\_M\_0 sample showed that the  $A_s$  is 47.34°C and  $A_f$  is 51.72°C. The  $M_s$  for NiTi\_M\_0 sample is 2.59°C and  $M_f$  is -2.23°C. The DSC results of NiTi\_M\_1214 sample showed that  $A_s$  is 45.85°C and  $A_f$  is 51.55°C. The  $M_s$  and  $M_f$  for NiTi\_M\_1214 sample are 4.73°C and -0.92°C. Both the samples were dipped in liquid nitrogen to ensure that they are in the martensite state prior to doing the sample preparation for the TEM.

### **3.6 Sample F**

The samples were processed the same way as described in Section 3.2. However they were reinforced with 10 vol.% TiC in a NiTi (51.0 at.% Ni) matrix [Vaidyanathan *et al.* 2000]. The TiC powders (99.9% pure) were supplied by Atlantic Equipment Engineers, NJ, and the average size of the particles was 44  $\mu\text{m}$  [Vaidyanathan *et al.* 2000]. From the starting composition, this material is expected to be martensitic at room temperature. It is hereafter designated NiTi\_10TiC\_M to represent that it is martensitic and has 10 vol. % TiC particles in the NiTi matrix.

### **3.7 Sample G**

The samples were from a NiTiFe billet that was prepared by vacuum induction melting (VIM) and vacuum arc remelting (VAR). The billet was obtained from Special Metals

Corporation, NY with 46.8 at.% Ni and 3.2 at.% Fe. The samples were taken from the billet, which was electro-discharge-machined to form strips. These strips were solutionized at 850°C for 30 minutes and subsequently vacuum cooled. The strips were then cut with a pair of heavy-gauge clippers. From the starting composition this material is expected to be in the R-phase when cooled. It is hereafter designated as NiTiFe.

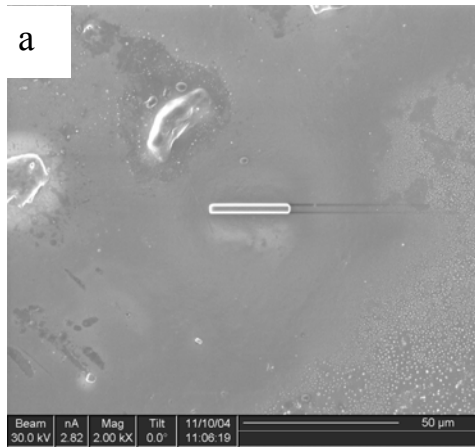
### **3.8 Focused Ion Beam (FIB) Technique**

The samples for the TEM studies were prepared by FIB by either the *ex-situ* process or the *in-situ* process. Both the processes are described in detail, the aims of which are to prepare a sample that is electron beam transparent.

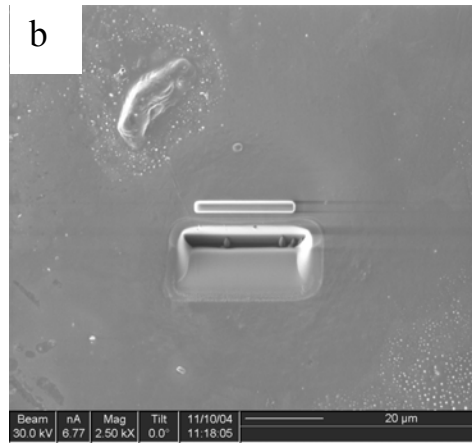
#### **3.8.1 *Ex situ* Lift Out Technique**

The FIB chamber was vented and the sample was loaded in the FIB chamber. The sample was set at the proper height using the marker so that it would not hit any of the needles, lenses or detectors. The chamber was pumped down to a reading of  $5 \times 10^{-5}$  mbar. The high voltage was switched on after the vacuum was achieved. A platinum layer was deposited on the specimen surface. Two trenches were milled on either side of the deposited platinum layer. The milling was done with higher currents of 20000 pA when away from the deposited platinum and was done with lower currents of 7000 pA when closer to the deposited Pt layer. Once the sample was thinned down to around 0.5  $\mu\text{m}$ , the sample was tilted to 45° and the bottom portion was cut. The

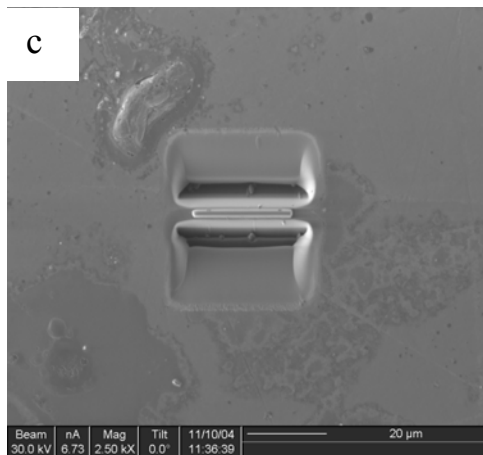
sample was again tilted by  $1^\circ$  on either side and further thinning was done. The final thinning was done at a 30 pA current by tilting the specimen in either direction by  $2-3^\circ$ . This thinning was done till the specimen was seen to be bending. Following this, the sample was tilted back to zero degrees and was finally cut away. It was then taken out from the FIB chamber and the sample was lifted out with the help of a needle with electrostatic force. It was subsequently placed on a copper grid with carbon film. Figure 10 explains the *ex situ* process of lifting out the TEM samples.



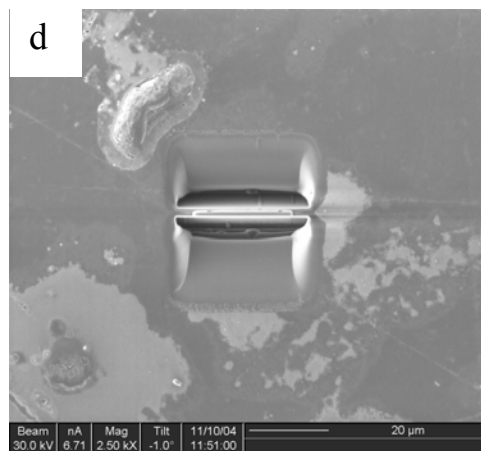
a. Pt deposited on sample



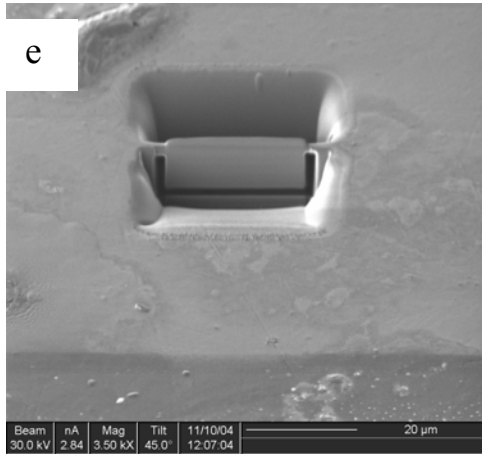
b. One trench milled



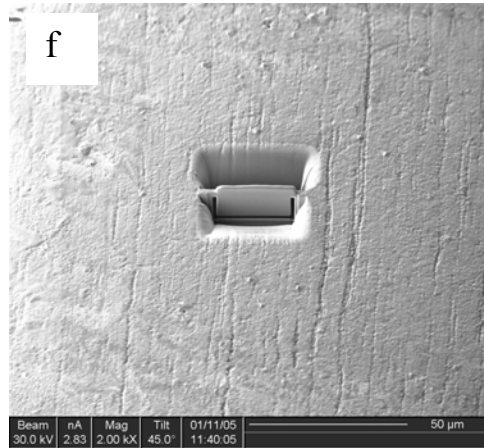
c. Trenched milled on both sides



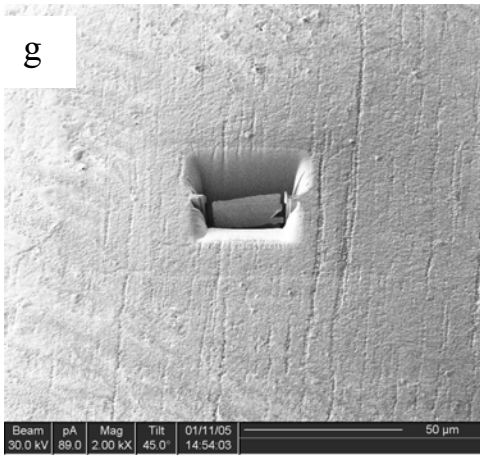
d. Thinning down before the bottom cut



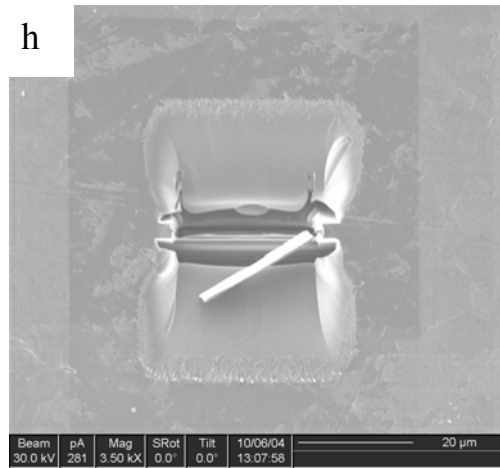
e. Tilted at 45° for bottom cut



f. Further thinned and shown at 45° angle



g. Sample cut-off viewed at 45°



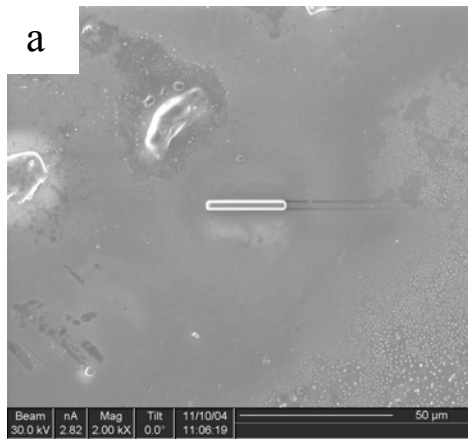
h. Sample cut-away viewed at 0°

Figure 10: The *ex situ* technique of FIB used for TEM sample preparation

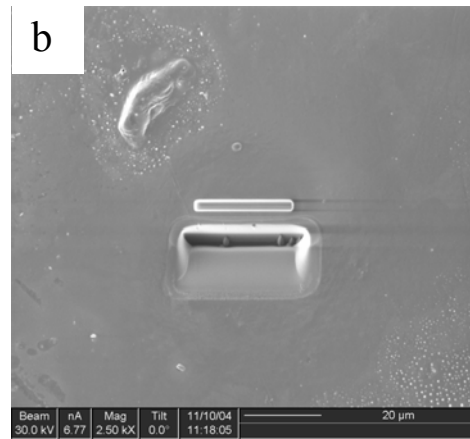
### 3.8.2 *In situ* Lift Out Technique

This technique is similar to the *ex situ* process except for that the sample is lifted out inside the FIB chamber with the help of an omni probe needle. Similarly, in this technique the sample

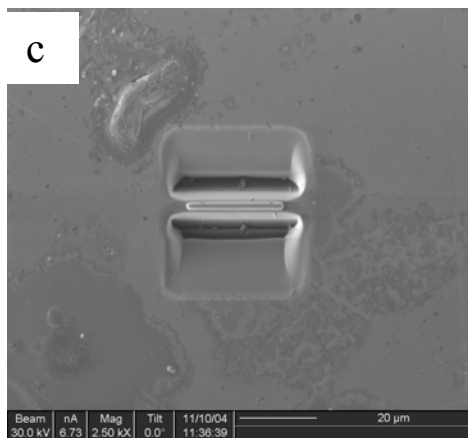
was loaded in the chamber and the height of the sample adjusted. A line of Pt layer was deposited and two trenches were milled on either side of the deposited Pt layer using the silicon file. The trenches were milled with higher currents (20000 pA) when away from the deposited platinum and were made with lower currents (7000 pA) close to the Pt layer. Following this, a bottom cut was made by tilting the specimen by 45°. After the bottom cut was made, the sample was rotated by -45° and the Pt needle and omni probe were introduced. The sample was lifted from the pit by attaching the sample to the omni probe, after depositing Pt to attach it to the omni probe. The omni probe and Pt needle were then taken out, and a half cut copper grid was introduced. A trench was milled on the copper grid into which the sample was placed. The Pt needle and the omni probe were introduced and the sample was placed on the copper grid. After placing the sample on the grid, the thinning of the sample was done to make it electron beam transparent. The advantage of this technique over the *ex situ* technique is that if the sample was found to be thick for electron beam transparency, it could be taken back into the FIB chamber and thinned again. Whereas in case of the *ex situ* technique, once the sample was cut out and put on the copper grid with carbon film, it could not be thinned further. Figure 11 outlines the *in situ* technique of preparing the TEM samples.



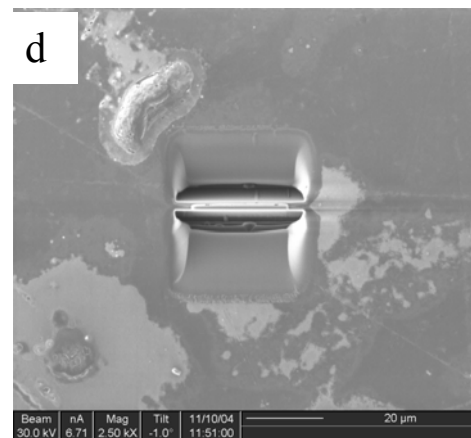
a. Pt deposited on the surface of the sample



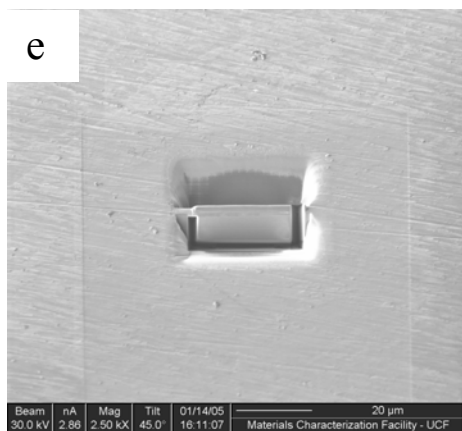
b. Trench in front of the deposited Pt



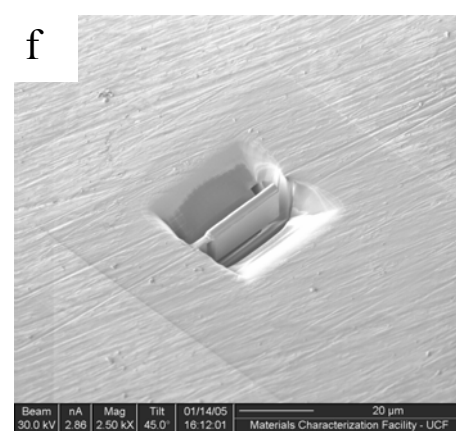
c. Trench on both sides of the deposited Pt



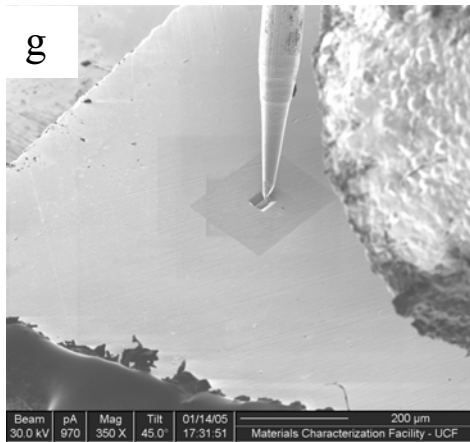
d. Thinning before the bottom cut



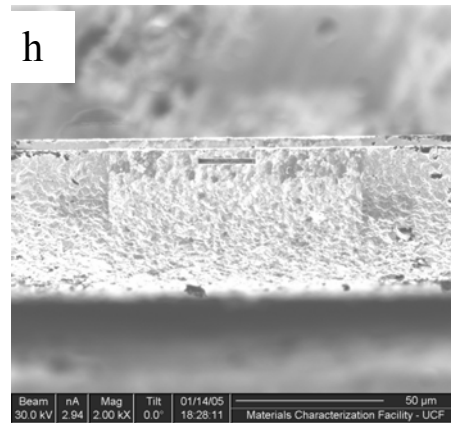
e. Tilting 45° for bottom cut



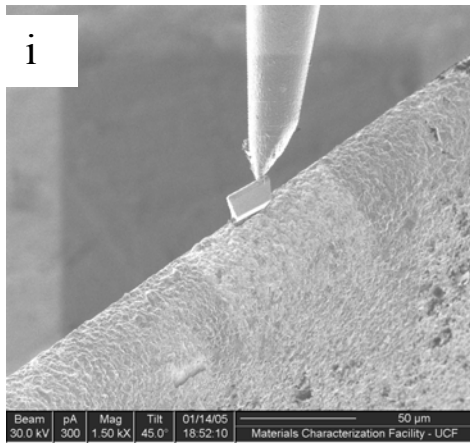
f. Rotated by -45°



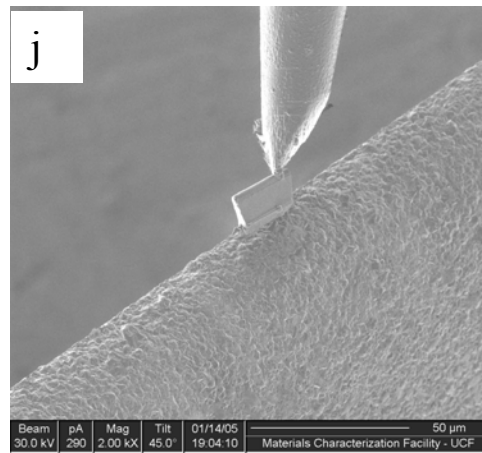
g. Lifting sample with the help of the omni probe



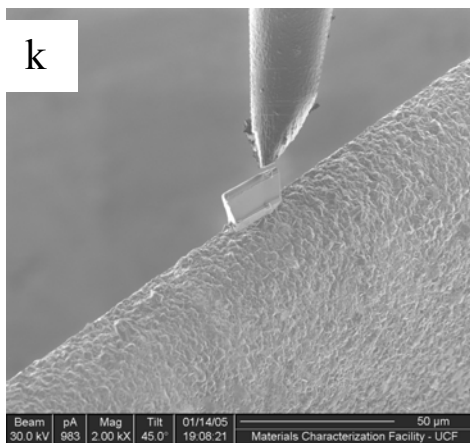
h. Trench milled on half cut Cu grid



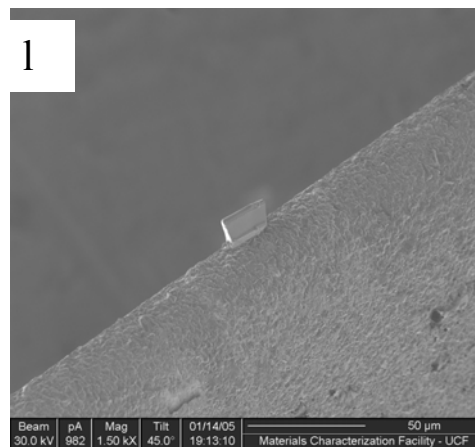
i. The sample about to be placed in the trench on the copper grid.



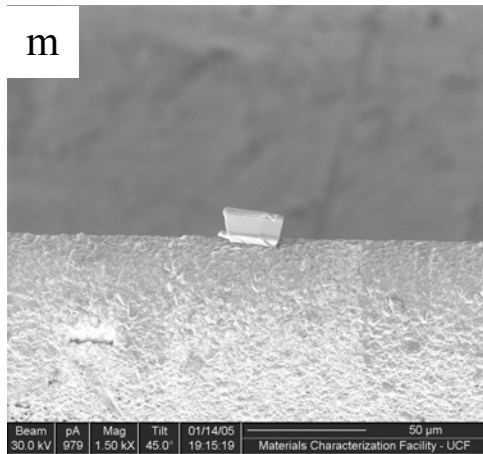
j. Pt deposited when the sample is in the trench.



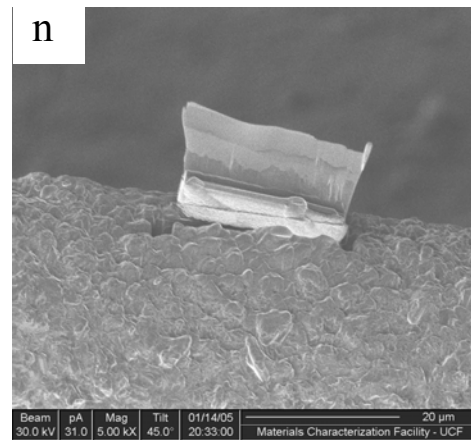
k. The omni probe cut from the sample



l. The sample placed on the grid



m. Half way through the thinning process



n. Final thinning

Figure 11: The FIB *in situ* technique used for TEM sample preparation

### **3.9 Electropolishing**

3 mm diameter discs were cut from the bulk specimen with the help of a low speed diamond saw into 0.1-0.3 mm thick plates. The discs were electrochemically thinned using a twin-jet electro polisher (Tenupol 2, Sturders, Denmark). The electrolyte used was 1: 3 (volume) nitric acid ( $\text{HNO}_3$ ) and methanol ( $\text{CH}_3\text{OH}$ ) at a voltage of 15 V. The flow rate was adjusted according to need. The samples were rinsed in distilled water after they are removed from the electrolyte.



### **3.10 Mechanical Polishing using a Tripod**

For preparing TEM sample using a tripod, a sample, cyano-acrylate based super glue, diamond lapping film, colloidal silica, a copper washer, wax and M-bond 610 adhesive are needed. Samples were cut to fit a tripod using a low speed diamond saw and were mounted using cyano-acrylate based super glue. They were polished using diamond paper and colloidal silica to form a wedge. This was achieved with one tripod on which the sample was placed, 1 mm lower than the other two pods. Once it was sufficiently thin, the samples were mounted on either titanium or copper washers, with M-bond 610 adhesive and heated for 15 minutes around 100°C to cure the adhesive.

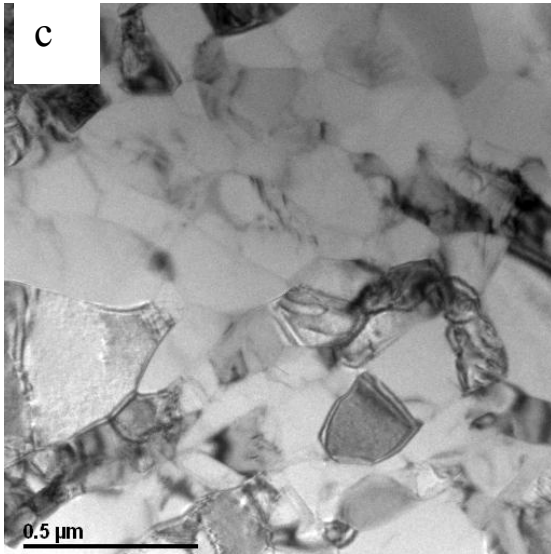
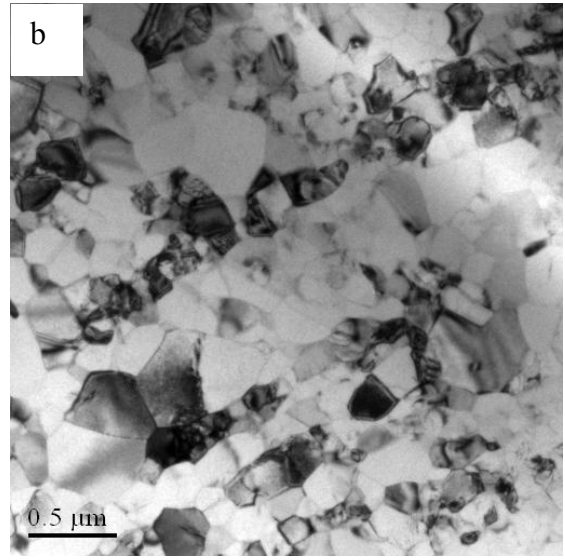
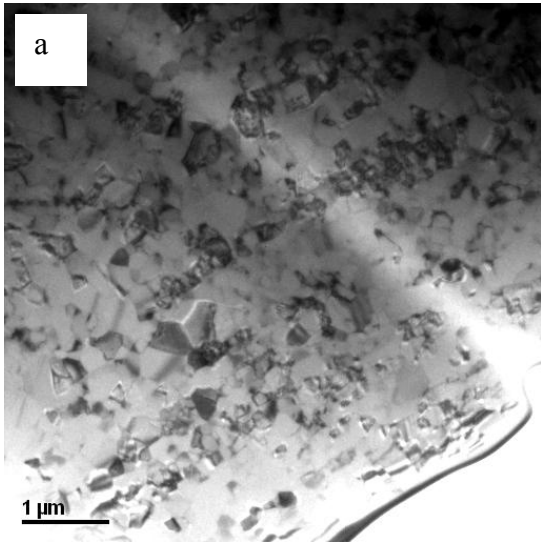
# CHAPTER FOUR: EFFECT OF PLASTIC DEFORMATION AND CYCLING

## 4.1 Undeformed Austenitic NiTi

### 4.1.1 Results

The samples were prepared by using the *ex situ* FIB technique as stated in Section 3.8.1. Figure 12(a)-(e) show the TEM images of NiTi\_A\_CD. Figure 13(a) shows an additional TEM image of NiTi\_A\_CD while Figure 13(b) shows the corresponding selected area diffraction pattern (SADP). The sample is in the [111] orientation with respect to the beam. Two grains overlap in the diffraction pattern in Figure 13(b), since there is no single spot in the diffraction pattern. Additionally, there are substantial bending contours seen in the sample.

The NiTi\_A\_HIP sample was prepared for TEM studies using both FIB and electropolishing methods. Figure 14(a) shows the FIB prepared sample, and the corresponding diffraction pattern is shown in Figure 14(b). The electropolished sample was prepared in the manner described in Section 3.9 where liquid nitrogen was poured into the electrolyte during electropolishing until the electrolyte had reached a temperature of approximately  $-40^{\circ}\text{C}$  as shown in Figure 15. Figure 15(a) shows large grains while Figure 15(b) shows the corresponding diffraction pattern for the beam orientation [110]. Figure 16 shows the grains in [111] orientation where the  $1/3$  reflections are seen clearly between the 110 diffraction spots.



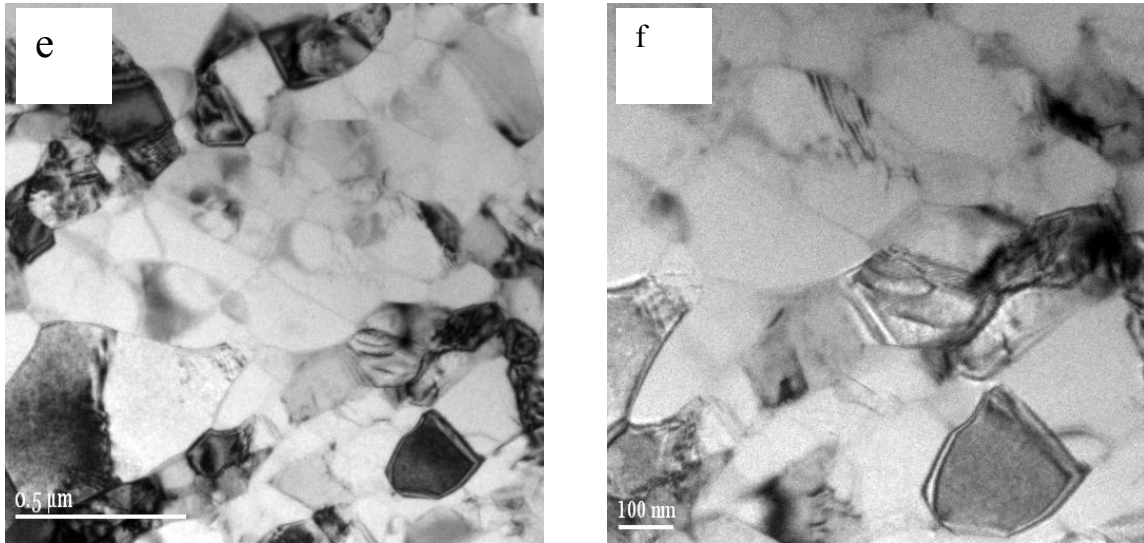


Figure 12: (a-f) TEM images of NiTi\_A\_CD

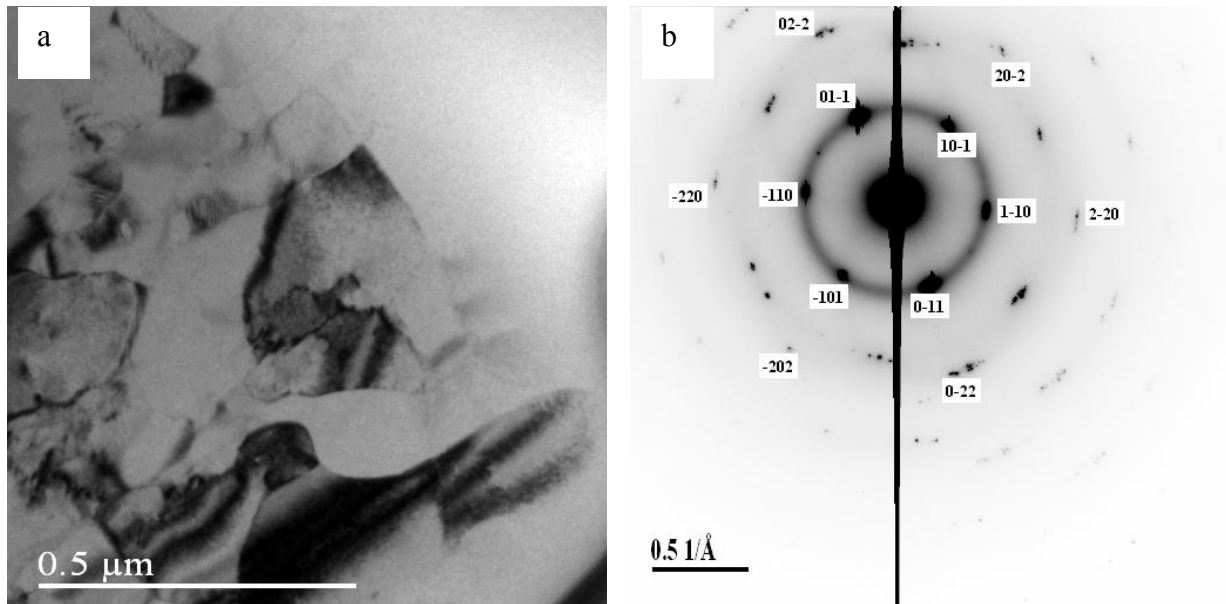


Figure 13: (a) TEM image of NiTi\_A\_CD and the corresponding SADP is shown in (b)

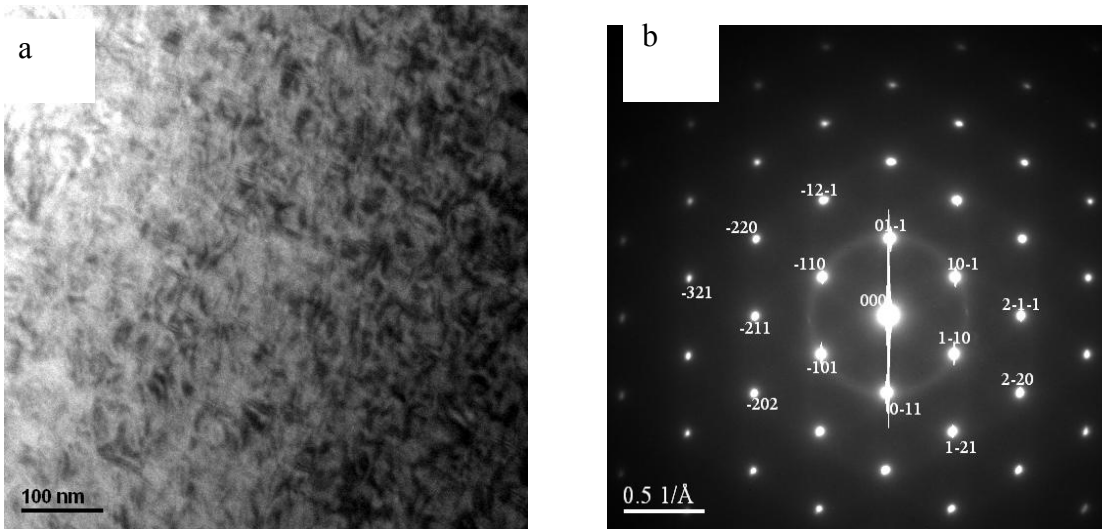


Figure 14: (a) TEM image of NiTi\_A\_HIP (prepared using FIB) and the corresponding SADP is shown in (b)

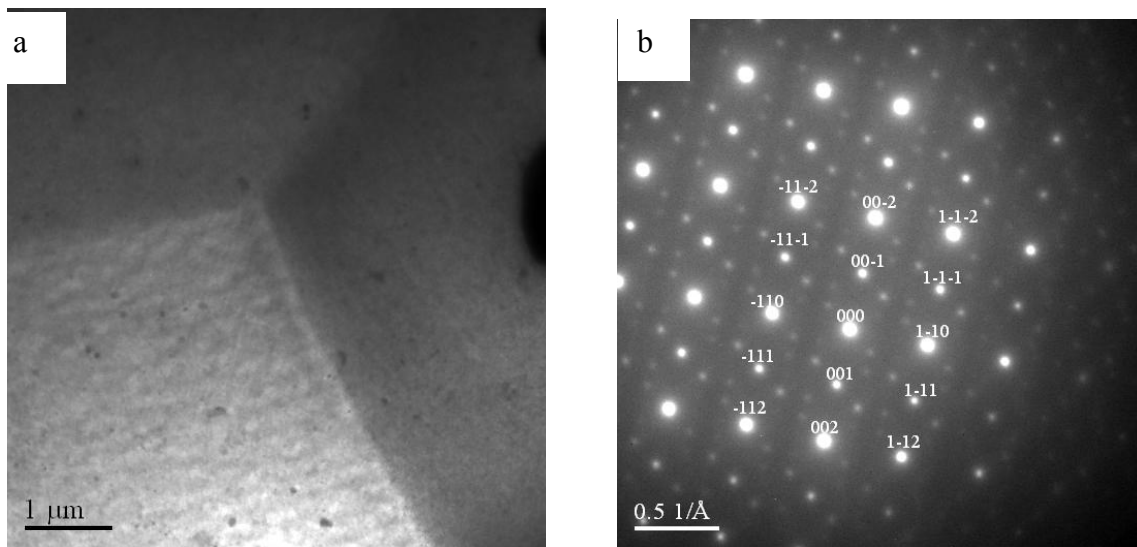


Figure 15: TEM image of NiTi\_A\_HIP (electropolished sample) and the corresponding SADP is shown in (b)

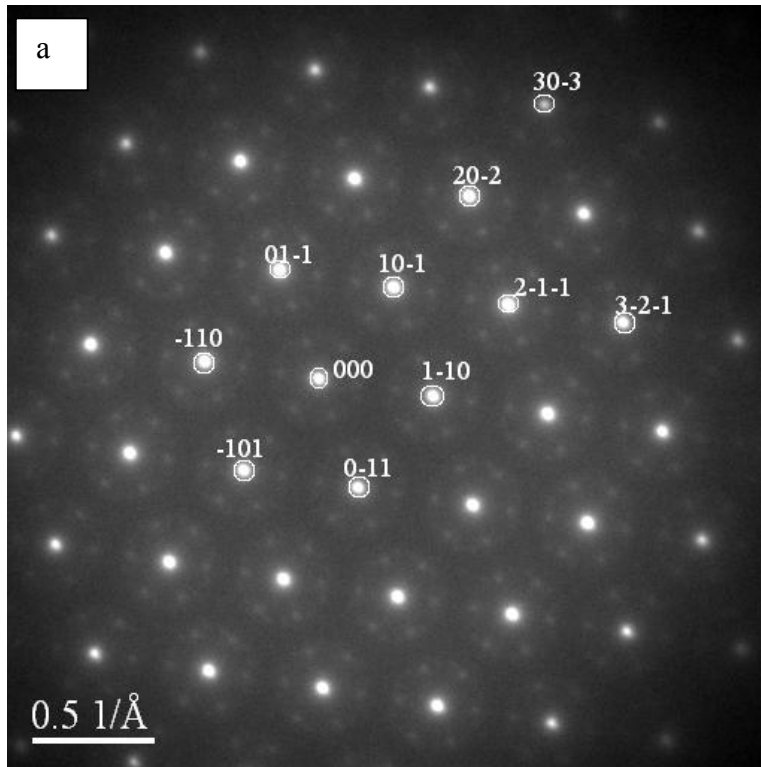


Figure 16: SADP of NiTi\_A\_HIP (electropolished sample)

#### 4.1.2 Discussion

The images of NiTi\_A\_CD in Figure 12 indicate that there is texture in the sample as seen from grains in the Bragg condition lining up (especially in Figure 12(a) and Figure 12(b)). As this sample was cold drawn it is expected to have texture. The diffraction pattern analysis in Figure 13 confirms that the sample is in the austenitic state, as expected for this starting composition.

The NiTi\_A\_HIP sample was processed in a way described in Section 3.2. From Vaidyanathan *et al.* [1999b] the average size of the grains was estimated to be 20  $\mu\text{m}$ . These large grains are very large in comparison to the grains seen in the NiTi\_A\_CD sample. These grains are randomly distributed in the sample. They are expected to be randomly distributed as

HIP was used for fabrication. The sample which was prepared by the FIB technique shows that only austenite is present in the sample as seen in Figure 14. On the other hand, the SADP of the electropolished sample in Figure 15(b) presents some extra super lattice reflections other than the reflections belonging to the austenite phase. From Figure 16, where the beam is in [111] orientation, it can be seen that the reflections occur at 1/3 positions from the  $\langle 110 \rangle$  spots

This phenomenon occurs with the formation of R-phase [Stroz 2003]. But the formation of the R-phase was seen to be strange in this sample as it was supposed to be an austenitic sample. The reasons for seeing the R-phase in this sample can be due to the presence of some Ni-rich precipitates or due to the liquid nitrogen cooling used in the electrolyte, which could have transformed the material and induced R-phase in the material. It could also be from chemical reactions with the electrolyte, for e.g., Ti can oxidize making the sample more Ni-rich and thus stabilizing the R-phase.

## **4.2 Deformed Austenitic NiTi**

### **4.2.1 Results**

The NiTi\_A\_8% sample was prepared as described in Section 3.3. The sample for TEM was prepared by using the *ex situ* FIB technique. For HRTEM images, the sample was prepared by electropolishing. Figure 17(a) presents the martensite lenticular structure interwoven in the austenite matrix. Figure 17(b) is the SADP of the area shown in Figure 17(a). Figure 18 also shows the lenticular structure in the sample. Figure 18(b) is a SADP of the area in Figure 18(a). Figure 19 shows the HRTEM/FFT images of the NiTi lattice with dislocations. Figure 20

presents the lenticular shaped twins. A lenticular structure of martensite interwoven with the austenite phase is visible in Figure 18 and Figure 18(b) gives the corresponding SADP. It tells us that the sample has a interwoven austenite martensite structure. The lenticular structures appear to be oriented in a particular direction (Figure 22). Figure 23 shows the Burgers vector around the edge component of the dislocation line. Figure 24 gives a line profile of the top and the bottom parts of the lattice lines seen in Figure 23. These images indicate the presence of dislocations at the interface of the martensite needles

The NiTi\_A\_14% sample was prepared for TEM observations by the *ex situ* FIB technique. It was processed as described in Section 3.4. Figure 25 shows the distribution of the dislocations in the grains in the 14% strained sample. Figure 25 (a) and (c) are the bright field micrographs of the NiTi\_A\_14% sample while Figure 25(b) is the dark field image of the NiTi\_A\_14% sample. Figure 26 shows a micrograph of an austenite grain and the corresponding SADP. The beam orientation was [111]. The martensite lenticular structures in Figure 27 are interwoven in the austenite matrix. The SADP of Figure 27(b) shows evidence of the presence of martensite.



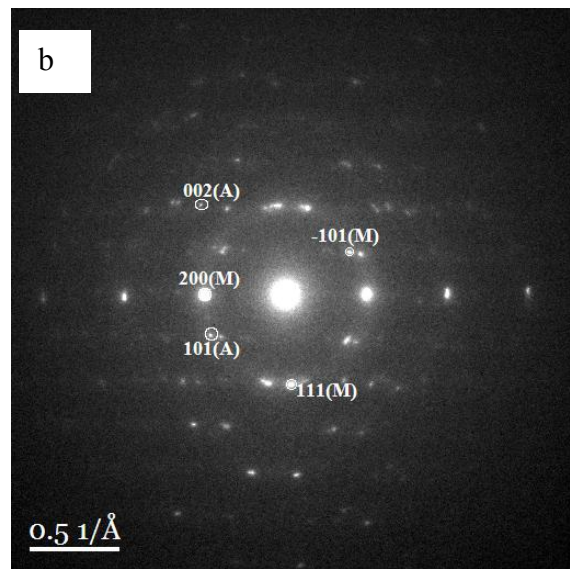
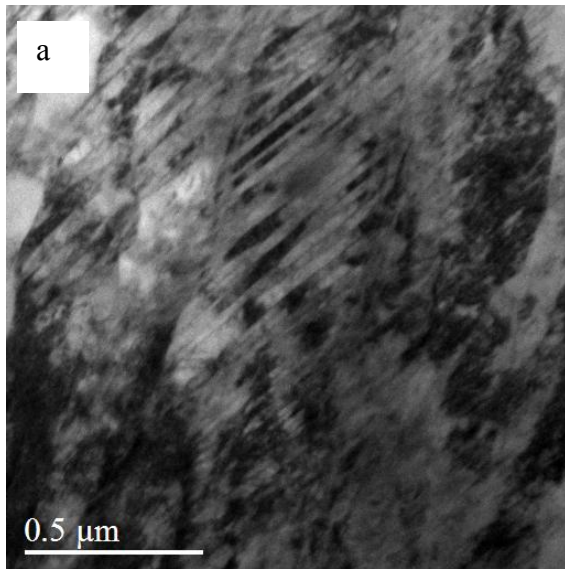


Figure 17: (a) TEM image of NiTi\_A\_8% and the corresponding SADP is shown in (b)

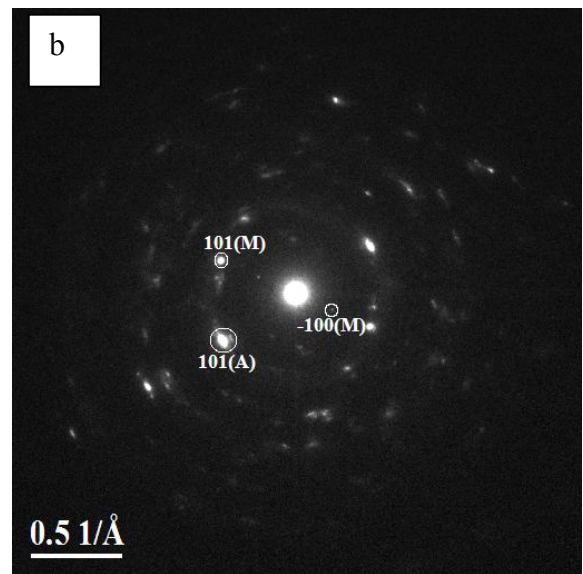
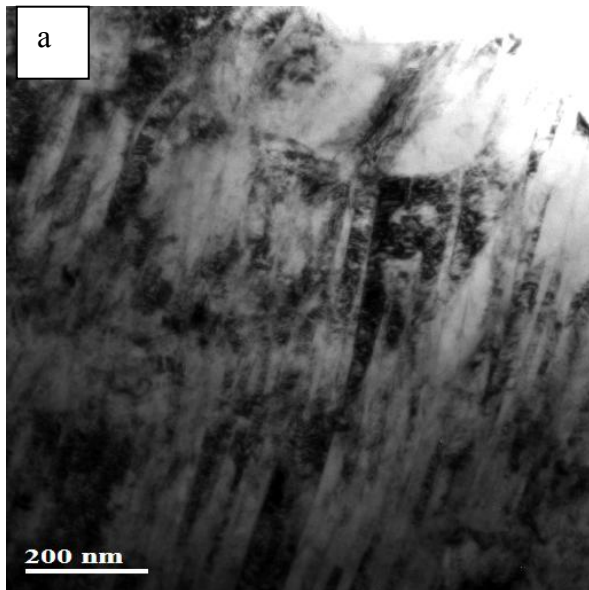


Figure 18: (a) TEM image of NiTi\_A\_8% and the corresponding SADP is shown in (b)

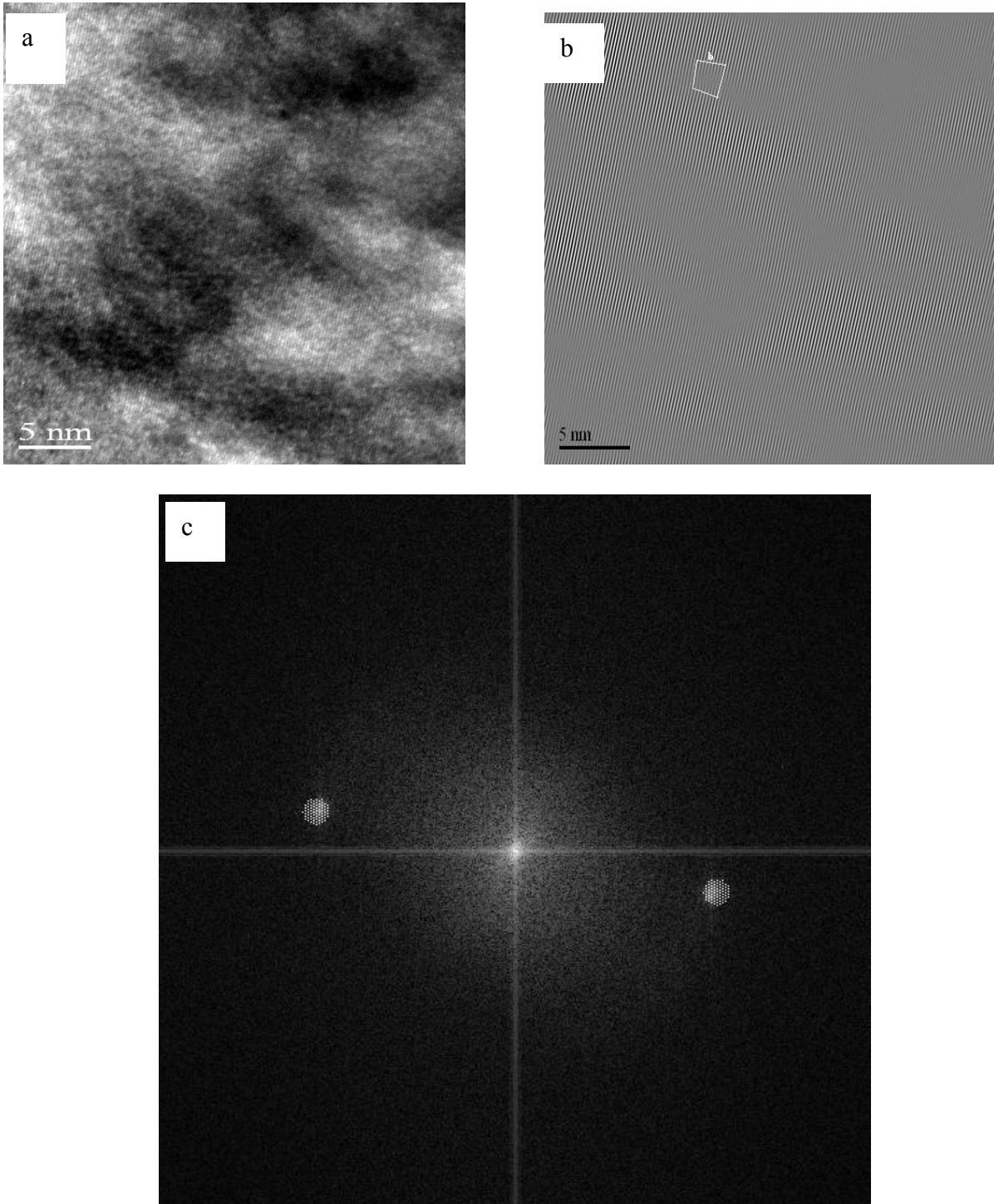


Figure 19: (a) HRTEM image of the lattice in NiTi\_A\_8% (b) Fourier filtered HRTEM image of NiTi\_A\_8%. (c) Reduced fourier filter image of 19(a) showing the reflections

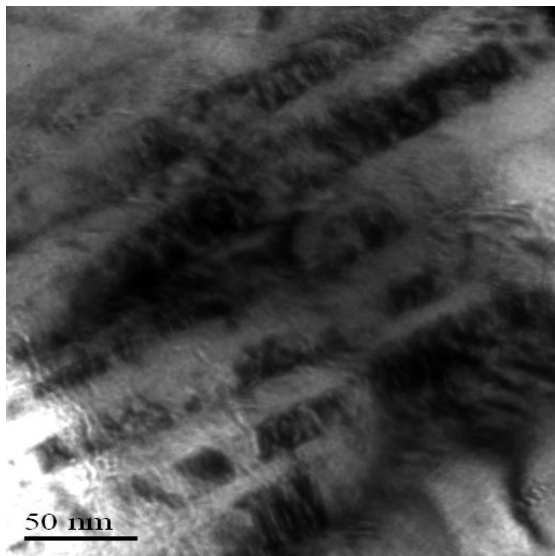


Figure 20: TEM image of NiTi\_A\_8%

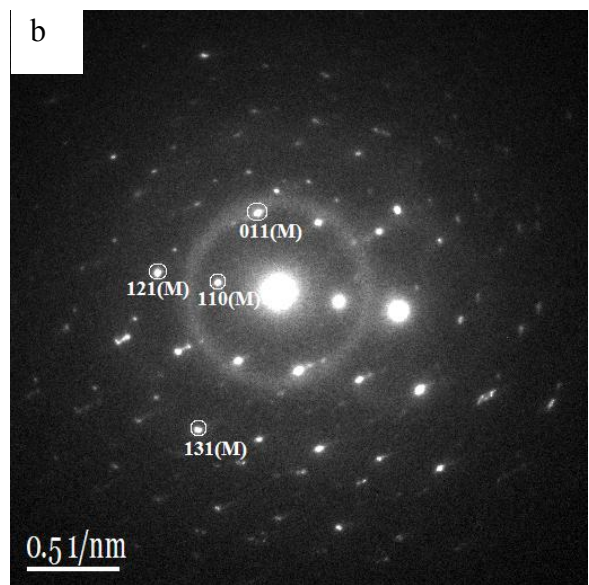
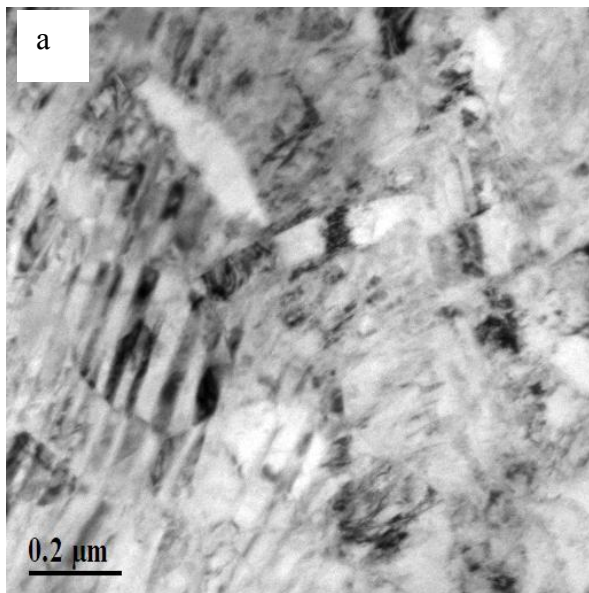


Figure 21: (a) TEM image of NiTi\_A\_8% and the corresponding SADP is shown in (b).

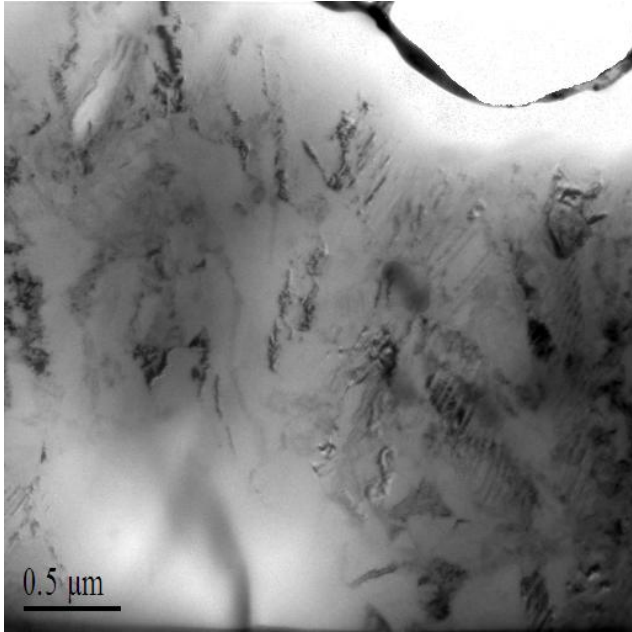
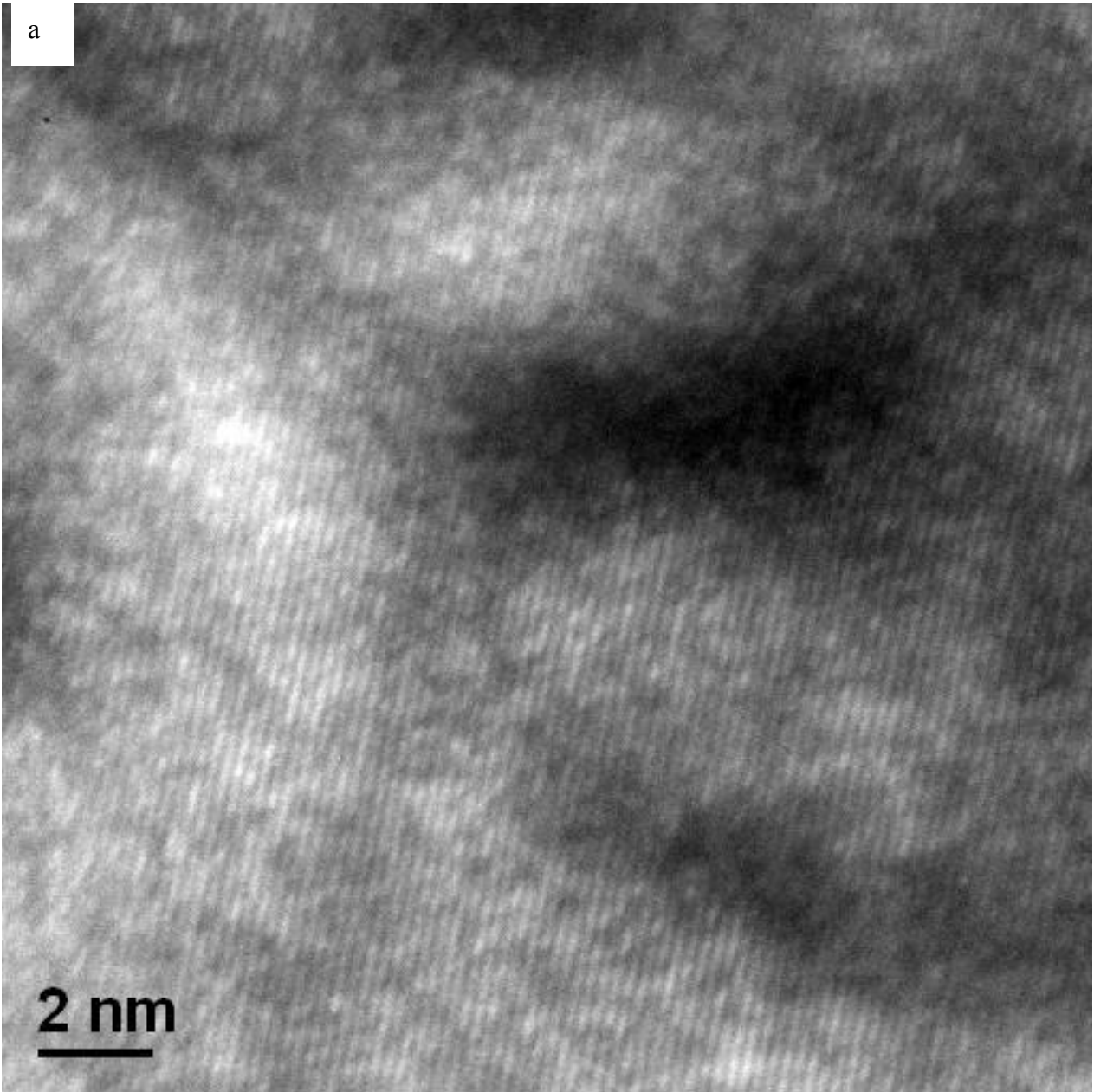


Figure 22: TEM image of NiTi\_A\_8%



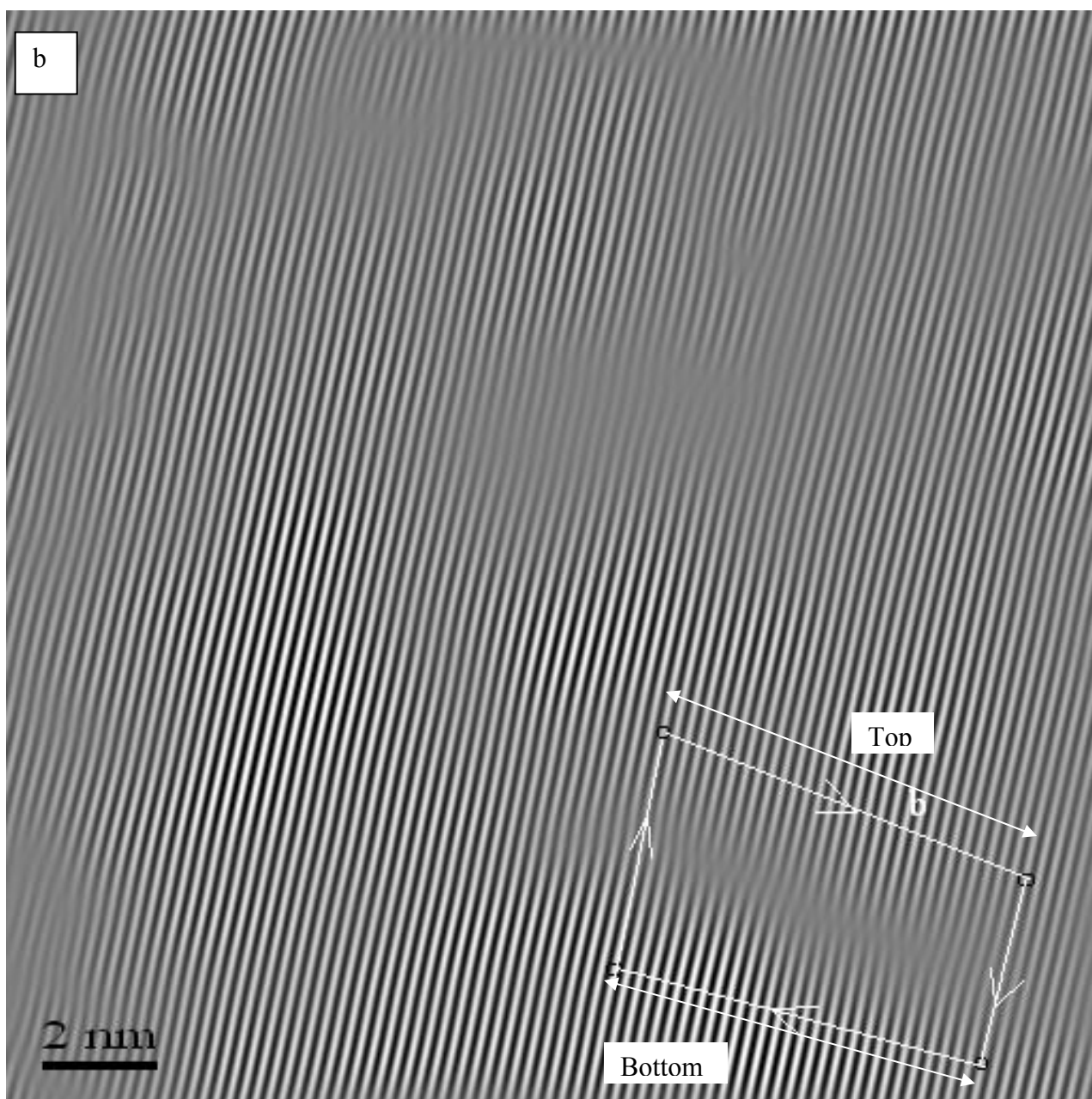


Figure 23: (a) HRTEM image of NiTi\_A\_8% (b) Fourier filtered HRTEM image of NiTi\_A\_8%

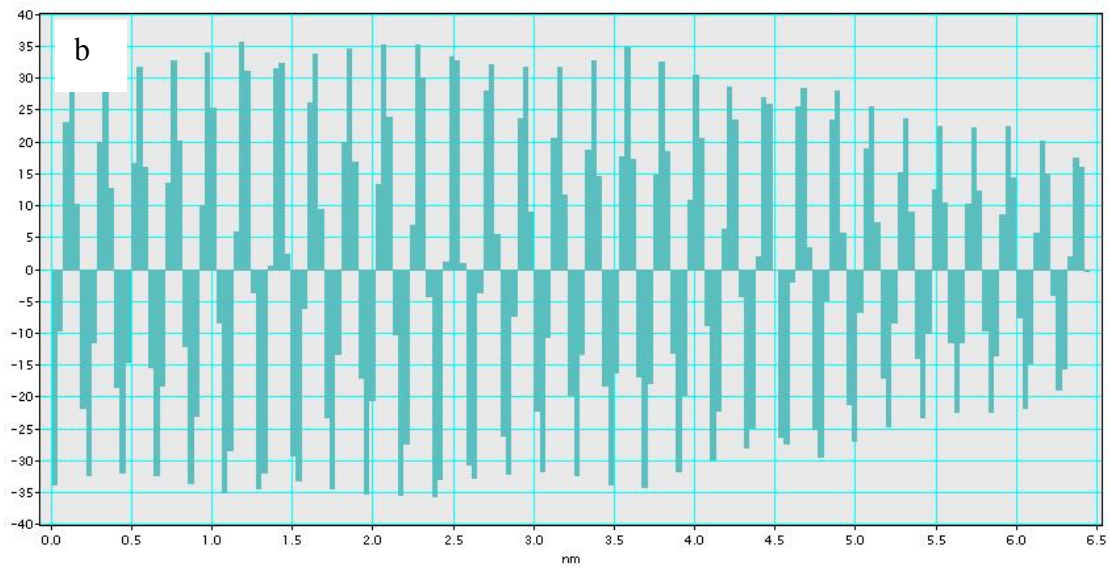
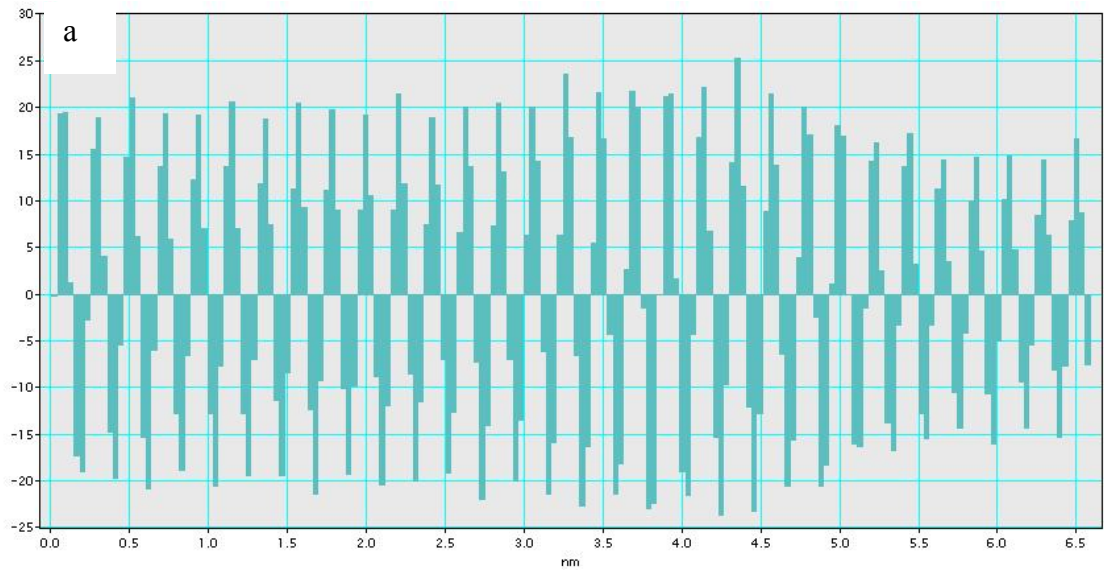


Figure 24: Profile around the dislocation lines shown in Figure 24; (a) is the top profile while (b) is the bottom profile of the lattice of NiTi\_A\_8%

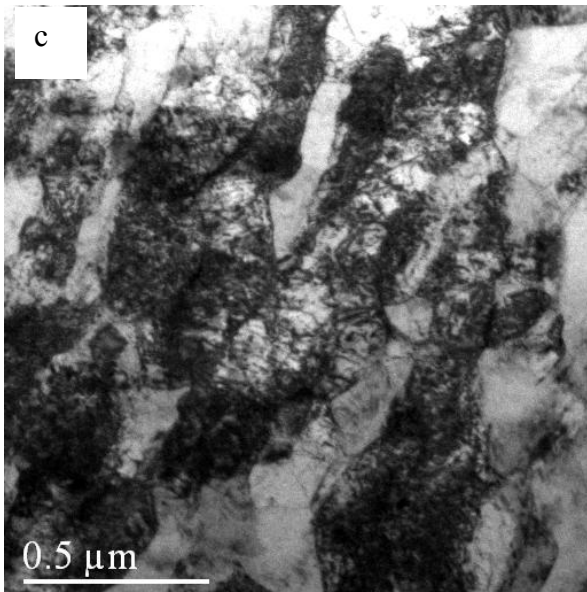
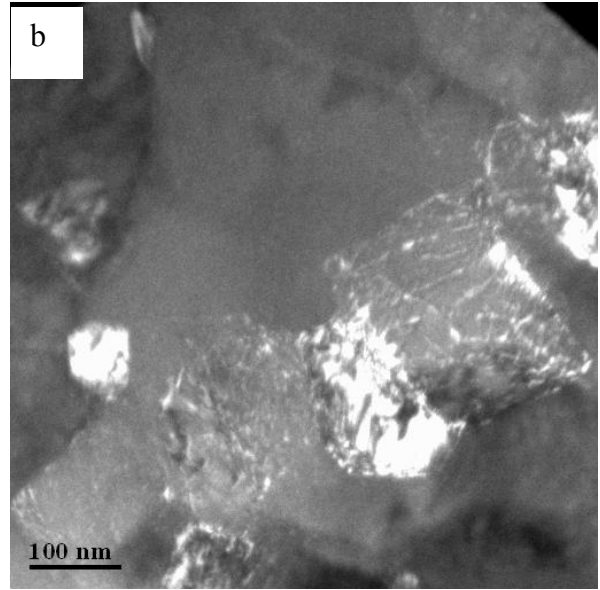
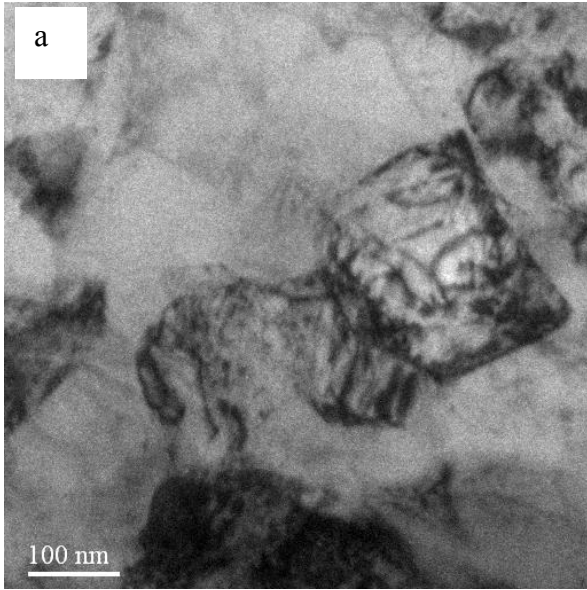


Figure 25: TEM images of NiTi\_A\_14%



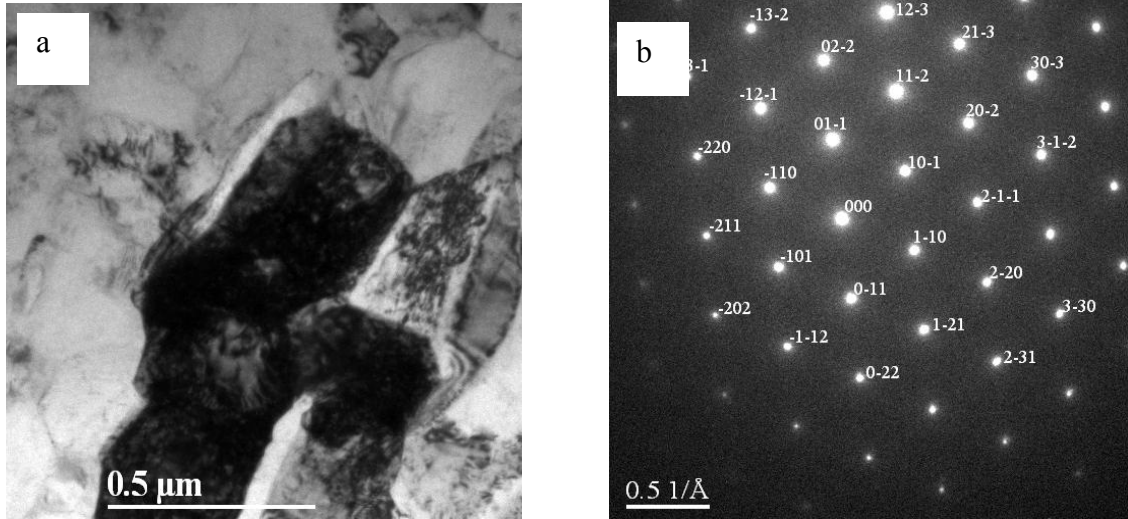


Figure 26: (a) TEM image of NiTi\_A\_14% and the corresponding SADP is shown in (b)

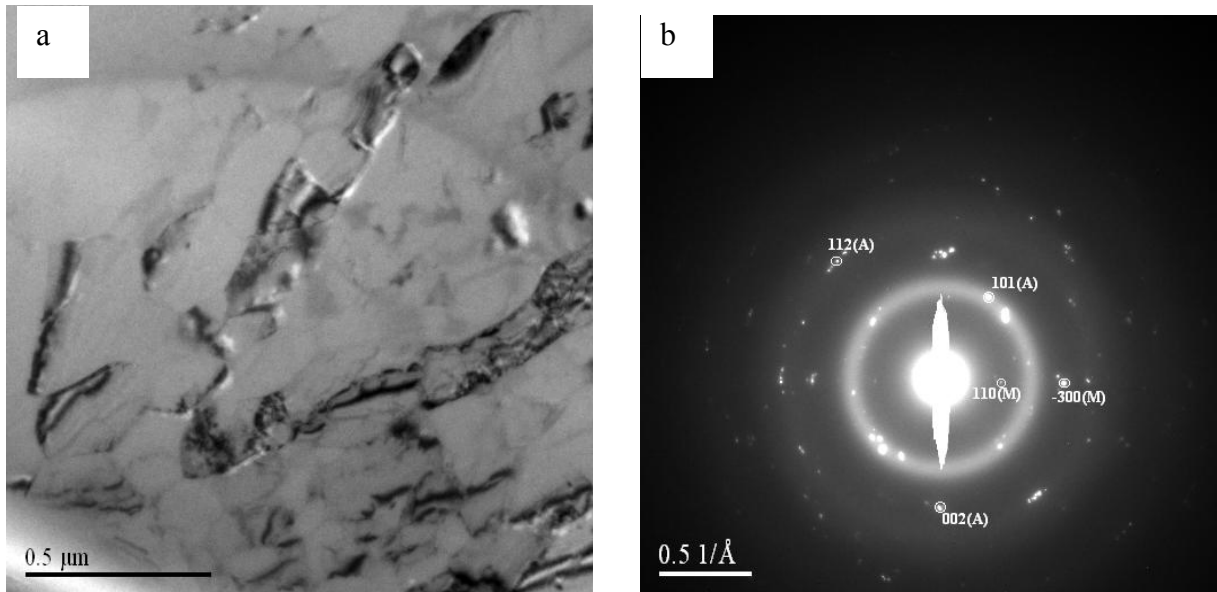


Figure 27: (a) TEM image of NiTi\_A\_14% and the corresponding SADP is shown in (b)

## 4.2.2 Discussion

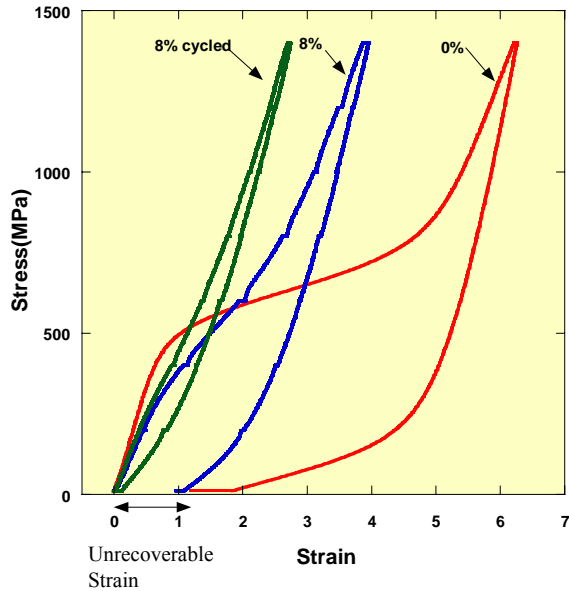


Figure 28: Stress-strain response of the undeformed (NiTi\_A\_CD), 8% plastically strained and 8% plastically strained and 15 times cycled (NiTi\_A\_8%) samples

The stress-strain curves in Figure 28 show that the curve of undeformed NiTi (NiTi\_A\_CD) exhibits a large hysteresis and has some unrecoverable strain associated with it. The 8% plastically strained sample also has unrecoverable strain but a smaller hysteresis. The stress strain curve of the 8% plastically strained sample that undergoes cycling (NiTi\_A\_8%) does not exhibit any unrecoverable strain and additionally the hysteresis collapses in comparison to the 8% strained sample.

In the present investigation we are trying to study the effect of cycling on the 8% plastically strained sample that has under gone 15 load-unload cycles. The material is in the austenite phase

and with the application of load, stress induced martensite is formed in the material, i.e., it exhibits superelasticity. In the austenite state the material exists in the cubic form. It is known that the martensite has 24 variants and it can change from the cubic structure to the monoclinic structure in 24 different crystallographic ways during the phase transformation. These 24 different ways are the different variants. Cycling is expected to result in the stress- induced growth of the most favorably oriented martensite variants, stress induced reorientation of martensite and also stress induced twin boundary migration within the martensite variants.

Even though the Ni-rich composition implies that the sample exists in the austenite state, the 8% plastic deformation results in the stabilization of martensite in the unloaded state. This is evident in the TEM images presented earlier. Figure 17 and Figure 18 shows interwoven austenite and martensite together, as observed in the SADP. The martensite needles tend to orient themselves in one particular orientation, which is evident in Figure 22. This implies that the martensite variants tend to reorient themselves in one of the favorable martensitic variants, either through variant coalescence or through variant reorientation. Thus, these variants reorient or grow at the expense of less-favorably oriented ones because of the cycling. In addition to these aforementioned observations dislocations were seen at the interfaces between adjoining martensitic needles. These dislocations are evident when observed in the HRTEM images in Figure 23 where the Burgers vector is identified. Line profiles of the image in Figure 23 are shown in Figure 24 where 31 lattice lines can be counted in the top section while only 30 lattice lines can be counted in the bottom section of the burgers circuit. This is indicative of an edge dislocation at that interface.

It is interesting to consider the role of these dislocations. Clearly, the applied plastic strain results in the generation of these dislocations. Even though there is no doubt that these

dislocations exist (from the fact that the sample has 8% plastic strain and from the aforementioned TEM images), the 15 times cycled NiTi\_A\_8% sample shows no unrecoverable strain during loading and unloading. This implies that the dislocations are either (i) in a stable or locked configuration or (ii) are being shielded from the external applied stress. On application of stress, the austenite transforms to martensite and, in doing so, accommodates the stress and strain mismatch through variant selection, reorientation and coalescence. The stabilized martensite (i.e., the martensite that exists in the unloaded state) also can accommodate the mismatch through variant reorientation and coalescence. It appears that both of these mechanisms, i.e., accommodation through transforming the austenite or accommodation through stabilized martensite, are viable. The exact reason for the dislocation existing at the interface of the martensite needles is not clear. It could serve to accommodate the mismatch between variants of stabilized martensite or it could just be that the dislocations pin the martensite needles and hence appear at the interfaces. It is also possible that the martensite is stabilized around the dislocations due to the stress field resulting from the dislocations.

To separate the effect of cycling from the effect of only plastic deformation, the 14% plastically strained or NiTi\_A\_14% sample was studied. Qualitative examination suggests that there are smaller quantities of martensite in the NiTi\_A\_14% sample than in the NiTi\_A\_8% sample. Furthermore, while an interwoven austenite and martensite structure was identified (e.g., Figure 27), dislocations were found in the austenite grains (e.g., Figure 25 and Figure 26) rather than at the interfaces. Comparing results between NiTi\_A\_8% and NiTi\_A\_14% suggests that the load-unload cycling results in a stress field due to the dislocations stabilizing the additional martensite. This martensite serves to accommodate the stress and strain mismatch between the

dislocations and the transforming material resulting in reduced unrecoverable strain. This is seen in the macroscopic stress-strain curve.

### **4.3 Martensitic NiTi**

#### **4.3.1 Results**

The NiTi\_M\_0 sample was prepared with the help of the *ex situ* FIB technique for observation under the TEM. The wire was dipped in liquid nitrogen before preparing the sample by FIB to ensure that the sample was in the fully martensite state. Figure 29 shows the NiTi\_M\_0 sample wire with martensite variants distributed at a fine scale. The corresponding SADP in Figure 30 confirms a fully martensitic sample.

The NiTi\_M\_1214 sample for TEM was also prepared by the *ex situ* FIB technique. The wire was dipped in liquid nitrogen before preparing the sample by FIB to ensure that the sample was in the fully martensite state. Figure 31 is the TEM image of NiTi\_M\_1214 that shows larger martensite variants. Figure 32 is the corresponding SADP.

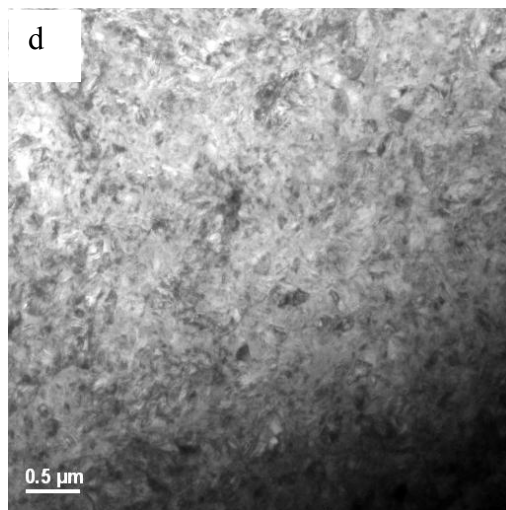
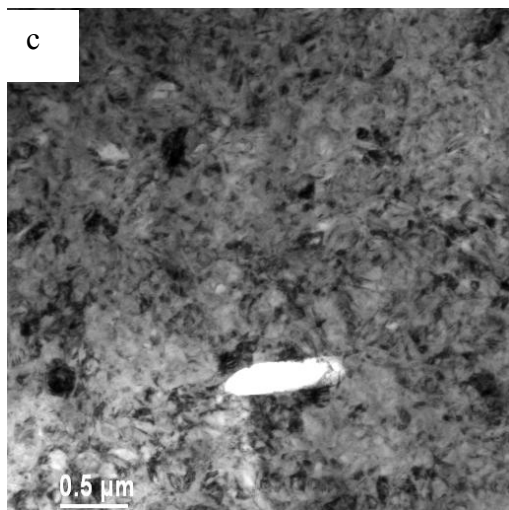
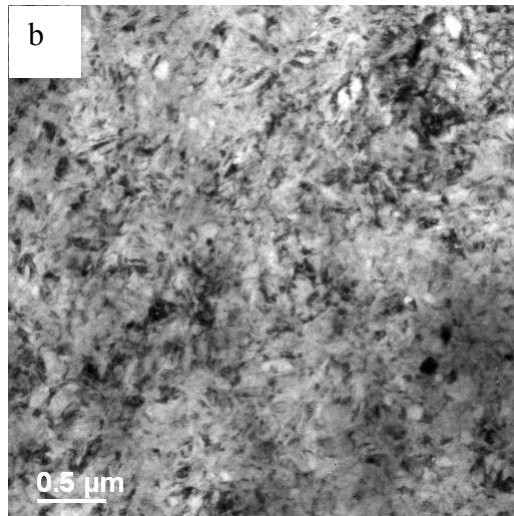
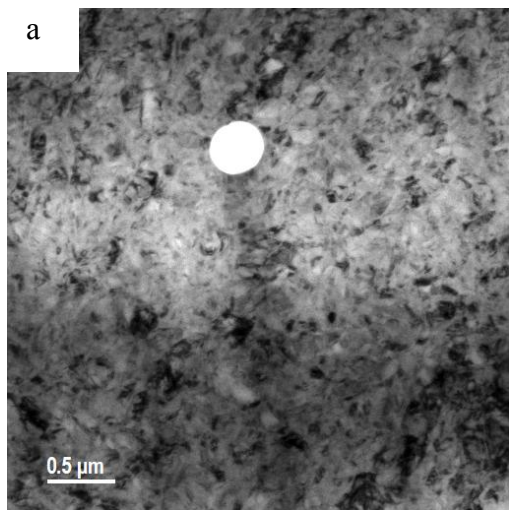


Figure 29: TEM images of NiTi\_M\_0

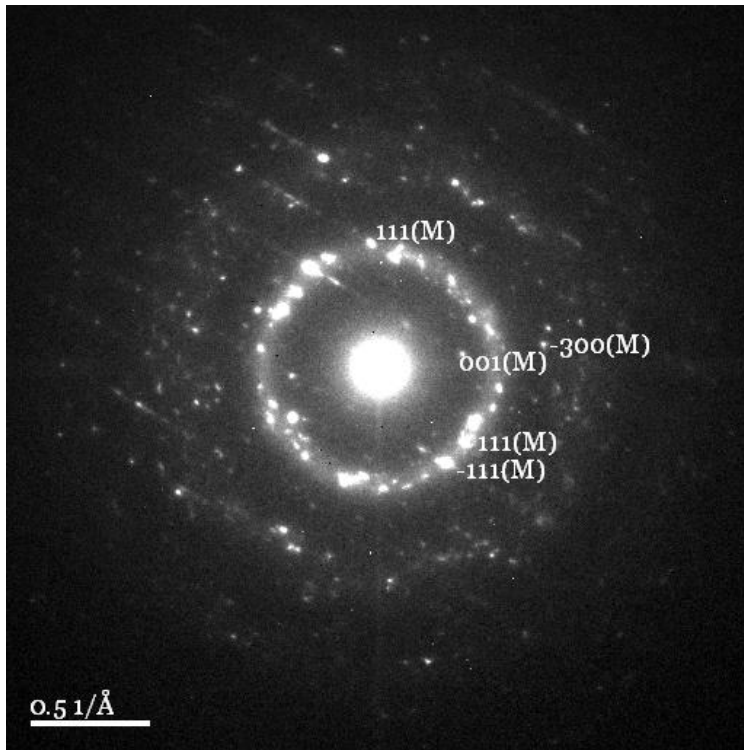


Figure 30: SADP corresponding to Figure 30(a)

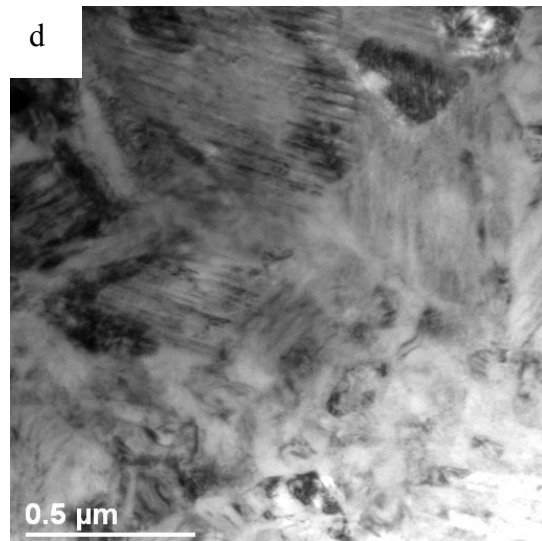
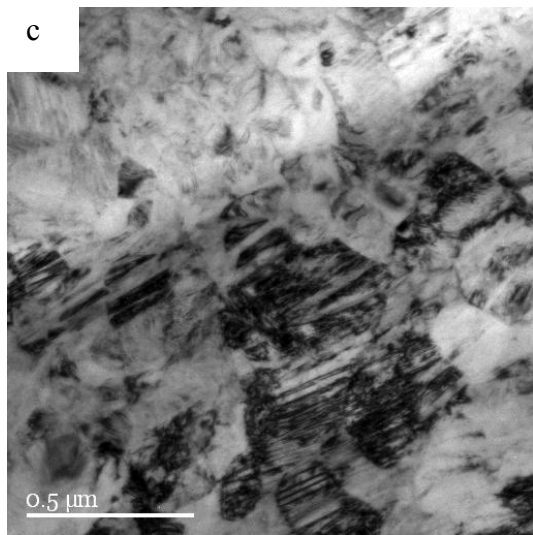
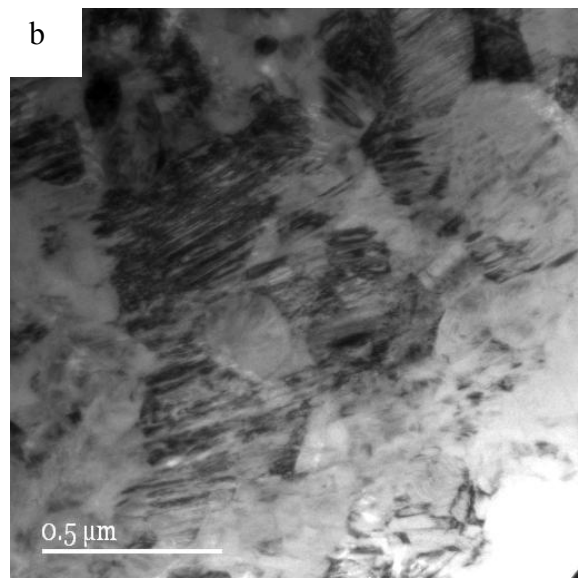
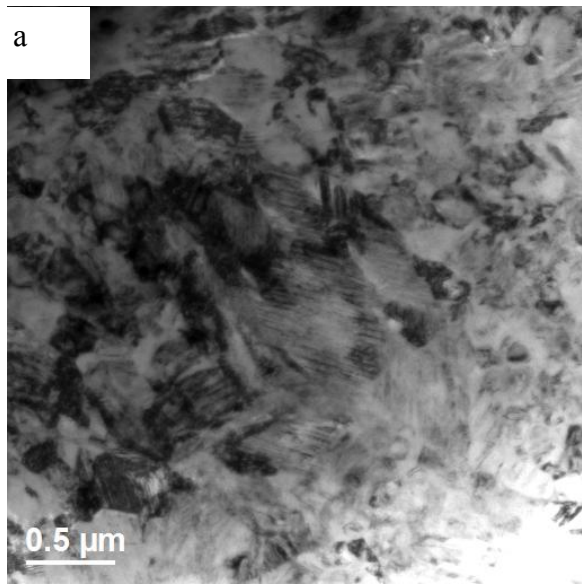


Figure 31: TEM images of NiTi\_M\_1214



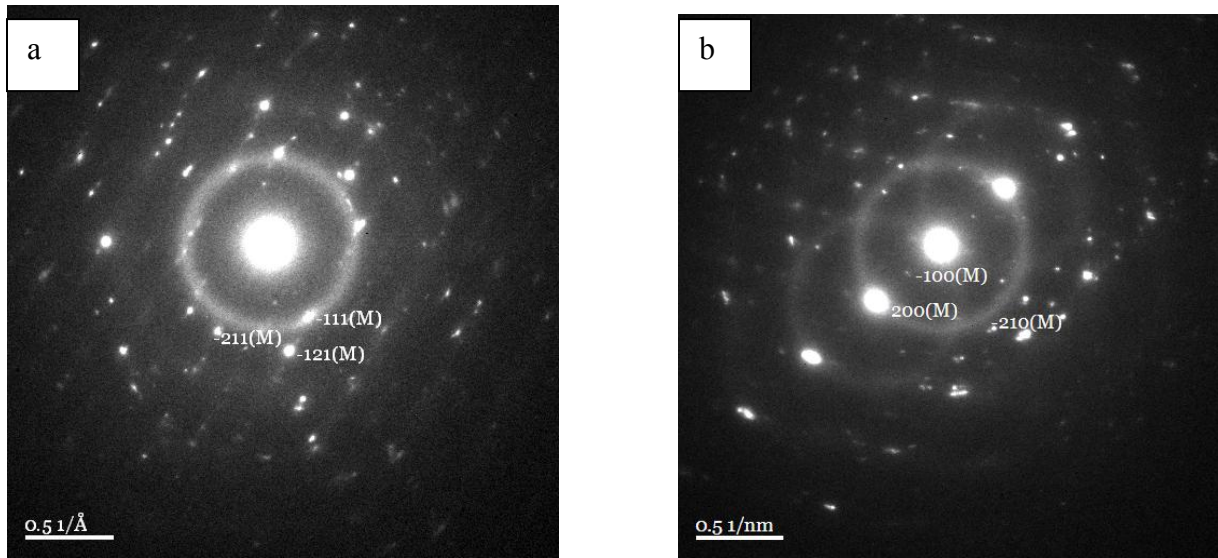


Figure 32: SADP corresponding to Figure 31(a) and Figure 31(b)

#### 4.3.2 Discussion

NiTi shape memory elements for actuator applications generally require the setting of a shape for the NiTi element. Shape setting of the NiTi element is accomplished by constraining it in a fixture of desired shape and applying an appropriate heat treatment. The heat treatment used for the NiTi element investigated, a wire in this case, is discussed in Section 3.5. The wire was dipped in liquid nitrogen to ensure that the sample was in the martensite state.

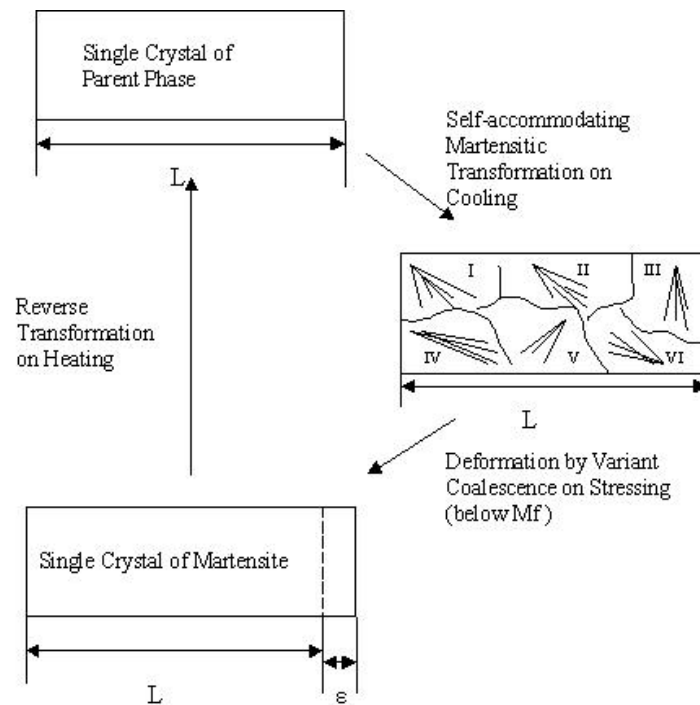


Figure 33: Schematic illustration of the shape memory effect in a single crystal

Figure 33 explains the phenomenon associated with the shape memory mechanism whereby cooling the sample from the parent austenite phase results in martensite forming in a self accommodating process. Subsequent deformation of that martensite results in the coalescence of the different variants because of which one of the favorable variant grows at the expense of the other variants. In Figure 29, small grain like structures corresponding to the different variants of the martensite are seen. These variants are mostly randomly arranged and are very fine in scale. Martensite needle like structures are not seen in the images. The diffraction pattern in Figure 30 gives evidence of the presence of martensite in the sample.

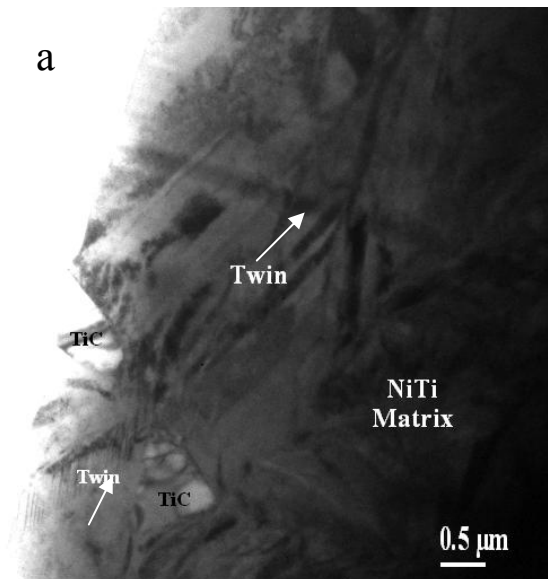
Figure 31 shows the effect of cycling in the sample after applying 1214 heat-cool cycles while loading. This simulates a NiTi element in cyclic actuator applications. Clearly twins and

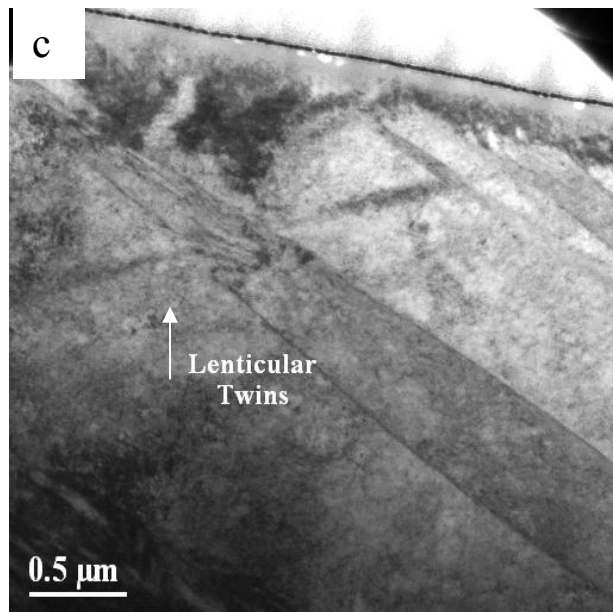
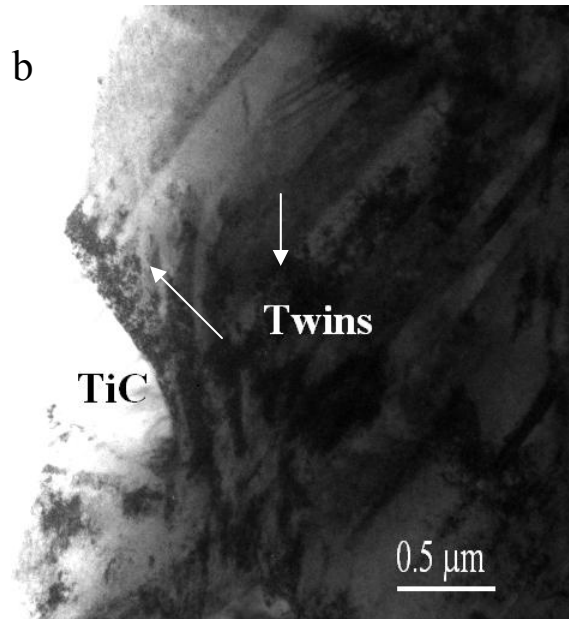
martensite lenticular structures are observed in the images. Again, the presence of martensite is confirmed by the SADP in Figure 32. It can also be observed from these images that the grains tend to orient themselves in one particular orientation. The aforementioned effects are a result of the internal stresses induced by the cycling. These stresses are biasing the formation of martensite during cooling through a combination of one or more of these processes: (i) variant selection; (ii) variant reorientation; and (iii) variant coalescence.

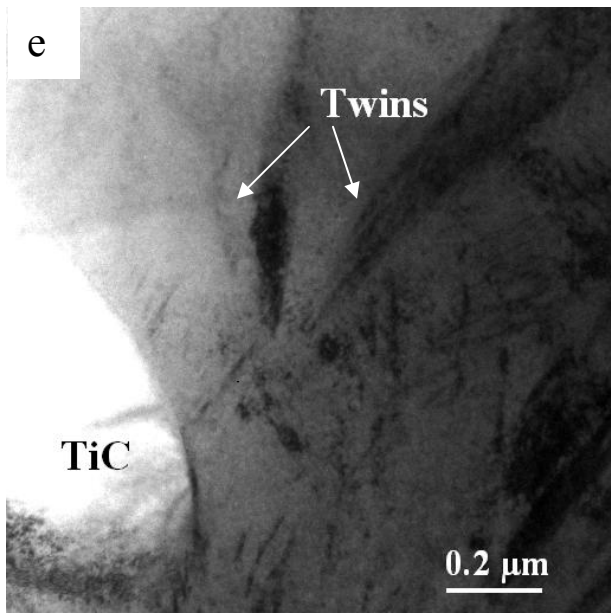
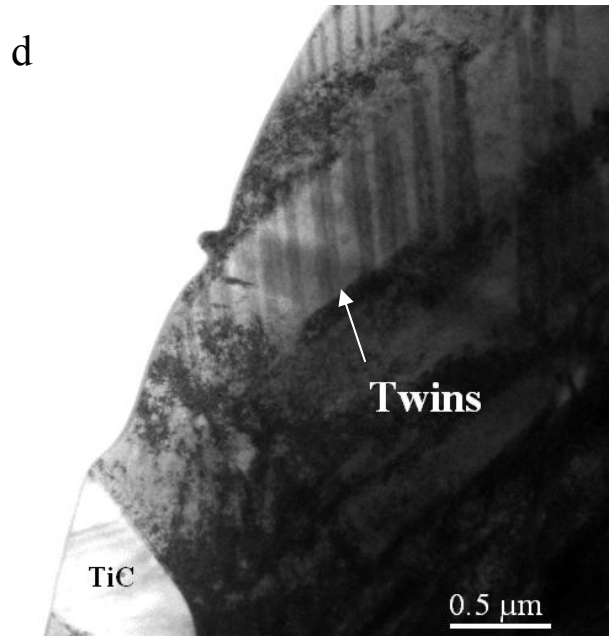
## CHAPTER FIVE: NiTi-TiC

### 5.1 Results

NiTi<sub>10</sub>TiC<sub>M</sub> samples for TEM were prepared by the *ex situ* FIB technique. The material was processed as described in Section 3.6. The sample was heated to 100 °C and then cooled to room temperature to ensure that it was in a fully martensitic state. Figure 34 shows TiC particles in the NiTi matrix. Lenticular twins are found a distance away from the matrix-TiC interface.







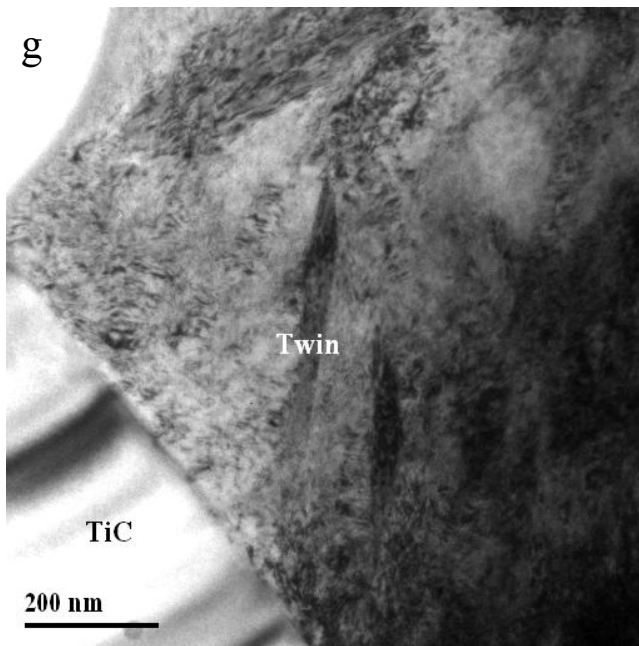
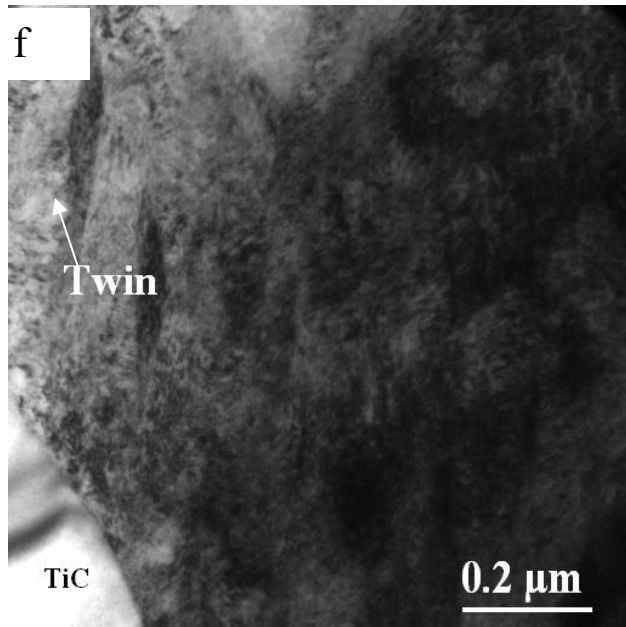


Figure 34: TEM images of NiTi<sub>10</sub>TiC<sub>M</sub>.

## **5.2 Discussion**

Microprobe and microscopy analyses was conducted by Vaidyanathan [Vaidyanathan 1998] on NiTi-10TiC to conclude that the TiC particles behave as an inert reinforcement. The micrograph in Figure 34 shows the presence of twins in the material. NiTi in martensitic form is expected to possess twins when cooled from the austenite state. However, in the case of the composite, additional stresses due to the coefficient of thermal expansion mismatch between the matrix and the inclusion can further enhance twinning in NiTi. To assess the magnitude of these stresses, is Eshelby equivalent homogeneous inclusion method was used and is described in the following.

### **5.2.1 Eshelby Equivalent Inclusion Method**

Internal stresses are common in almost any material, which is mechanically inhomogeneous. For a cubic polycrystalline metal, which is loaded externally, differently oriented crystallites will be stressed to different extents, but these differences are quite small. For a composite, consisting of two distinct constituents with different stiffnesses, these disparities in stress are generally found to be much larger. Internal stresses arise as a result of some kind of misfit between the shapes of the constituents (matrix and reinforcement, i.e., fiber, whisker or particle). Such a misfit could arise from a temperature change, but a closely related situation is created during mechanical loading-when a stiff inclusion tends to deform less than the surrounding matrix. Analysis of the stresses required to mate up the inclusion and matrix across the interface allows the prediction of properties such as thermal expansivity and stiffness. For a



spherical inclusion case of an ellipsoid, an analytical technique set on the pioneering work of 1950s by J.D.Eshelby can be employed [Clyne & Withers 1993].

The elastic strain field is very complicated, both inside and outside the constrained transformed region, and for this reason an analytic solution is not usually possible. If the transformed region is ellipsoidal in shape and the shape change is a uniform one (i.e., ellipsoidal to ellipsoidal), however, the mathematics become tractable as the stress and strain within the enclosed phase are uniform under these conditions [Clyne & Withers 1993].

### 5.2.2 Determination of Internal Mismatch Stresses

Following Dunand *et al.* [1996], we apply the equivalent homogeneous inclusion model developed by Eshelby, who considered a random distribution of ellipsoidal inclusions in an isotropic matrix, both phases exhibiting different elastic constants. We use the solutions for nondilute systems.

Thermal and transformation mismatch stresses:

$E_{100} = 125 \text{ GPa}$       elastic modulus of matrix

$\nu = 0.35$               Poisson's ratio of matrix

$\bar{\mu} = 28.199 \text{ GPa}$       shear modulus of matrix

$\alpha_m = 11 \times 10^{-6}$       average coefficient of thermal expansion for inclusion in  $\text{K}^{-1}$

$\alpha_m' = 8.5 \times 10^{-6}$  average coefficient of thermal expansion for martensitic matrix

$\alpha_i = 7.3 \times 10^{-6}$  average coefficient of thermal expansion of matrix in  $K^{-1}$

$f = 0.1$  volume fraction of inclusions

$T_0 = 756$  lowest temperature at which mismatch is zero in  $^{\circ}C$

$T_R = 25$  room temperature  $^{\circ}C$

$M_s = 70^{\circ}C$  martensite start temperature

$M_f = 47^{\circ}C$  martensite finish temperature

The equivalent transformation strain tensor  $\epsilon^T$  is a function of the mismatch strain tensor  $\epsilon^*$  between matrix  $m$  and inclusion  $i$ .

$$\epsilon^T = - \{ (C_m - C_i) \cdot [S - f(S - I)] - C_m \}^{-1} C_i \epsilon^* \quad (1)$$

where  $f$  is the volume fraction of inclusions,  $I$  is the identity matrix,  $C$  is the stiffness tensor, and  $S$  is the Eshelby tensor.

Here

$$C_i = \begin{bmatrix} 515 & 106 & 106 & 0 & 0 & 0 \\ 106 & 515 & 106 & 0 & 0 & 0 \\ 106 & 106 & 515 & 0 & 0 & 0 \\ 0 & 0 & 0 & 179 & 0 & 0 \\ 0 & 0 & 0 & 0 & 179 & 0 \\ 0 & 0 & 0 & 0 & 0 & 179 \end{bmatrix} \quad \text{Stiffness tensor for inclusion (GPa)}$$

$$S = \begin{bmatrix} \frac{7-5\nu_m}{15(1-\nu_m)} & \frac{-1+5\nu_m}{15(1-\nu_m)} & \frac{-1+5\nu_m}{15(1-\nu_m)} & 0 & 0 & 0 \\ \frac{-1+5\nu_m}{15(1-\nu_m)} & \frac{7-5\nu_m}{15(1-\nu_m)} & \frac{-1+5\nu_m}{15(1-\nu_m)} & 0 & 0 & 0 \\ \frac{-1+5\nu_m}{15(1-\nu_m)} & \frac{-1+5\nu_m}{15(1-\nu_m)} & \frac{7-5\nu_m}{15(1-\nu_m)} & 0 & 0 & 0 \\ 0 & 0 & 0 & \frac{8-10\nu_m}{15(1-\nu_m)} & 0 & 0 \\ 0 & 0 & 0 & 0 & \frac{8-10\nu_m}{15(1-\nu_m)} & 0 \\ 0 & 0 & 0 & 0 & 0 & \frac{8-10\nu_m}{15(1-\nu_m)} \end{bmatrix}$$

$$= \begin{bmatrix} 0.538 & 0.077 & 0.077 & 0 & 0 & 0 \\ 0.077 & 0.538 & 0.077 & 0 & 0 & 0 \\ 0.077 & 0.077 & 0.538 & 0 & 0 & 0 \\ 0 & 0 & 0 & 0.817 & 0 & 0 \\ 0 & 0 & 0 & 0 & 0.817 & 0 \\ 0 & 0 & 0 & 0 & 0 & 0.817 \end{bmatrix} \text{ Eshelby Tensor}$$

$$C_m = \begin{bmatrix} c_{11} & c_{12} & c_{12} & 0 & 0 & 0 \\ c_{12} & c_{11} & c_{12} & 0 & 0 & 0 \\ c_{12} & c_{12} & c_{11} & 0 & 0 & 0 \\ 0 & 0 & 0 & c_{44} & 0 & 0 \\ 0 & 0 & 0 & 0 & c_{44} & 0 \\ 0 & 0 & 0 & 0 & 0 & c_{44} \end{bmatrix}$$

$$= \begin{bmatrix} 200.6 & 108 & 108 & 0 & 0 & 0 \\ 108 & 200.6 & 108 & 0 & 0 & 0 \\ 108 & 108 & 200.6 & 0 & 0 & 0 \\ 0 & 0 & 0 & 20 & 0 & 0 \\ 0 & 0 & 0 & 0 & 20 & 0 \\ 0 & 0 & 0 & 0 & 0 & 20 \end{bmatrix} \text{Stiffness tensor of matrix}$$

$$I = \begin{bmatrix} 1 & 0 & 0 & 0 & 0 & 0 \\ 0 & 1 & 0 & 0 & 0 & 0 \\ 0 & 0 & 1 & 0 & 0 & 0 \\ 0 & 0 & 0 & 1 & 0 & 0 \\ 0 & 0 & 0 & 0 & 1 & 0 \\ 0 & 0 & 0 & 0 & 0 & 1 \end{bmatrix} \text{Identity Matrix}$$

where  $f$  is the volume fraction,  $I$  is the identity matrix,  $C$  is the stiffness tensor, and  $S$  the Eshelby tensor for spherical particles, is only a function of the matrix Poisson's ratio  $\nu$ . The matrix mean internal stress tensor  $\langle \sigma \rangle_M$  and inclusion mean internal stress tensor  $\langle \sigma \rangle_i$  can then be calculated from equation (6) as

$$\langle \sigma \rangle_m = -f C_m (S-I) \varepsilon^T \quad (2)$$

$$\langle \sigma \rangle_i = (1-f) C_m (S-I) \varepsilon^T \quad (3)$$

The corresponding mean internal strain tensors  $\langle \varepsilon \rangle$  for the matrix and inclusion are

$$\langle \varepsilon \rangle_m = C_m^{-1} \langle \sigma \rangle_m \quad (4)$$

$$\langle \varepsilon \rangle_i = C_i^{-1} \langle \sigma \rangle_i \quad (5)$$

and correspond to the average strains measured by neutron diffraction when no external load is applied on the composite.

Dunand *et al.* [1996] assume that the total mismatch resulting from cooling of the composite from annealing temperature to room temperature  $T_R$  is the sum of a thermal strain – resulting from the mismatch of coefficients of thermal expansion of matrix and inclusion- and a transformation strain-resulting from the phase transformation of the matrix in the presence of the nontransforming inclusions.

First, the linear thermal mismatch strain resulting from cooling from the annealing temperature to  $M_s$  is

$$\varepsilon_{thA}^* = (\alpha_m - \alpha_i) (T_0 - M_s) \quad (6)$$

$$\varepsilon_{thA}^* = 0.03526$$

where  $\alpha_m$  is the austenitic matrix coefficient of thermal expansion,  $\alpha_i$  is the inclusion coefficient of thermal expansion, and  $T_0$  is the temperature at which the mismatch between the two phases is zero, corresponding to the annealing temperature if no relaxation takes place during cooling from the annealing temperature. Because diffusion and creep processes are rapid above a homologous temperature of 0.65, we assume that all thermal mismatch stresses are relaxed at this temperature, corresponding to  $T_0=756^\circ\text{C}$  for equiatomic NiTi.

Second, the matrix allotropic transformation results in a linear expansion strain upon cooling from  $M_s$  to  $M_f$ .

$$\varepsilon_{A-M}^* = \frac{1}{3} \frac{\Delta V}{V} \quad (7)$$

$$\varepsilon_{A-M}^* = 0.00354$$

where  $\Delta V/V$  is the fractional constrained volume change upon phase transformation and assuming that the phase transformation is purely hydrostatic in nature, i.e., that all shear strains are zero on average. This is expected for a textureless polycrystal, where the shear strains resulting from the transformation of individual variants are canceled by self-accommodation. Third, the linear thermal mismatch strain resulting from cooling the martensitic composite from cooling the martensitic composite from  $M_f$  to  $T_R$  is

$$\varepsilon_{thM}^* = (\alpha_m' - \alpha_i) (M_f - T_R) \quad (8)$$

$$\varepsilon_{thM}^* = 0.3$$

where  $\alpha_m'$  is the martensitic matrix coefficient of thermal expansion.

The total mismatch strain tensor  $\varepsilon^*$  is found by adding the contributions of Eqs. [6] through [8] written in the simplified matrix notation of Nye [1985] as

$$\varepsilon^* = (\varepsilon_{thA}^* + \varepsilon_{A-M}^* + \varepsilon_{thM}^*) [1, 1, 1, 0, 0, 0] \quad (9)$$

$$\varepsilon^* = 0.34 [1, 1, 1, 0, 0, 0]$$

and neglecting higher order terms.

The final matrix mean internal stress could be calculated as

$$\langle \sigma \rangle_m = -f C_m (S-I) \varepsilon^T$$

$$\frac{\sigma_m}{10^6} = \begin{bmatrix} 30 \\ 30 \\ 30 \\ 0 \\ 0 \\ 0 \end{bmatrix} \text{ Matrix mean internal stress in MPa}$$

Recently [Rajagopalan *et al.* 2005], have shown that stresses as low as 30 MPa can cause twinning in martensitic NiTi. This was confirmed by neutron diffraction experiments. Hence, based on an Eshelby approach we expect the coefficient of thermal mismatch stresses between the matrix and the inclusion to result in additional twinning. Thus, some of the twins observed in the images in Figure 34 could include those due to this coefficient of thermal mismatch stresses.

### 5.2.3 Comparison with Spherical Indenter

Repeated attempts were made to examine the matrix-inclusion interface for twins, but they proved unsuccessful. On the other hand, twins were clearly observed in the matrix, away from the matrix-inclusion interface. For an explanation for why the twins are not found at the interface, the analogy of an indenter was considered, where the maximum stress under the indenter is not at the point of contact but at some distance below the point of contact.

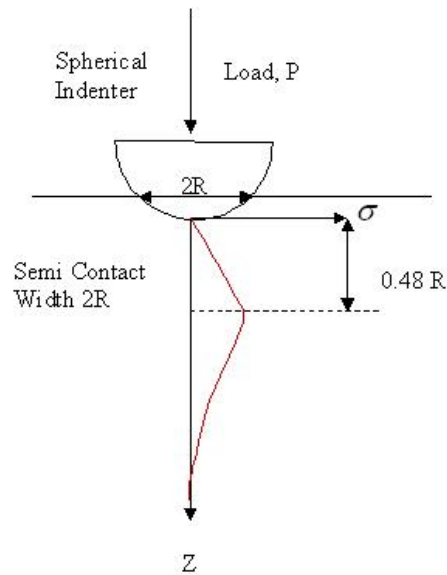


Figure 35: Diagram showing the maximum stress under the indenter

Maximum stress under indenter is shown in Figure 35 [Rajagopalan *et al.* 2005]. The maximum stress under the indenter is at a distance of  $0.48R$ , where  $R$  is the contact radius. Considering a spherical particle in the martensitic NiTi matrix, and fitting a curvature to the particle, a distance from the interface where the stress is maximal can be estimated. For the particle shown in Figure 36 this distance is of the order of 250 nm. This distance appears to agree with the distance of some of the observed twins from the matrix-inclusion interface.



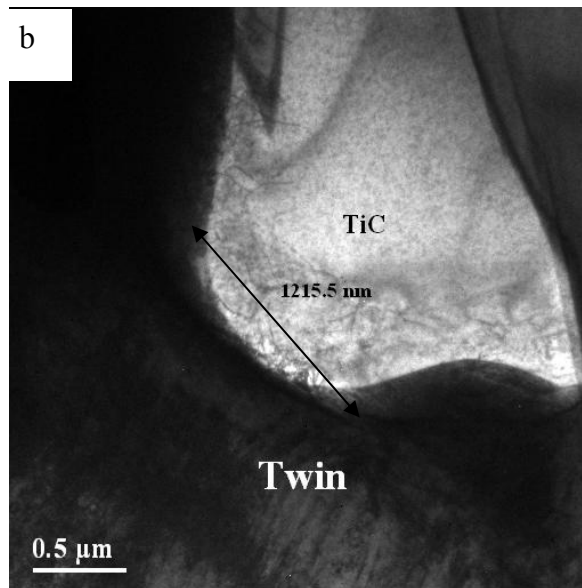
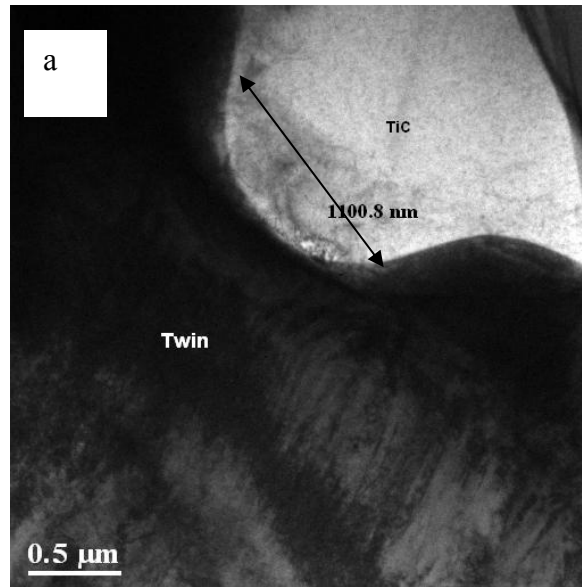


Figure 36: The contact radius of the TiC particle for the spherical indenter analogy

## CHAPTER SIX: R-Phase in NiTiFe

### 6.1 Results

NiTiFe samples for TEM were prepared by the *in situ* FIB technique and also by electropolishing. The processing of this material is described in Section 3.7. Figure 37 shows diffraction patterns at (a) room temperature, (b) -20°C, (c) -60°C and (d) -160°C in the [111] beam direction. Figure 38 is the corresponding figure for the [110] beam direction and Figure 39 is the corresponding figure for the [100] beam direction.

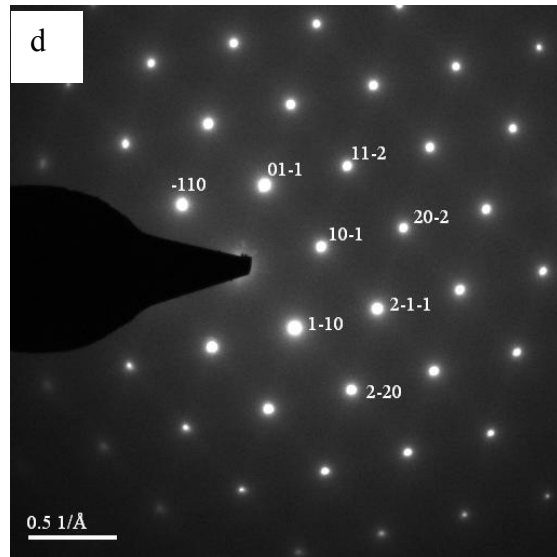
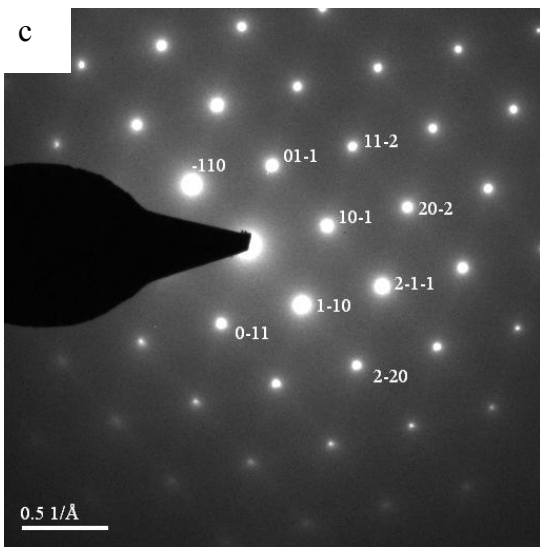
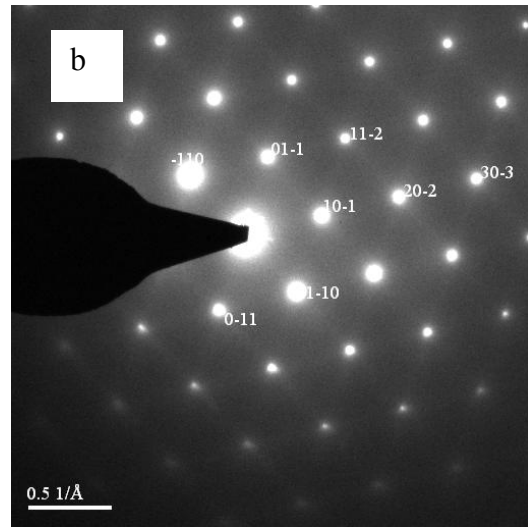
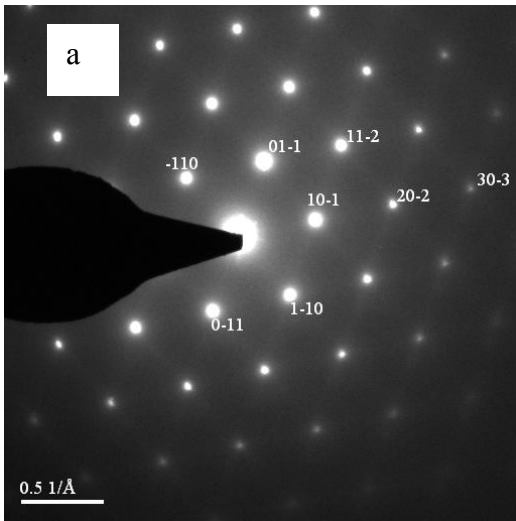


Figure 37: SADP of NiTiFe at (a) room temperature, (b)  $-20^\circ\text{C}$ , (c)  $-60^\circ\text{C}$  and (d)  $-160^\circ\text{C}$  for the  $[111]$  beam direction

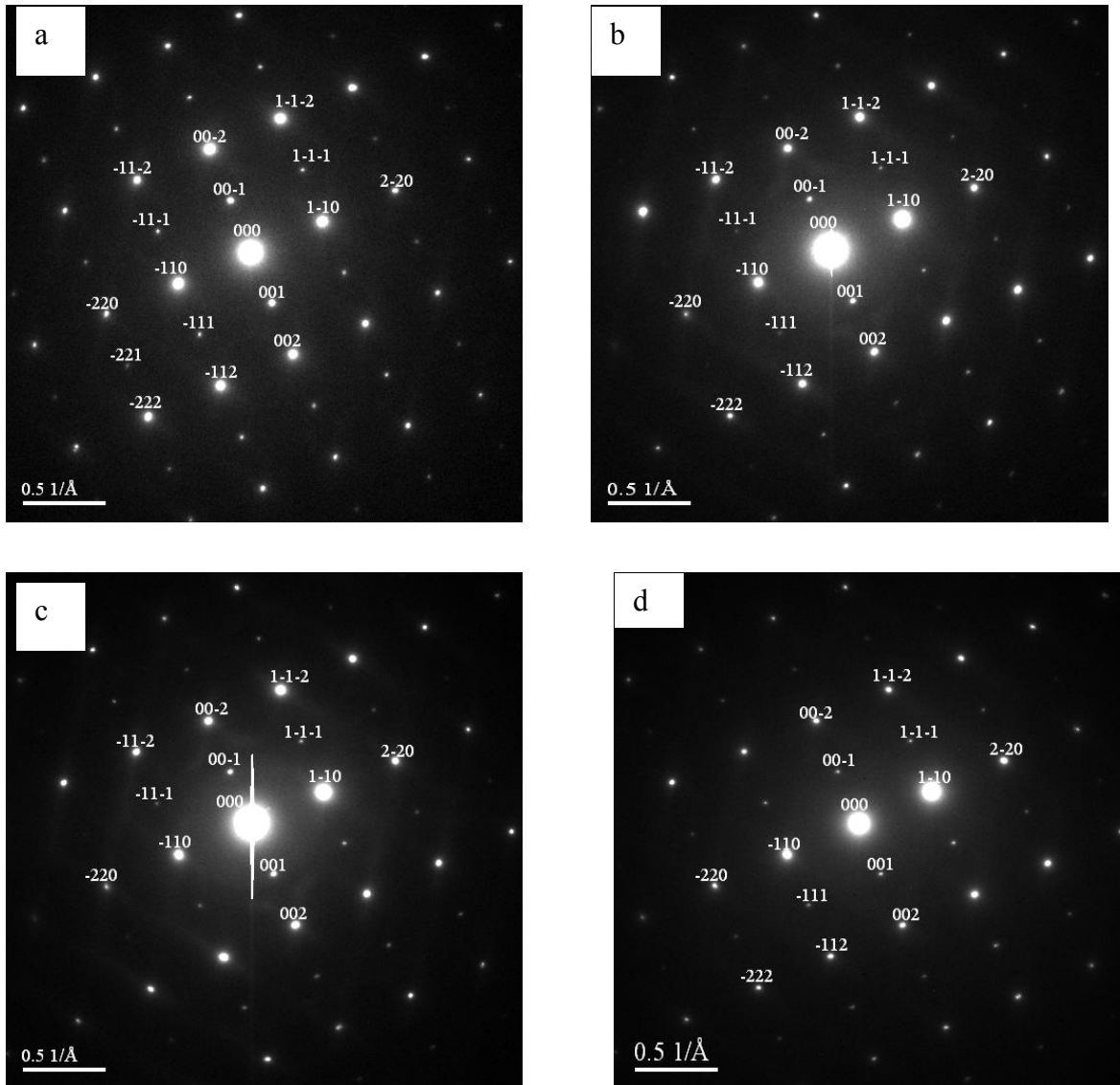


Figure 38: SADP of NiTiFe at (a) room temperature, (b) -20°C, (c) -60°C and (d) -160°C for the [110] beam direction

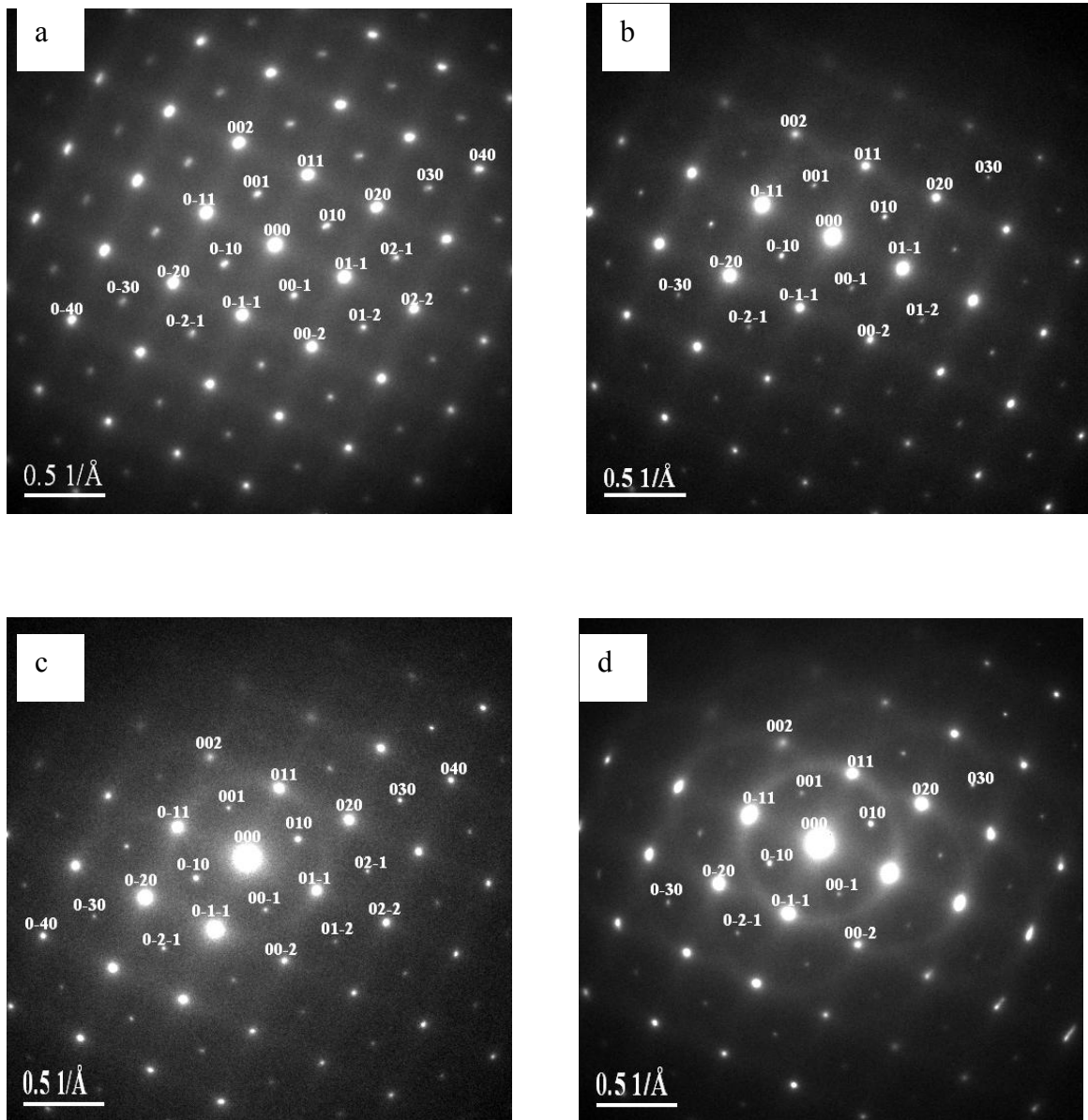


Figure 39: SADP of NiTiFe at (a) room temperature, (b) -20°C, (c) -60°C and (d) -160°C for the [100]-beam direction

## **6.2 Discussion**

For the formation of R-phase, the composition of the alloy and heat treatment play a major role. From the literature, it is found that the R-phase transformation is characterized by a sharp increase in resistivity and appearance of super lattice reflections. In order to find the R-phase, the sample was prepared by electropolishing as well as by FIB techniques. For TEM, a cold stage was used where a special sample holder that can take the sample to the desired temperature was employed. The sample was taken from room temperature to  $-160\text{ }^{\circ}\text{C}$  using the cold stage. Differential Scanning Calorimetry and neutron diffraction measurements on identical samples have shown that the R-phase transformation occurs at  $-46\text{ }^{\circ}\text{C}$  [Lemanski 2005, Shmalo 2006]. Even though temperatures as low as  $-160\text{ }^{\circ}\text{C}$  were reached, it was surprising that the sample did not show any signs of R-phase such as appearance of superlattice reflections. The reason for the absence of R-phase is being investigated here under.

The TEM images did not show any grain boundaries and thus it was possible that the sample was a single grain. Furthermore, any inhomogeneities such as precipitates were absent. Tan & Crone [2004], reported the formation of the R-phase near inhomogeneities like precipitates and dislocations. According to them, the R-phase nucleates at  $\text{Ti}_{11}\text{Ni}_{14}$  precipitates as they have very similar crystal structures. Miyazaki & Wayman [1987], reported the formation of R-phase in single crystals during TEM, however they used an external straining mechanism to induce internal stresses. We thus hypothesize that the stress-free nature of the NiTiFe sample investigated resulted in the failure to observe the R-phase.

## CHAPTER SEVEN: CONCLUSIONS AND FUTURE WORK

This work was initiated with the objective of connecting the macroscopic behavior in shape memory alloys with microstructural observations from TEM. Based on the work presented in the preceding chapters, the following conclusions can be drawn:

1. Both *in situ* and *ex situ* versions of the FIB technique can be successfully used to fabricate shape memory alloy samples for TEM characterization.
2. Less success was achieved using electropolishing and possible reasons include a temperature induced phase transformation while cooling with electrolyte with liquid nitrogen or oxidation of Ti that shifts the composition of the sample being prepared.
3. As expected from conventional metallurgy principles, cold drawn samples qualitatively exhibited more texture compared to samples prepared by hot isostatic pressing (HIP).
4. The Ni-rich NiTi samples were fully austenitic in the undeformed state. The introduction of plastic deformation (8% and 14% in the samples investigated) resulted in the stabilization of martensite in the unloaded state. An interlaying morphology of the austenite and martensite was observed and the martensite needles tended to orient themselves in preferred orientations. The aforementioned observations were more pronounced in mechanically cycled samples. Additionally, dislocations were seen at the interface between adjoining martensitic needles. E.g., the Burgers vector of such an edge dislocation was identified and confirmed using line profiles.
5. The observed dislocations (especially in the cycled samples) are either (i) in a stable or locked configuration or (ii) are being shielded from the external applied stress since they are not associated with unrecoverable strain after a load-unload cycle. On application of stress, the

austenite transforms to martensite and in doing so can be expected to accommodate the stress and strain mismatch through preferential transformation, variant selection, reorientation and coalescence. The stabilized martensite (i.e., martensite that exists in the unloaded state) also can be expected to accommodate the mismatch through variant reorientation and coalescence. The exact reason for the dislocation existing at the interface between adjoining martensitic needles is not clear. The following reasons were proposed: (i) It could serve to accommodate the mismatch between various variants in the stabilized martensite; (ii) it could be that the dislocations pin the martensite needles; (iii) it is also possible that the martensite is stabilized around the dislocations due to the stress field resulting from the dislocations.

6. A martensitic NiTi sample was also thermally cycled through its transformation while loaded. Such a sample simulates a NiTi actuator in an engineering application. Significant variant coalescence, variant reorientation and preferred variant selection was observed as a result of the internal stresses generated because of the thermal cycling.

7. A martensitic NiTi-TiC composite was also characterized. The interface between the matrix and the inclusion was free of twins while significant twins were observed at a distance away from the matrix-inclusion interface. A spherical indenter analogy was presented to explain this observation. An Eshelby homogenous equivalent inclusion approach was used to assess the magnitude of the thermal mismatch stresses between the matrix and the inclusion to determine if the stresses were high enough to cause additional twinning.

8. Incorporating a cold stage, diffraction patterns were obtained at temperatures as low as  $-160^{\circ}\text{C}$  in order to observe the R-phase in NiTiFe. However, the R-phase was not observed and reasons for this were presented.



Thus the above conclusion provides insight in to deformation phenomena in shape memory materials that have implications for engineering applications (e.g., cyclic performance of actuators, engineering life of superelastic components and low-hysteresis R-phase based actuators). In terms of future work, the following is proposed:

1. Further investigation to examine the reason for being unable to obtain the R-phase at  $-160^{\circ}\text{C}$  when differential scanning calorimetry and neutron diffraction measurements confirm such a transformation.
2. Further investigation to prepare shape memory samples for TEM using electropolishing and to avoid the R-phase transformation.
3. To examine the NiTi-TiC interface more carefully for possible stress and strain accommodation mechanisms.

## **APPENDIX: LATTICE PARAMETERS**

Austenite lattice parameter used was  $a=0.3007$  nm [Villars and Calvert, 1991]

Table 2 : Properties of reflections in “kinematic diffraction” patterns of the austenite

h	k	l	$\frac{1}{dhkl}$ [nm <sup>-1</sup> ]	Multiplicity	Relative Intensity
0	0	1	3.3256	6	1.0489
1	0	1	4.7031	12	1000.00
1	1	1	5.7601	8	0.2123
0	0	2	6.6511	6	167.5578
1	0	2	7.4362	24	1.1614
1	1	2	8.1460	24	325.5342
2	0	2	9.4061	12	94.0165
2	1	2	9.9767	24	0.8228
0	0	3	9.9767	6	0.2057
1	0	3	10.5164	24	119.6295
1	1	3	11.0297	24	0.6951
2	2	2	11.5201	8	26.8965
2	0	3	11.9905	24	0.6013
2	1	3	12.4432	48	113.1572
0	0	4	13.3023	6	10.2042
2	2	3	13.7117	24	0.4490
1	0	4	13.7117	24	0.4490
1	1	4	14.1092	36	45.1819

Martensite lattice parameter used was  $a=0.2898$  nm,  $b=0.4108$ ,  $c=0.4646$ ,  $\beta=97.8^\circ$  [Villars and Calvert, 1991]

Table 3: Properties of reflections in “kinematic diffraction” patterns of the martensite

h	k	l	$\frac{1}{d_{hkl}}$ [nm <sup>-1</sup> ]	Multiplicity	Relative Intensity
-1	0	0	2.1789	2	17.8868
1	1	0	3.2231	4	7.3902
0	0	1	3.4908	2	1.6103
-1	0	1	3.8900	2	102.6104
0	1	1	4.2221	4	97.4969
1	0	1	4.3283	2	25.6646
2	0	0	4.3578	2	516.0199
-1	1	1	4.5577	4	1000.00
0	2	0	4.7500	2	567.6440
1	1	1	4.9371	4	954.0109
-2	1	0	4.9630	4	260.1963
1	2	0	5.2259	4	7.4207
-2	0	1	5.2510	2	19.8671
-2	1	1	5.7632	4	83.1274
0	2	1	5.8948	4	0.4411
2	0	1	5.8973	2	1.7480
-1	2	1	6.1396	4	60.2997
2	1	1	6.3576	4	0.7658
1	2	1	6.4263	4	14.2711
2	2	0	6.4462	4	314.4082

-3	0	0	6.5367	2	10.7990
-3	1	0	6.9548	4	6.7790
0	0	2	6.9815	2	127.0658
-3	0	1	7.0363	2	81.8974
-1	0	2	7.0631	2	46.8761
-2	2	1	7.0807	4	10.9842
0	1	2	7.3744	4	8.9882
-3	1	1	7.4264	4	74.1513
1	3	0	7.4517	8	15.2474
1	0	2	7.5559	2	20.0580
2	2	1	7.5724	4	3.2624
3	0	1	7.7664	2	53.4499
-2	0	2	7.7799	2	37.1677
1	1	2	7.9204	4	3.8649
0	3	1	7.9342	4	14.4075
-3	2	0	8.0803	4	12.8454
-1	3	1	8.1178	4	156.7085
3	1	1	8.1214	4	112.8638
-2	1	2	8.1344	4	61.1022
1	3	1	8.3367	4	176.0234
2	3	0	8.3520	4	50.4544
0	2	2	8.4442	4	131.0103
-3	2	1	8.4896	4	87.8053
-1	2	2	8.5117	4	51.0326
2	0	2	8.6566	2	64.8159
-4	0	0	8.7156	2	13.2508
-2	3	1	8.8510	4	23.7247
1	2	2	8.9249	4	21.9813
2	1	2	8.9765	4	14.5788

-3	0	2	8.9812	2	15.2112
-4	0	1	8.9968	2	16.4411
4	1	0	9.0334	4	100.3174
3	2	1	9.1038	4	60.8491
-2	2	2	9.1154	4	40.7509
2	3	1	9.2490	4	0.0230
-3	2	1	9.2900	4	34.2974
-4	1	1	9.3050	4	12.7630
0	4	0	9.5001	2	58.1216
-3	3	0	9.6693	4	1.1514
-1	4	0	9.7467	4	1.5102
4	0	1	9.7648	2	0.0108
2	2	2	9.8742	4	80.6196
-4	2	0	9.9259	4	15.8662
0	3	2	9.9754	4	3.9641
-3	3	1	10.0138	4	23.4929
-1	3	2	10.0326	4	1.5351

## LIST OF REFERENCES

- [1] Buehler W.J. and Wang F.E., “*A Summary of Recent Research on the Nitinol Alloys and their Potential Application in Ocean Engineering*”, *Ocean Eng.* 1, 1967, 105-120
- [2] Cai W., Murakami Y. and Otsuka K., *Materials Science and Engineering A273-275*, 1999, 186- 189
- [3] Chrobak D. and Stroz D., *Scripta Materialia*, Vol 52, 2005,757-760
- [4] Clyne T.W. and Withers P.J., *An Introduction to Metal Matrix Composites*, Cambridge University Press, 1993
- [6] Dunand D.C., Mari D., Bourke M.A.M. and Roberts J.A., *Metallurgical and Materials Transactions A*, Vol 27A, 1996, 2820-2836
- [5] Dunand D.C., Fukami-Ushiro K.L., Mari D., Roberts J.A. and Bourke M.A., *Mat.Res.Soc.Symp.Proc*, Vol 459, 1997, 131-142
- [7] Fukami-Ushiro K.L., Mari D. and Dunand D.C., *Metallurgical and Materials Transactions A*, Vol 27A, 1996, 183-191

- [8] Fultz B. and Howe J.M., *Transmission Electron Microscopy and Diffractometry of Materials*, 2001
- [9] Funakubo H., *Shape Memory Alloys*, Gordon and Breach Science Publishers, New York, 1987
- [10] Giannuzzi L.A. and Stevie F.A., *Micron* 30, 1999, 197-204
- [11] Gall K. and Maier H.J., *Acta Materialia* Vol 50, 2002, 4643-4657
- [12] Kim J.I., Yinong L. and Miyazaki S., *Acta Materialia*, Vol 52, 2004, 487-499
- [13] Lemanski J., “*Cryogenic Shape Memory Alloy Actuators for Spaceport Technologies: Materials Characterization and Prototype Testing*”, MS Thesis, UCF, 2005
- [14] Liu Y., Xie Z. and Humbeeck J.V., *Materials Science and Engineering* A273-275, 1999, 673-678
- [15] Reimer L., *Transmission Electron Microscopy*, Springer New York, 1997
- [16] Mari D., Bataillard L., Dunand D.C. and Gotthardt R., *Journal De Physique IV*, Vol 5, Dec 1995



- [17] Miyazaki S. and Otsuka K., *Metallurgical Transactions A*, Vol 17A, 1986, 53-63
- [18] Miyazaki S. and Wayman C.M., *Acta Metallurgica*, Vol 36, 1987, 181-192
- [19] Murakami Y. and Shindo D., *Philosophical Magazine Letters*, Vol 81, 2001, 631-638
- [20] Nam T.H., Kim J.H. and Choi M.S., *Journal of Materials Science Letters* Vol 21, 2002, 685-688
- [21] Nye J.F., *Physical Properties of Crystals*, Oxford University Press, Oxford, UK, 1985
- [22] Otsuka K. and Wayman C. M., *Shape Memory Materials*, Cambridge University Press, Cambridge, UK, 1998
- [23] Rajagopalan S., Little A.L., Bourke M.A.M. and Vaidyanathan R., *Applied Physics Letters*, Vol 86, 2005, 081901-3
- [24] Saburi T. and Wayman C.M., *Acta Metallurgica*, Vol 28, 1980,15-32
- [25] Shmalo S., PhD Dissertation, University of Central Florida, 2006 (Expected)
- [26] Srinivasan A.V. and McFarland D.M., *Smart Structures*, Cambridge University Press, Cambridge, UK, 2001

[27] Stroz D., *Scripta Materialia*, Vol 47, 2002,363-369

[28] Stroz D., *Materials Chemistry and Physics*, Vol 81, 2003, 460-462

[29] Tan L. and Crone W.C., *Scripta Materialia*, Vol 50, 2004, 819-823

[30] Reed Hill R. and Abbaschian R., *Physical Metallurgy Principles*, third edition, 2003

[31] UNL, <http://www.unl.edu/CMRAcfem> , Dec 2004

[32] Uchino K., “Shape Memory Ceramics”, in *Shape Memory Materials*, edited by Otsuka K. and Wayman C. M., Cambridge University Press, 1998, 184-202.

[33] Vaidyanathan R., “*Mechanical Properties of Superelastic and Shape-Memory NiTi and NiTi-TiC Composites Investigated by Neutron Diffraction*”, PhD Dissertation, Massachusetts Institute of Technology, 1998

[34] Vaidyanathan R., Bourke M.A.M. and Dunand D.C., *Acta Materialia* Vol 47, 1999a, 3353-3366

[35] Vaidyanathan R., Bourke M.A.M. and Dunand D.C., *Materials Science and Engineering* A273-275, 1999b, 404-409

[36] Vaidyanathan R., Dunand D.C. and Ramamurty U., *Materials Science and Engineering* A289, 2000, 208-216

[37] Vaidyanathan R., “ Shape-Memory Alloys”, in *Kirk-Othmer Encyclopedia of Chemical Technology*, Wiley InterScience, John Wiley and Sons Inc., New York, 2002 edition.

[38] Villars P. and Calvert L.D., *Pearson's handbook of crystallographic data for intermetallic phases*, 2nd Ed, 1991

[39] Williams D.B. and Carter C.B., *Transmission Electron Microscopy*, Plenum Press, New York, 1996

[40] Wu S.K., Lin H.C., Yen Y.C. and Chen J.C., *Materials Letters* Vol 46, 2000, 175-180

[41] Xie Z., Liu Y. and Humbeeck J.V., *Acta Materialia*, Vol 46, 1998, 1989-2000